POLITECNICO DI TORINO

Master of science program in Energy and Nuclear Engineering

A.a. 2025/2026

Master's Thesis

Thermo-Mechanical Modelling of a high Pressure AEM electrolyser

Supervisor:

Prof. Massimo Santarelli

Co. Supervisor:

Mohsen Mansourkiaei

Martina Prastaro

Candidate:

Hosein Parsayan

July 2026

Abstract

The rapid transition to renewable energy sources is a fundamental requirement to achieve carbon neutrality and decouple global economic growth from carbon emissions. Anion Exchange Membrane Water Electrolysis (AEMWE) is gaining traction because its non-noble transition metal catalysts significantly reduce capital costs. The objective of this thesis is the 3D thermo-mechanical modeling of a single-cell high-pressure AEM electrolyser to ensure performance efficiency at 30 bar. To achieve optimal operational aspects, cell layer material selection must be carefully evaluated regarding stability, economics, and mechanical performance. For each layer, most common materials have been assessed and based on different criteria such as performance, cost and availability in the commercial markets, different material configurations of the single cell have been suggested. Optimizing the initial assembly technique is vital, as excessive clamping preloads induce structural cracks, while insufficient preloads cause fluid leakage. Analytical calculation models indicate that the optimal structural clamping pressure for an active membrane layer ranges from 1.5 to 3.0 MPa. A sensitivity analysis was done using MATLAB to compare the effect of different components of the cell on the clamping force. At 30 bar operating pressure, utilizing a planar geometric cell configuration successfully satisfies the overall design criteria and stackability parameters while the tubular and circular design were also studied. A 3D computational geometry was implemented in COMSOL Multiphysics version 6.2 using a finite element normal-sized mesh sequence. The numerical approach couples Heat Transfer in Solids, Solid Mechanics, and Secondary Current Distribution physics concurrently within the simulation. The calculated polarization curve reports a produced current density of 0.65 A/cm^2 at a balanced applied voltage of 2 V. Thermal simulation results show that the highest temperatures concentrate directly inside the membrane, peaking safely at approximately 360 K. Mechanical analysis reveals that Von Mises stress peaks locally at the cathode end plate edges, while the active area pressure remains uniform. Validation against physical literature reference models confirms that all computed thermal and pressure profiles match standard acceptable physical ranges.

Contents

List of Figures

List of Tables

1 Introduction

1.1. Context and Motivation

The global energy landscape is currently undergoing its most significant transformation since the Industrial Revolution. For over a century, the engine of human progress has been fueled by the combustion of hydrocarbons; a convenient, yet ultimately costly, pact with the planet's finite resources. Today, the era of "burning things" to keep the lights on is reaching its natural conclusion, not merely out of scarcity, but out of necessity. The transition to renewable energy sources is no longer a peripheral environmental ambition; it is a fundamental requirement for the continued stability and prosperity of modern civilization.

The primary driver behind the shift to renewables is the undeniable reality of anthropogenic climate change. The accumulation of greenhouse gases (GHGs) in the atmosphere has triggered a measurable rise in global mean temperatures, leading to more frequent extreme weather events, rising sea levels, and the disruption of critical ecosystems. To align with the goals of the Paris Agreement and limit global warming to well below 2°C, a rapid decarbonization of the power sector is mandatory. Renewable energy technologies; principally solar, wind, hydro, and geothermal, offer a pathway to decouple economic growth from carbon emissions, providing a sustainable alternative to the fossil fuel status quo.

While climate change is the most urgent catalyst, the necessity of renewable energy is amplified by several other critical factors:

- Energy Security: Fossil fuel reserves are geographically concentrated, often leading to geopolitical tensions and economic vulnerability for importing nations. By harnessing localized renewable resources, countries can reduce their dependence on volatile international markets and enhance their national energy independence.
- Economic Resilience and Job Creation: The renewable sector has matured into a global economic powerhouse. As the levelized cost of energy (LCOE) for solar and wind continues to decrease, often outperforming coal and gas, renewables are becoming the most cost-effective choice for new capacity. Furthermore, the transition stimulates "green" job markets, from high-tech manufacturing to local infrastructure maintenance.

- Public Health and Air Quality: The hidden costs of fossil fuels include significant public health expenditures. Particulate matter and nitrogen oxides from combustion are major contributors to respiratory and cardiovascular diseases. Transitioning to clean energy sources directly translates to cleaner air, reduced healthcare burdens, and improved quality of life for urban populations.
- Technological Maturity and Scalability: Unlike previous decades, the barrier to entry for renewables is no longer technological viability. Advances in energy storage, smart grid integration, and material efficiency have made renewable systems reliable and scalable, capable of meeting the rigorous demands of industrial and residential sectors alike.

Hydrogen (H_2) has become a critical commodity in the global industrial landscape, with annual production exceeding 70 million metric tons and a market value of roughly 117 billion USD. Historically utilized in oil refining and chemical synthesis for ammonia and methanol, H_2 is now at the forefront of the global transition toward sustainability. While traditional production methods such as Steam Methane Reforming (SMR) and coal gasification are economically established, they are significant net emitters of greenhouse gases like CO_2.

To achieve carbon neutrality, there is a global shift toward "green" hydrogen produced via water electrolysis (WE) powered by renewable energy sources. Electrolysers offer the dual benefit of generating high-purity H_2 and acting as a versatile energy storage medium for intermittent sources like solar and wind power, enabling a stable "power-to-power" grid service. Among existing technologies, Anion Exchange Membrane Water Electrolysis (AEMWE) is gaining traction due to its ability to use non-noble, cost-effective transition metal catalysts (e.g., Ni, Fe) and low-concentration electrolytes, which significantly reduces capital costs compared to PEMWE.

1.2. Objective of the thesis

The primary objective of this thesis is the thermo-mechanical modeling and simulation of a high-pressure AEM electrolyser cell using COMSOL Multiphysics. By investigating the interplay between electrochemical reactions and mechanical constraints, this study aims to ensure structural integrity and performance efficiency at an operating pressure of 30 bar.

The report is structured as follows:

- Chapter 2: Literature Review; Provides an overview of hydrogen production technologies and a comparative analysis of different electrolysers, focusing on material selection and thermo-mechanical properties. Four different cell configurations are also provided based on materials of AEM components and their characteristics such as performance, cost and commercial availability.
- Chapter 3: Cell Design Study; Investigates critical design parameters, including clamping pressure calculations based on equivalent stiffness models and the selection of optimal geometries for high-pressure operation. Three common designs of AEM electrolysers which are tubular, circular and planar design are assessed and for different components, mainly the bipolar plate and gasket, most common geometries and design aspects are studied.
- Chapter 4: COMSOL Model Development; Details the 3D geometry construction, mesh generation, material property assignment, and the definition of physics and their required settings including Heat Transfer in Solids, Solid Mechanics and Secondary Current Distribution.
- Chapter 5: Results and Validation; Analyzes the polarization curves, temperature distributions, and Von Mises stress across cell components, validating the model against existing literature.

2 Literature Review

2.1. Hydrogen Production

Hydrogen has played a key role throughout the industrial life of humankind, and the global demand for H_2 has continuously increased, in fact tripling since 1975. Today's global H_2 production exceeds70 million metric tons (MMTs)/year and is consumed by the oil and gas industry and by metal refineries or turned into value-added products such as NH_3, feedstock chemicals such as CH_3OH, or specialty chemicals. H_2 can be considered a commodity of increasing need, with its importance already being reflected in its 117 billion US $ global market value. [1]

The future demand for H_2 may experience an additional increase due to H_2's physical properties such as its high gravimetric standard heat of formation (being the highest among fuels) and its standard heat of formation value (H_2's high heating value is 142MJ/kg), which is up to 3 times higher than that for liquid hydrocarbon fuels. Unfortunately, the volumetric density of H_2 of 8 MJ/L is 4 times lower than the 32MJ/L value of gasoline, thus requiring a high storage volume or significant gas compression.

Hydrogen is classified into different color shades, i.e., blue, gray, brown, black, and green respectively based on their hydrogen production technology, energy source, and environmental impact, as shown in Table 1.

Hydrogen Color	Technology	Source	Products	Cost ($ kg/H_2)	CO_2 emissions
Brown Hydrogen	Gasification	Brown coal (Lignite)	$H_2 + CO_2$	1.2–2.1	High
Black Hydrogen	Gasification	Black coal (Bituminous)	$H_2 + CO_2$	1.2–2.1	High
Grey Hydrogen	Reforming	Natural gas	$H_2 + CO_2$ (Released)	1–2.1	Medium
Blue Hydrogen	Reforming + carbon capture	Natural gas	$H_2 + CO_2$ (Captured 85-95%)	1.5–2.9	Low
Green Hydrogen	Electrolysis	Water	$H_2 + O_2$	3.6–5.8	Minimal

Table 1. Hydrogen color shades and their Technology, cost, and CO_2 emissions. [2]

Brown hydrogen is most abundant in use today, which is produced from hydrocarbon-rich feedstock (brown coal or methane) via the gasification process. But as a result, every tone of brown hydrogen releases 10–12 tons of CO_2 into the atmosphere. The black hydrogen is produced from coal gasification, during this coal gasification process syngas are produced from the gasifier and the hydrogen can be separated from the other gases using absorbers or special membranes and the remaining gases can be released into the atmosphere. [2]

Since the late1950s, steam methane reforming (SMR) has been predominantly used to produce H_2 followed by coal gasification and water electrolysis (WE), although the latter only contributes 2–4 % to today's global H_2 production. The heating value of CH_4 is high (the HHV is 55.5 MJ/kg), making the production of H_2 via SMR, which is in the range of 2€/kg H_2, economically attractive. H_2 production from fossil-based sources and moreover from CH_4, which is an ~30 times more potent greenhouse gas than CO_2, is a net emitter of CO_2 and other air pollutants. Based on calculations and a large set of reported data, Sunet al. [3] concluded average CO_2/ H_2 values of 9 kg/kg and 75.4 kg/MJ, translating into 720 MMT/year of CO_2 emitted for 70 MMT/year H_2 produced from SMR. The latter suggests that H_2 produced from SMR alone contributes 1.7 % to the 43.1 billion metric tons worldwide emissions from humans in 2019. Furthermore, the SMR process also produces H_2 of low purity (95–98%), requiring upgrading steps such as pressure swing absorption for many applications (e.g., fuels, specialty chemicals, and the ceramic and electronics industries). A mechanical compression step, which can be costly, also needs to be added. WEs have an advantage of generating higher-purity and already partially compressed H_2.

H_2 as a fuel for the H_2 economy is still a topic of interest. Much of the interest is driven by our increasing demand for energy based on cleaner sources. Correspondingly, H_2 is considered for energy storage (ES) and as a fuel. The driving forces for the H_2 economy are different across the globe depending on the resources, potential for energy generation, and political landscape of a country. To understand the feasibility for a specific H_2 production or storage route, technical gaps need to be identified and examined while keeping the cost in mind. The complete cycle needs to be considered including the end use of H_2, which can be manifold and may be different depending on the locations of H_2 production and consumption. H_2 is suitable for short-, medium-, and long-term energy storage. H_2 could, e.g., be reelectrified and injected back into the grid considering payback options known as power to power, which is used as a grid service to balance the grid when demand is high and production is low, or that known as price arbitrage, or to avoid the building of new grid connections. In addition, H_2 can also be transformed into a liquid organic hydrogen carrier (LOHC), enabling safer transport for later use.

Unlike fossil-based hydrogen production methods (e.g., steam methane reforming), water electrolysis enables the production of green hydrog*en* when powered by renewable electricity sources.

Electrolysis-based hydrogen production plays a crucial role in sectors such as transportation, chemical synthesis (e.g., ammonia and methanol), and energy storage systems. The ability of hydrogen to store excess renewable energy and release it when needed makes it particularly suitable for integrating intermittent sources like wind and solar power. [4]

Biomass and water are renewable sources that potentially allow clean H_2 production. Vast amounts of biomass are available, but the production of H_2 from water is more advanced; hence, H_2 derived from biomass is viewed to be implemented in the long term. H_2 production from water splitting can be divided into low- and high temperature electrolysis, thermochemical water splitting, and photoelectrochemical processes. Due to the absence of carbon-based reaction fuels, water splitting offers the cleanest way of producing H_2, provided clean sources of electricity are used.

Fossil fuel-free energy sources, such as nuclear and renewables, can be low or CO_2-free forms of energy. Nuclear offers several advantages as vast amounts are available and excess energy during low demands can be stored via, e.g., electrolysis. The outlet temperatures of nuclear reactors are in the range of 300–950 °C. Such a range can be attractive for higher-temperature electrolyzers, e.g., solid oxide electrolysis cells and thermochemical water splitting. However, these high-temperature electrolysis methods are not yet mature and suffer material-corrosion issues above 100 °C.

Solar and wind provide intermittent forms of energy. Solar is currently the fastest growing energy source due to the many investments made globally. The global capacity and usage of wind energy may well grow, as it is not costly and the technology is continuously advancing. Electrochemical WE is best suited in combination with wind energy, which calls for storage in the MW range. WE not only is able to provide large-scale storage but also offers medium- and longer-term storage unlike, e.g., flywheels, which are low cost but only allow short-term storage. In addition, WEs can accept high-current inputs per surface area, operate in dynamic modes, and can be ramped up quickly, which are all requirements for storage of intermittent energy sources. [4]

A scheme demonstrating the coupling of wind with WE and the possible uses of the stored H_2 is shown in Figure 1.

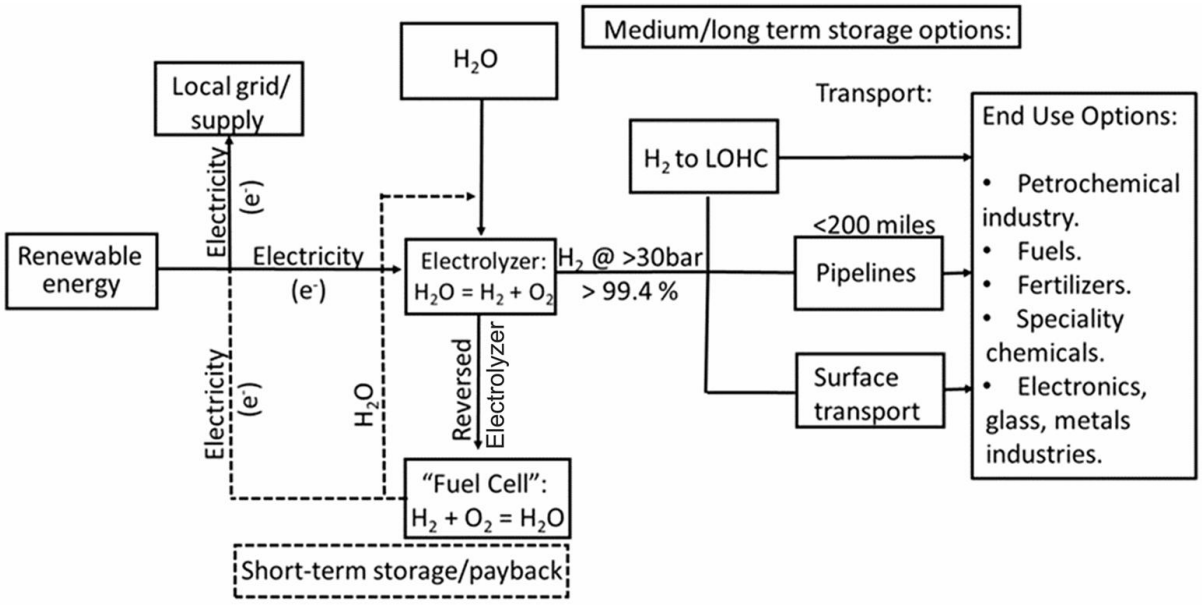

Figure 1. Schematic for the coupling of renewable (wind or solar) energy with water electrolysis. [4]

The figure shows options for short-, medium-, and long-term storage for the energy in the form of H_2 and possible end uses including payback options.

In this thesis report, the feasibility of H_2 produced from electrochemical water splitting is of interest. Among the low-temperature WEs, AEMWE is the least-mature technology, and prior to implementation, significant technological hurdles need to be overcome.

2.2. Overview of electrolysers

Water electrolysis is an electrochemical process that splits water into hydrogen and oxygen using electrical energy. The overall reaction is:

$$2H_2O(l) \rightarrow 2H_2(g) + O_2(g)$$

This process consists of two half-reactions:

- Cathode (Hydrogen Evolution Reaction, HER):

$$2H_2O + 2e^- \rightarrow H_2 + 2OH^-$$

- Anode (Oxygen Evolution Reaction, OER):

$$4OH^- \rightarrow O_2 + 2H_2O + 4e^-$$

These reactions occur simultaneously in an electrolyzer, separated by an electrolyte or membrane that allows ionic transport while preventing gas mixing.

The theoretical minimum voltage required for water splitting is 1.23 V under standard conditions; however, practical systems require higher voltages (typically 1.8–2.0 V) due to overpotentials and internal resistances.

Low-temperature water electrolyzers (WEs) can be divided into alkaline and acidic systems. They are further divided into finite and zero-gap electrolyzers (Figure 2). The schematics show the principles of a single WE cell, while an actual system consists of an assembly of many cells known as a stack. The anode and the cathode in a WE are spaced using a separator to avoid mixing of the H_2 and O_2 gases. [4]

The terms finite and zero gap are related to the distance of the separator between the anode and the cathode, where the O_2 evolution reaction (OER) and the H_2 evolution reaction (HER) take place.

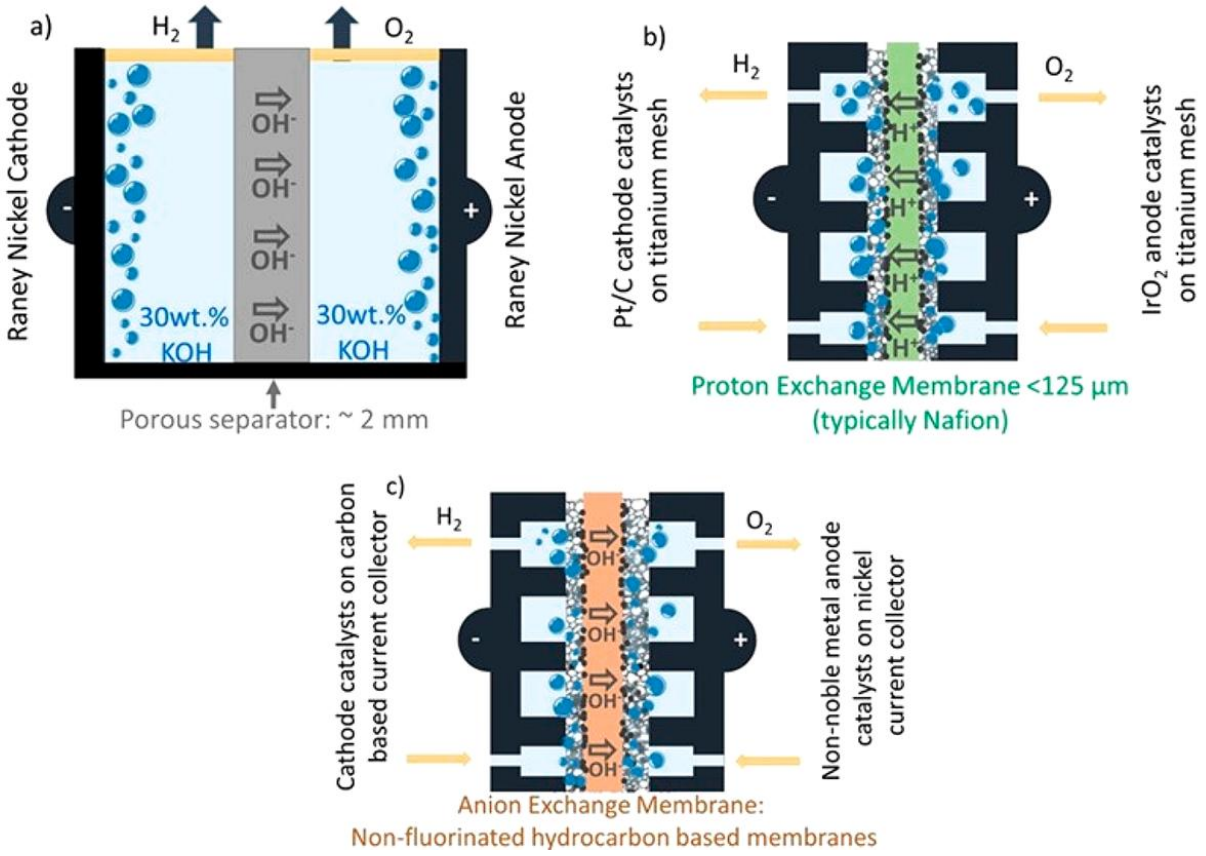

Figure 2. Schematic of the three types of WEs as (a) traditional alkaline finite WE (AWE), (b) zero-gap PEMWE running under acidic conditions using an H^+ conducting membrane, and (c) zero-gap AEMWE utilizing an OH^- conducting membrane. The goal is to use noble metal-free catalysts for the cathode and anode of an AEMWE. [4]

The solid oxide water electrolysis cell (SOEC) is one of the electrochemical conversion cells, it converts electrical energy into chemical energy. Typically, the solid oxide water electrolyzer operates with water in the form of steam at high temperatures (500–850 °C) can drastically reduce the power consumption to split the water into hydrogen and oxygen consequently increase the energy efficiency.

This improvement in energy efficiency can lead to a strong reduction in hydrogen cost due to power consumption being the main contributor to the hydrogen production cost in electrolysis. Apart from that, solid oxide water electrolysis offers two major advantages compared to the low-temperature water electrolysis technologies. The first one is that solid oxide water electrolysis can be thermally integrated easily with downstream chemical synthesis i.e., the production of methanol, dimethyl ether, and ammonia. The second one is that the solid oxide water electrolysis does not require the use of noble metal electrocatalysts and gives high conversion efficiency. [2]

The four types of water electrolysis technologies and their characteristics along with advantages and disadvantages are summarized in Table 2 and Table 3.

	Alkaline	AEM	PEM	Solid Oxide
Anode reaction	$2OH^- \rightarrow H_2O + \frac{1}{2} O_2 + 2e^-$	$2OH^- \rightarrow H_2O + \frac{1}{2} O_2 + 2e^-$	$H_2O \rightarrow 2H^+ + \frac{1}{2} O_2 + 2e^-$	$O^{2-} \rightarrow \frac{1}{2} O_2 + 2e^-$
Cathode Reaction	$2\ H_2O + 2e^- \rightarrow H_2 + 2OH^-$	$2\ H_2O + 2e^- \rightarrow H_2 + 2OH^-$	$2H^+ + 2e^- \rightarrow H_2$	$H_2O + 2e^- \rightarrow H_2 + O^{2-}$
Overall cell	$H_2O \rightarrow H_2 + \frac{1}{2} O_2$	$H_2O \rightarrow H_2 + \frac{1}{2} O_2$	$2H_2O \rightarrow H_2 + \frac{1}{2} O_2$	$H_2O \rightarrow H_2 + \frac{1}{2} O_2$
Electrolyte	KOH/NaOH (5M)	DVB polymer support with 1 M KOH/NaOH	Solid polymer electrolyte (PFSA)	Yttria stabilized Zirconia (YSZ)
Separator	Asbestos/Zirfon/Ni	Fumatech,	Nafion®	Solid electrolyte YSZ
Electrode/Catalyst (Hydrogen side)	Nickel coated perforated stainless steel	Nickel	Iridium oxide	Ni/YSZ
Electrode/Catalyst (Oxygen side)	Nickel coated perforated stainless steel	Nickel or NiFeCo alloys	Platinum carbon	Perovskites (LSCF, LSM) (La,Sr,Co,FE) (La,Sr,Mn)
Gas Diffusion layer	Nickel mesh	Nickel foam/carbon cloth	Titanium mesh/carbon cloth	Nickel mesh/foam
Bipolar Plates	Stainless steel/Nickel coated stainless steel	Stainless steel/Nickel coated stainless steel	Platinum/Gold-coated Titanium or Titanium	Cobalt coated stainless steel
Nominal current density	0.2–0.8 A/cm^2	0.2–2 A/cm^2	1–2 A/cm^2	0.3–1 A/cm^2
Voltage range (limits)	1.4–3 V	1.4–2.0 V	1.4–2.5 V	1.0–1.5 V
Operating temperature	70–90 °C	40–60 °C	50–80 °C	700–850 °C
Cell pressure	<30 bar	<35 bar	<70 bar	1 bar
H2 purity	99.5–99.9998%	99.9–99.9999%	99.9–99.9999%	99.9%
Efficiency	50%–78%	57%–59%	50%–83%	89% (laboratory)
Lifetime (stack)	60 000 h	>30 000 h	50 000–80 000 h	20 000 h
Development status	Mature	R & D	Commercialized	R & D
Electrode area	10 000–30 000 cm^2	<300 cm^2	1500 cm^2	200 cm^2
Capital costs (stack) minimum 1 MW	USD 270/kW	Unknown	USD 400/kW	>USD 2000/kW
Capital costs (stack) minimum 10 MW	USD 500–1000/kW	Unknown	USD 700–1400/kW	Unknown

Table 2. Technical characteristics of typical water electrolysis technologies. [2]

Electrolysis technology	Advantages	Disadvantages
Alkaline water electrolysis	• Well established Technology • Commercialized for industrial applications • Noble metal-free electrocatalysts • Relatively low cost • Long-term stability	• Limited current densities • Crossover of the gasses • High concentrated (5M KOH) liquid electrolyte
AEM water electrolysis	• Noble metal-free electrocatalysts • Low concentrated (1M KOH) liquid electrolyte.	• Limited stability • Under development
PEM water electrolysis	• Commercialized technology • Operates higher current densities • High purity of the gases • Compact system design • Quick response	• Cost of the cell components • Noble metal electrocatalysts • Acidic electrolyte
Solid oxide water electrolysis	• High working temperature • High efficiency	• Limited stability • Under development

Table 3. Advantages and disadvantages of typical water electrolysis technologies. [2]

2.2.1. Solid oxide electrolysis

Typically, solid oxide water electrolysis operates at higher temperatures with the consumption of water in the form of steam and generates green hydrogen and oxygen. During the solid oxide water electrolysis process, initially at the cathode side, the water molecule is reduced to hydrogen (H_2) and oxide ion (O^{2-}) by the addition of two electrons. The hydrogen released from the cathodic surface and the remaining oxide ion (O^{2-}) are traveled through the ion exchange membrane to the anode side. At the anode side, the oxide ions (O^{2-}) are further reduced to generate oxygen and electrons, then the produced oxygen is released from the anodic surface and the electrons are traveled through the external circuit to the cathode side by the positive attraction of the cathode. The basic working principle of solid oxide water electrolysis is shown in Figure 3. [2]

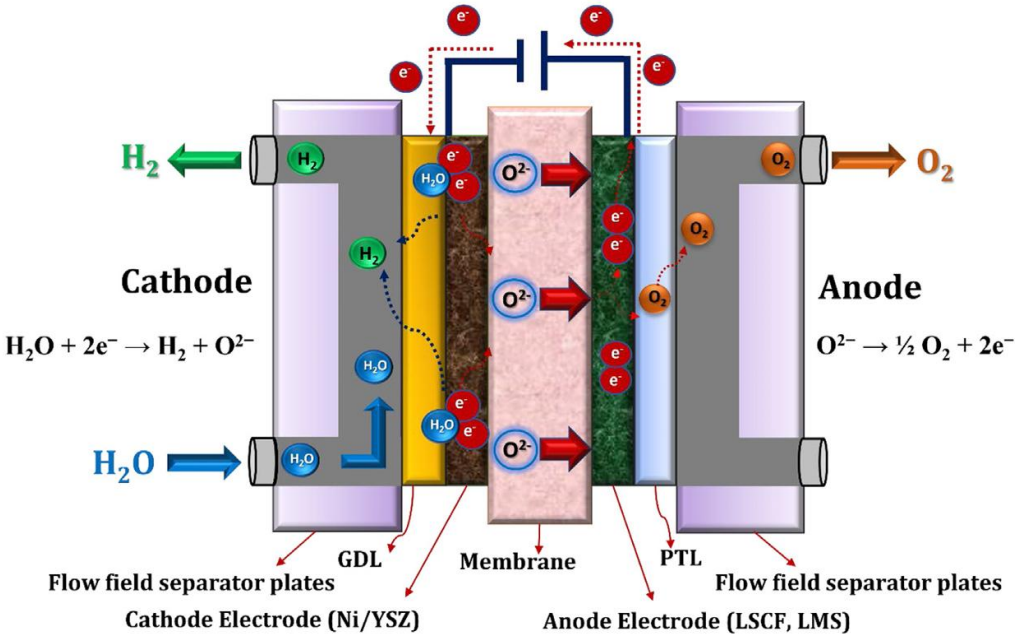

Figure 3. Schematic view of solid oxide water electrolysis working principle. [2]

Solid oxide water electrolysis cell consists of three main components such as two porous electrodes (anode and cathode) and a dense ceramic electrolyte capable of conducting oxide ion (O^{2-}). The most used electrolyte is yttria-stabilized zirconia (YSZ), which is especially 8 mol% of yttria doped in a dense zirconium oxide-based ceramic material (cubic crystal structure stabilized by the addition of yttria), due to the yttria-stabilized zirconia

electrolyte shows stable and excellent performance at higher temperatures (700–850 °C). Moreover, YSZ electrolyte having high ionic conductivity (10^{-2}– 10^{-1} S cm^{-1}) is associated with good chemical and thermal stability. The state-of-the-art hydrogen (cathode) electrode material is a ceramic metal composed of YSZ and nickel (Ni-YSZ) which is a non-noble metal catalyst with high electronic conductivity. The most widely used oxygen (anode) electrodes are perovskite materials i.e., LSCF ($La_{0.58}Sr_{0.4}Co_{0.2}Fe_{0.8}O_3-\delta$) and LSM ($(La_{1-x}Sr_x)_{1-y}MnO_3-\delta$. The LSCF is the mixed ionic electronic conductive material, which is high electrical and ionic conductivity (10^2 and 10^{-2} S cm^{-1}) along with high oxygen diffusion properties. Typically, LSM is considered reference material because it shows good performance. [2]

2.2.2. Alkaline water electrolysis

Finite-gap alkaline WEs employ a porous separator and aqueous, e.g., 30 wt % (5 M) KOH, conducting solutions (Figure 2a). This is a proven technology and has been deployed in MW scales since the late 1950s. A well-known advantage of alkaline conditions, specifically pH > 13, is the stability of the non-platinum group metal (non-PGM) based catalysts for the OER and HER, unlike for acidic media needing platinum group metal catalysts. Typically, high surface-area Raney nickel electrodes are used in an infinite-gap alkaline electrolyzer. The use of a porous separator, such as Zircon and Perl UTP 500, calls for a large distance (>2 mm) between the anode and cathode to reduce H_2 and O_2 gas crossover, which unfortunately is accompanied by a high ohmic resistance due to the direct dependency of ionic resistance on electrolyte thickness. The latter limits the maximum current densities (jmax) that can be reached.

Typically, the jmax value for a finite-gap alkaline WE is 0.25 A/cm^2, which is too low for integration with renewables, such as wind, that need ES technologies that are able to accept current densities in the several A/cm^2 range as well as with fast dynamic responses. [4]

During the alkaline electrolysis process, initially at the cathode side two moles of alkaline solution are reduced to produce one mole of hydrogen (H_2) and two moles of hydroxyl ions (OH^-), the produced H_2 can be eliminated from the cathodic surface and the remaining hydroxyl ions (OH^-) are transferred under the influence of electric circuit between anode and cathode through the porous separator to the anode side. At the anode, the hydroxyl ions (OH^-) are discharged to produce the 1/2 molecule of oxygen (O_2) and one molecule of water (H_2O), as shown in Figure 4.[2]

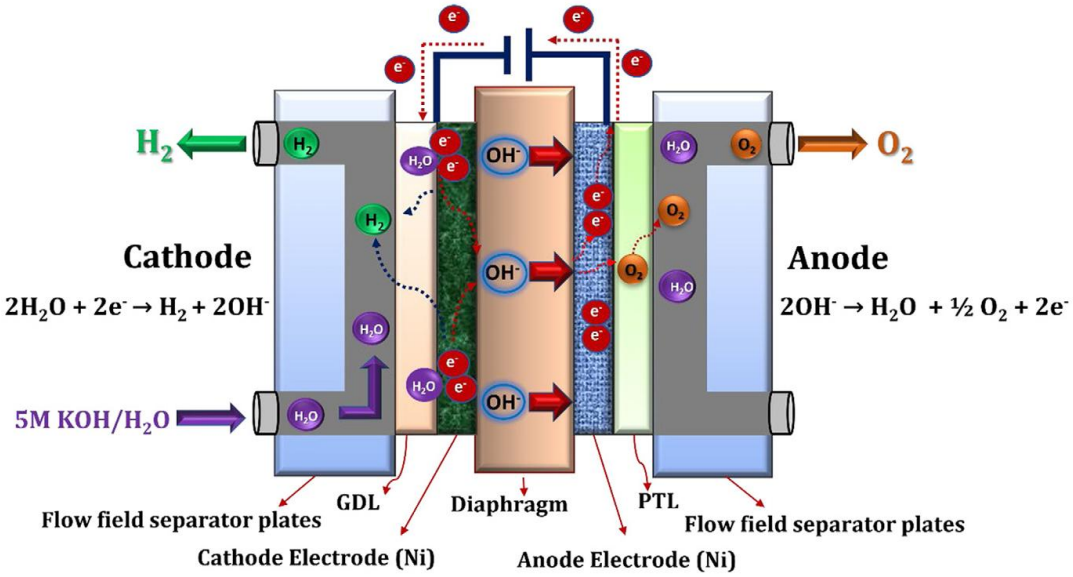

Figure 4. Schematic view of alkaline water electrolysis working principle. [2]

The major alkaline water electrolysis cell components are diaphragms/separators, current collectors (gas diffusion layer), separator plates (bipolar plates), and end plates respectively. In general, Asbestos/Zirfon/Nickel coated perforated stainless-steel diaphragms are used as separators in alkaline water electrolysis. The nickel mesh/foam is used as gas diffusion layers and stainless steel/nickel-coated stainless steel separator plates are used as bipolar and end plates respectively.

2.2.3. Proton exchange membrane water electrolysis

The zero-gap WE design reduces the internal resistance as thin polymer-based membranes of low H_2 and O_2 crossover are employed. Proton-exchange membranes (PEMs) and anion-exchange membranes (AEMs) are used for acidic (Figure 2b) and alkaline (Figure 2c) zero-gap WEs, respectively.

Consequently, zero-gap WEs are predicted to achieve higher j values than finite-gap electrolyzers. PEMWEs are much more mature than AEMWEs. This is related to the fact that PEMs, which typically consist of a perfluorosulfonic acid that is known under the trademarks Nafion and Aquivion, have a significantly higher stability than anion-exchange membranes (AEMs), although the stability of Nafion is limited to 80 °C operations. In fact, PEMWEs using a Nafion separator are typically operated at 60 °C. [4]

During the PEM water electrolysis process, initially at the anode side water molecule is decomposed to generate oxygen (O_2) and protons (H^+), and electrons (e^-). The generated oxygen eliminated from the anodic surface and the remaining protons are traveled through the proton-conducting membrane to the cathode side and the electrons are traveled through the external circuit to the cathode side. At the cathode side, the protons and electrons are recombined to produce H_2 gas. The basic principle of PEM water electrolysis is shown in Figure 5. [2]

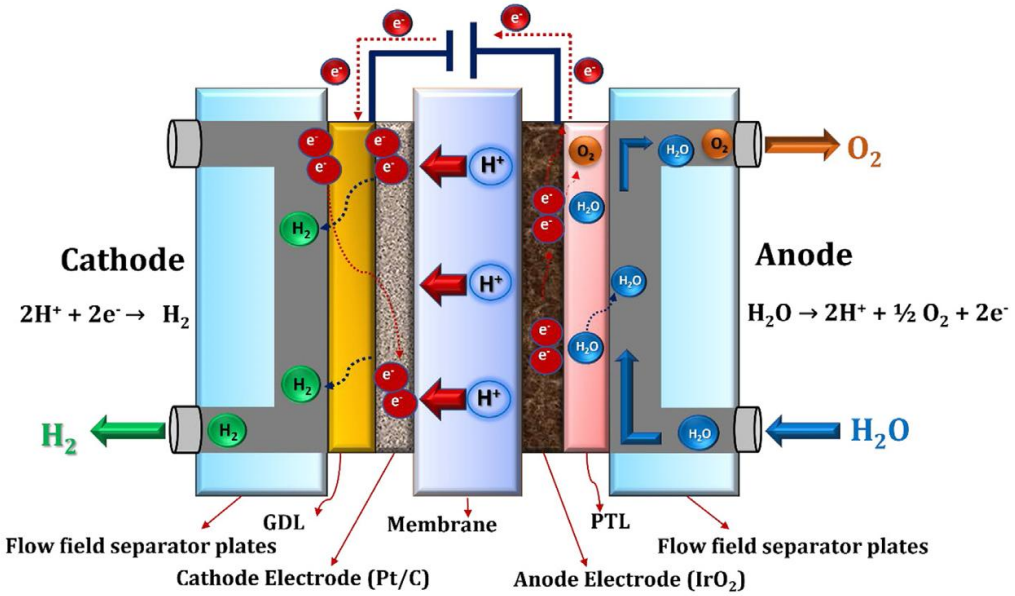

Figure 5. Schematic view of PEM water electrolysis working principle. [2]

The PEM water electrolysis cell major components are membrane electrode assembly (consist of membrane and anode, cathode electrode materials), Gas diffusion layer, separator plates (bipolar plates), and end plates respectively. Typical proton exchange membranes are Nafion®, Fumapem®, Flemion®, and Aciplex® respectively. However, most widely used membrane is Nafion® (Nafion® 115, 117, and 212), because Nafion® membrane offers several advantages such as high proton conductivity, possessing high current density, high mechanical strength, and chemical stability respectively. The state-of-the-art anode and cathode electrode materials are noble metal based electrocatalysts especially IrO_2 for the OER and carbon-supported Pt for the HER respectively. These noble metals are more expensive, and iridium is scarcer than platinum.

The porous titanium/titanium mesh and carbon cloth are used as anode and cathode gas diffusion layers. Different flow field designed bipolar plates made up of titanium material coated with platinum/gold are used as separators and endplates respectively.

2.2.4. Anion exchange membrane water electrolysis

Over the past few years, many research organizations/institutions are actively working in the development of AEMWE due to its low cost and high performance compared to the other conventional electrolysis technologies. The AEM water electrolysis technology is similar to conventional alkaline water electrolysis. However, the main difference between alkaline and AEM water electrolysis is the replacement of the conventional diaphragms with an anion exchange membrane in alkaline water electrolysis. AEM water electrolysis offers several advantages such as cost-effective transition metal catalysts being used instead of noble metal catalysts, distilled water/low concentrated alkaline solution (1M KOH) can be used as electrolyte instead of high concentrated (5M KOH solution). [2]

The electrochemical reaction consists of two half-cell reactions they are hydrogen evolution reaction (HER) and oxygen evolution reaction (OER). Initially, at the cathode side, the water molecule is reduced to generate hydrogen (H_2) and hydroxyl ions (OH^-) by the addition of two electrons. Hydrogen is released from the surface of cathode and the hydroxyl ions (OH^-) are diffused through the ion exchange membrane to the anode side by the positive attraction of the anode, while the electrons are transported through the external circuit to the anode. On the anode side, the hydroxyl ions recombine as water molecules and oxygen by losing electrons. The produced oxygen is released from the anode. The basic principle and half-cell reactions of AEM water electrolysis as shown in Figure 6.

Generally, AEM water electrolysis cell components are membrane (separator), electrode materials current collectors (gas diffusion layer), separator plates (bipolar plates), and end plates respectively. Typical anion exchange membranes are quaternary ammonium ion exchange membranes i.e., Sustanion®, Fumasep, Fumatech respectively. Commonly used anode and cathode electrode materials are transition metal based electrocatalysts especially Nickel and NiFeCo alloy materials respectively. The nickel foam/porous nickel mesh and carbon cloth are used as anode and cathode gas diffusion layers. Stainless steel and nickel-coated stainless steel separator plates are used as bipolar and end plates respectively. [2]

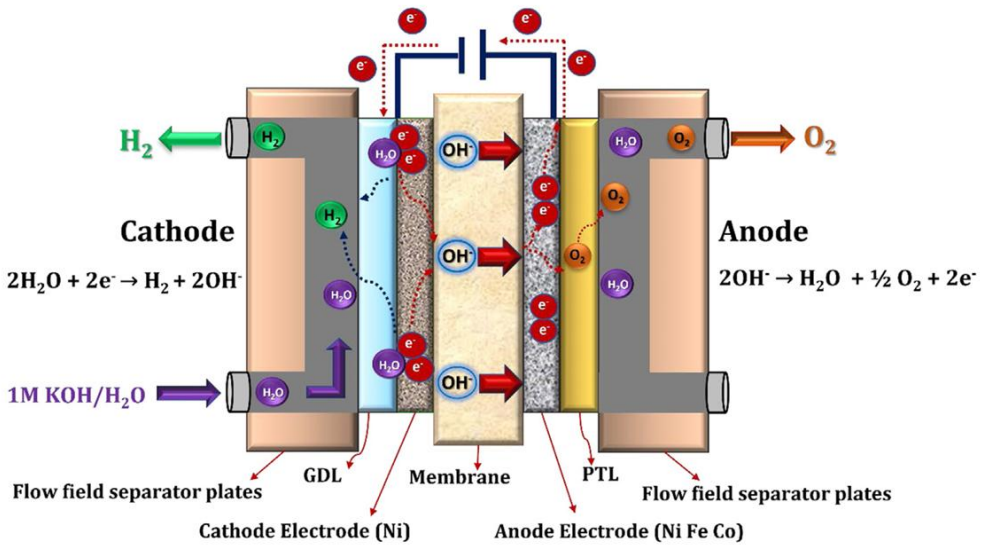

Figure 6. Schematic view of AEM water electrolysis working principle. [2]

2.3. AEM water electrolysis

2.3.1. Material selection of layers with their thermo-mechanical properties

We've seen different layers of an AEM electrolyser in the previous section. To have the cell performing properly in three major aspects which are thermal, mechanical and electrical, it's important to select the materials of all layers very carefully. The thermal aspect is related to the temperature distribution and thermal expansion among cell layers due to heat from the anodic fluid and heat of reactions. The mechanical aspect is related to pressure distribution and strain of the layers both from the fluids pressure and from the clamping pressure after assembly of the cell. The electrical aspect is related to the ability of the layers to conduct the electrons and so the electricity properly.

In the following sections, most common materials for each layer with some of their most important thermo-mechanical properties are provided for comparing them in terms of stability, performance, economical and other engineering aspects.

2.3.1.1. Anion Exchange Membrane (AEM)

Regarding AEM electrolyzers, there are relatively few studies on crossover. Some papers report data that can give a qualitative idea of the percentage to be expected with commercial membranes. In Table 4 and Table 5, some of the properties of commercial membranes for AEMEL and PEM are provided, in particular their thickness which is a relevant parameter in crossover phenomena.

The membrane is the weakest mechanically and most sensitive layer. The membrane expands due to water absorption and since it is constrained by the electrodes and gaskets, in-plane stress would be induced which leads to risk of cracking and delamination. Besides, under working temperature (70 °C), the polymeric membrane becomes softer, and it would have more deformation under the same pressure and there would be higher risk of creep for this layer. If the pressure is not perfectly balanced (30 bar at both anodic and cathodic sides), there could be the risk of membrane bulging leading to mechanical fatigue. So, following criteria must be considered when selecting the material of the membrane: low swelling, good mechanical strength at operating temperature, having compatible coefficient of thermal expansion (CTE) with adjacent layers.

Liu et al. [5] demonstrated that the Sustainion® 37-50 membrane had a lower resistance than Fumasep® FAS-50, Fumasep® FAPQ, AMI 7001, Nafion 115, or Celazole PBI using electrochemical impedance measurements. These authors obtained a current density of about 3.5 A/cm^2 at 60 °C with a 1.0 M KOH electrolyte solution, using $NiFe_2O_4$ as the anode and NiFeCo as the cathode catalysts with loadings of 2 mg/cm^2.

Pushkareva et al. [6] also demonstrated that the Sustainion® membrane had a better performance than AemionTM and Tokuyama A201 membranes at different electrolyte and temperature operation conditions, obtaining density currents higher than 3.0 A/cm^2 at 60 °C and 1.0 M KOH as electrolyte.

To prevent current leakage, the thickness of the membrane is recommended to be ≥50 μm. [5]

Company	Membrane	IEC (mmol g^{-1})	Tensile strength (MPa)	Thickness (μm)
Dioxide Materials	Sustainion 37-50		-	50
Fumatech	FAA-3-30	1.67–2.04 (Cl)	-	26–34
	FAA-3-50	1.6–2.1 (Cl)	25–40	45–55
	FAA-3-PK-75	1.2–1.4 (Cl)	30–60	70–80
Ionomr	AF1-HNN5-25	1.4–1.7 (OH)	60	25
	AF1-HNN5-50	1.4–1.7 (OH)	60	50
	AF1-HNN8-25	2.1–2.5 (OH)	60	25
	AF1-HNN8-50	2.1–2.5 (OH)	60	50
	AF2-HWP8-75-X	2.3-2.6 (OH)	32	85
Tokuyama	A201	1.7 (OH)	96	28
	A901	1.7 (OH)	-	10
Versogen	PiperION-A-20	~2.35	>30	20
	PiperION-A-80	~2.35	>50	80
Orion	TM1	2.19 (OH)	29	30
DuPont	Nafion 211	0.95-1.01	23	25.4
	Nafion 212	0.95-1.01	32	50.8
	Nafion 115	0.95-1.01	43	125
	Nafion 117	0.95-1.01	43	183

Table 4. Summary of the reported properties of AEMs and PEMs membranes. [7]

Membrane	Water Uptake (wt %)	Tensile Strength (MPa)	Elongation at Break (%)	Thermal Stability / Max Operating Temp (°C)
Fumasep FAA-3-50	10 – 25	25 – 40	45 – 55	Stable up to ~ 60 °C (tested at 60 °C in 1 M KOH; degradation rate 800 µV h^{-1} over 1000 h)
Selemion AMVN	15 ± 2	0.3	N.A.	Recommended up to ~ 60 °C (used in CO_2 electrolysis at 60 °C)
Sustainion X37-50 RT	> 80	N.A.	N.A.	Stable up to ≈ 80 °C (operated at 60 °C with < 5 µV h^{-1} degradation over 2000 h; TGA > 200 °C)
PiperIon PiperIon20	50	> 30	> 20	Stable to at least 60 °C (used at 60 °C in 1 M KOH)
AEMION AF1-HNN8-25-X	33 – 37	60	50 – 65	Stable to ≥ 60 °C (tested at 60 °C with good durability; TGA ≈ 220 °C)
Orion TMI m-TPN1	25	29	36	Stable up to ~ 60 °C (used in CO_2 electrolysis at 60 °C; decomposition onset ~ 200 °C)
Tokuyama A201	44 ± 5	96	62	Stable at 60 °C (tested in AEMWE at 60 °C for 1000 h; decomposition onset ~ 200 °C)
PurionX-131	45 – 55	100 – 120	30 – 50	Stable > 18 000 h at 80 °C in 1 M KOH (TGA decomposition > 250 °C)

Table 5. common membranes used for AEMEL. [8], [9], [10], [11]

Based on the above properties and operating conditions, the best anion exchange membranes for the high pressure AEM electrolyser are described in the Table 6.

Membrane	Reason for Priority
PurionX-131	Exceptional mechanical strength (100–120 MPa) and demonstrated long-term stability (> 18 000 h at 80 °C in 1 M KOH), making it ideal for 30 bar at 70 °C.
Sustainion X37-50 RT	Ultra-low area-specific resistance and very high ionic conductivity, though it requires mechanical reinforcement or slightly reduced pressure to handle 30 bar.
AEMION AF1-HNN8-25-X	High IEC and balanced water uptake combined with good tensile strength (≈ 60 MPa), offering solid performance at elevated temperature and moderate pressure.
Tokuyama A201	Very high tensile strength (≈ 96 MPa) ensures excellent pressure resistance; slightly lower IEC and higher water uptake may cause more swelling.
PiperIon PiperIon20	Good overall conductivity and reasonable strength (> 30 MPa) but lacks extensive long-term data above 60 °C, so further validation at 70 °C is needed.

Table 6. best AEMs for high pressure AEM electrolyser.

2.3.1.2. Catalyst Coated Electrode

Electrodes in AEM electrolyzers use non-precious catalysts (typically Ni, Ni–Fe, Ni–Co, etc.) on porous supports, plus a binder (PTFE or Ionomer) to adhere the layer. Two main configurations exist: (1) Metal substrates (e.g. Ni or Stainless Steel mesh/foam) coated or plated with catalyst; or (2) Carbon-supported layers (catalyst on carbon cloth/paper). [12]

High pressure (30 bar) and 60–80 °C operation require that catalyst particles remain adhered to the substrate; this is typically achieved by selecting binder polymers with reduced water uptake or by heat-treatment to crosslink the binder (which improves mechanical stability). [13]

The common catalysts for HER and OER reactions at cathode and anode electrodes with their characteristics are provided in Table 7 and Table 8 respectively.

Catalyst	Category	Characteristics and Notes
Pt/C (20-40 wt%)	PGM	Benchmark: low overpotential (<50 mV @ 10 mA/cm² RDE, ~100-150 mV @ 10 mA/cm² MEA); excellent durability.
PtRu/C	PGM	Enhanced CO tolerance; Pt preferred if no CO present.
NiMo Alloys (e.g., Ni_3Mo)	Ni-Mo Alloys	High intrinsic HER activity; overpotential ~50-100 mV @ 10 mA/cm² in MEA; durable if protected.
$CoNiO_2$/C	Ni-Co Oxides	Overpotential ~90-110 mV @ 10 mA/cm² RDE; higher loading (~1.6 mg/cm²) needed in MEA (~200 mV @ 1 A/cm²).
NiCu Oxides	Ni-Cu Oxides	Modulates H-binding energy; conductivity improvement; ~200-250 mV @ 1 A/cm² in MEA.
Ni/CeO_2–La_2O_3/C	Mixed Oxides	Improved kinetics; supports tailored dispersion; ~200-250 mV @ 1 A/cm² MEA.
$Fe_{0.2}Ni_{0.8}$–$P_{0.5}S_{0.5}$	Phosphide-Sulfide	Low overpotential (~70-90 mV @ 10 mA/cm² RDE); in situ oxidation to oxides; moderate durability.
VCo-P	Phosphide	Low overpotential; in situ oxidation; needs stability validation in MEA.
VN, Mo_2C, WC	Nitrides/Carbides	High conductivity; stable under HER; some form thin oxide layers.
Ni Foam Support	Support Architecture	Enhances surface area and electron transport; supports low-loading catalysts.
Oxidized Carbon Support	Support Architecture	Used for electrodeposited NiMo or other HER catalysts; enhances mass transport.

Table 7. Common HER catalysts. [14]

Catalyst	Category	Characteristics and Notes
Iridium Oxide (IrO_2)	PGM	Benchmark OER catalyst; high activity but limited stability; volatile IrO_3 formation; costly.
Ruthenium Oxide (RuO_2)	PGM	Comparable activity to IrO_2 in alkaline; less stable due to Ru dissolution.
$NiO/Ni(OH)_2$	Ni-based Oxides	Transforms to NiOOH in situ; moderate OER activity.
NiFe Mixed Oxides	Ni-based Oxides	Fe incorporation lowers overpotential; high surface area; in situ active phase formation.
$Ni_xFe_{1-x}(OH)_2$	Ni-based Oxides	Forms active NiOOH(Fe) phases; high intrinsic activity.
$Ni_{1-x}Co_xO_x$	Ni-Co Oxides	Enhanced activity; Co leaching risk under long-term OER.
$NiCo_2O_4$ Spinel	Ni-Co Oxides	Moderate OER activity; good structural robustness; mass-transport limits at high current.
Co_3O_4 Spinel	Co Oxides	Active with Fe contamination; less activity than NiFe.
CoFe Mixed Oxides	Co-Fe Oxides	Enhanced activity; needs higher loading than NiFe.
Mn-based Oxides	Mn Oxides	Lower intrinsic activity; often combined with Ni or Co to improve conductivity.
Perovskites (e.g., $LaNiO_3$)	Perovskites	Lab-scale; require high-temperature sintering; moderate activity.
Various Spinels (e.g., $MnCo_2O_4$)	Spinels	Moderate activity; serve as supports for functionalization.
Metal Phosphides (e.g., Ni_2P)	Phosphides	High conductivity; in situ oxidation forms active (oxy)hydroxides.
Metal Sulfides (e.g., MoS_2)	Sulfides	Undergoes surface reconstruction to oxides; primarily HER use.
Metal Nitrides/Carbides (e.g., TiN)	Nitrides/Carbides	Oxide layer formation under OER conditions; high conductivity.
Ni Foam + MPL Support	Support Architecture	3D Ni with NiFe/CoFe coating offers high electrical connectivity; robust.
SS Mesh/Felt Support	Support Architecture	Used with protective coatings; risk of degradation; provides structural support.

Table 8. Common OER catalysts. [14]

The most widely used catalysts used for AEMWE are transition metals such as Co, Ni, or Fe. This choice is supported by their electrochemical stability, low cost, and easy accessibility. Among the most promising non-noble catalysts, Ni and Ni-alloys, Co mixed oxides, or graphene have demonstrated a high stability and activity for the OER. Thus, in recent studies, it has been demonstrated that the addition of Fe to Ni catalysts decreases the overpotential for the OER and increases the overall reaction performance. Currently, CuCoOx, Ni-alloys, and graphene are extensively used as HER catalysts. Among them, Ni can be considered the most promising catalyst for AEMWE. [15]

Based on above tables, the preferred catalysts for OER and HER reactions are provided in Table 9.

Reaction	Catalyst	Details
OER	IrO_2 on Ti Support	Low overpotential (~250 mV @ 1 A/cm²), multi-thousand-hour stability, high cost.
OER	NiFe Mixed (Oxy)hydroxide on Ni Mesh + MPL	Overpotential ~300-350 mV @ 1 A/cm² in MEA, low cost, stable (>1000 h).
HER	Pt/C CCM	Overpotential ~50 mV @ 1 A/cm² MEA (KOH feed), durable (>10,000 h).
HER	NiMo on Ni Foam or Oxidized Carbon	Overpotential ~80-100 mV @ 1 A/cm², durable (>2000 h), requires protection.

Table 9. Preferred catalysts for OER and HER reactions

As describes before, Ionomers are needed to adhere the catalysts to the porous substrates. The common Ionomers with their characteristics are listed in Table 10.

Ionomer (Binder Type / Chemistry)	Tensile Strength	Young's Modulus	Elongation at Break	Water Uptake (23 °C / 80 °C)	Swelling (23 °C / 80 °C)
PPO-based AEI crosslinked via "thiolene" (bulky imidazolium groups)	~18 MPa (dry, 23 °C)	~1.0–1.2 GPa (dry, 23 °C)	~30–40 % (dry, 23 °C)	≈20 wt % / ≈30 wt %	≈10 % / ≈15 %
Poly(aryl piperidinium) (e.g. PDTP AEM)	≈20–30 MPa (dry, 23 °C)	≈0.23–0.30 GPa (dry, 23 °C)	≈45–60 % (dry, 23 °C)	≈25 wt % / – (extrapolate: 50–60 wt % at 80 °C)	≈5 % / ≈10–12 %
Crosslinked poly(styrene–ethylene/butylene–styrene) (SEBS) AEI	4.00 MPa (precursor) → 18.43 MPa (fully crosslinked dry)	1.0 GPa (fully crosslinked dry)	Not explicitly stated (≥20 % expected)	≈50 wt % (at 23 °C) / ≈80 wt % (at 80 °C)	≈10–15 % (at 23 °C) / ≈20–25 % (at 80 °C)
Poly(2,6-dimethyl-1,4-phenylene oxide) (PPO) – quaternized	≥60 MPa (dry, 23 °C, fluorene-linked side chain)	≥1.0 GPa (dry, 23 °C, fluorene-linked side chain)	~20–30 % (dry, 23 °C)	≈10 wt % / ≈20 wt %	≈5 % / ≈8 %
Quaternary ammonium "poly(phenylene piperidinium)"	10–20 MPa (thin film, 23 °C)	0.2–0.5 GPa (thin film, 23 °C)	~20–50 % (depending on IEC)	20–60 wt % (23 °C) / 80–100 wt % (80 °C)	10–30 % (23 °C) / 20–40 % (80 °C)

Table 10. Common Ionomers with their characteristics. [16], [17], [18], [19]

The active material (e.g. Ni $(OH)_2$, NiFe, etc.) has negligible structural strength by itself; the layer's mechanical integrity comes from the binder and substrate. [1]

Common substrate materials for catalysts with their thermo-mechanical properties are listed in Table 11. Typical anode and cathode electrodes thickness are 550 µm and 350 µm respectively. [5]

Material / Composition	Young's Modulus (GPa)	Tensile Strength (Mpa)	Elongation at Break [%]	Specific Heat Capacity [J/KgC]	Thermal Conductivity [W/mK]	CTE ($\times 10^{-6}$/K)	Alkaline Compatibility	Comments
Carbon support	171	125-165	35	134	69.1	9.1	Excellent	HER cathode
Nickel Foam / Mesh	200	317	30	440	90.9	13.4	Excellent	Mechanical support and conduction
Stainless Steel	200	520	55	470	16	16	Moderate; coating needed	May corrode; used with coatings (Ni, Au, TiN)

Table 11. Common substrate materials. [20], [21], [22]

The thermodynamic stability of Ni foam and likewise of stainless steel (SS) felts, in combination with their ability to passivize at anodic potential in alkaline media, favor their use in AEMWE as anode substrates. However, common SS 316 is likely to leach Fe into the KOH electrolyte, specifically at elevated temperatures of 80 °C and over time. Therefore, SS 316 is likely not suitable as a long-term cell material, specifically at the anode. Carbon GDLs commonly used in Fuel cells are restricted to use at the cathode in AEMWEs due to carbon corrosion in the presence of OH^- ions, which tend to operate as nucleophilic intermediates and can accelerate degradation in the highly oxidative environment of AEMWE anodes. [1]

2.3.1.3. Gas diffusion layer

Gas diffusion layers (GDL) have porous structure and when they are under pressure of the clamping bolts, they would be compressed. So, their material selection matters because they must maintain their porosity under pressure and provide uniform contact pressure. If they are too soft, they would have excessive compression which leads to pores collapse and poor transport of species. If they are too stiff, it leads to poor contact and higher contact resistance which reduces the performance of the cell.

GDLs are treated with PTFE (5–30%) for hydrophobicity. Carbon-based GDLs have porosity ≈75–90% and are chemically inert to OH^- at ≤80 °C, but they can oxidize at the O_2 anode if potential is high. Metal GDLs (Ni, stainless steel) offer superior mechanical strength and conductivity; however, austenitic stainless steels must be chosen carefully (e.g. duplex grades or coated) to avoid stress-corrosion cracking in hot KOH. For carbon-based GDLs, compression during assembly reduces thickness (Toray paper compresses only ~10%, cloth up to ~20%). [23], [24]

In PEM electrolyzers, due to the high potential, oxygen-rich and strong acidic environment on the anode side, expensive titanium-based material GDL is often used. In AEM electrolyzers, due to the weak alkaline conditions, the anode GDL usually uses cheap nickel foam, and the cathode can use nickel foam or carbon cloth, which greatly reduces the cost. [25]. In Table 12, the most common GDL materials with some of their thermos-mechanical properties are provided.

Material	Elongation at Break [%]	Tensile Strength [MPa]	Elastic Modulus (GPa)	Specific Heat Capacity [J/KgC]	CTE ($\times 10^{-6}$/K)	Thermal Conductivity (W/m·K)	Alkaline Compatib-ility	Comments	Thickness [mm]
Carbon fiber paper (e.g. Toray TGP)	-	70	-	-	-0.8	23 @100 °C (in-plane)	Stable at 60–80 °C	Hydrophobic, in-plane conductive	0.5
Nickel Foam/ Sintered Ni	30	317	200	440	13.4	90.9	Excellent	Strong, used especially at anode	0.5
Stainless Steel Mesh (316L)	55	520	200	470	16	16	Risk of SCC above 80 °C	May need coating; robust	0.2-0.5

Table 12. Common GDLs materials with their thermo-mechanical properties. [22], [26], [5], [21], [24]

2.3.1.4. Bipolar Plate

Main purposes of bipolar plates are as follows; Current conduction where the electrons transfer between adjacent cells through bipolar plates and so it acts as an electrical pathway with low resistance and if it has poor conductivity, it leads to higher ohmic losses and lower efficiency.

Second purpose of bipolar plates is flow distribution where the flow channels are included in the bipolar plates and they distribute KOH solution at the anode side and removes H_2 gas

at the cathode side and if there is non-uniform flow through these channels, it leads to local drying or flooding and causes performance loss.

The third purpose is mechanical support which it acts as a load-bearing plate for the whole cell due to clamping force and internal forces of high-pressure fluids. It also provides safety for the cell as it prevents mixing of H_2 and O_2 gases.

Finally, it helps the heat management of the cell as it conducts heat away from the reaction zones and reduces the thermal gradients through the components which leads to lower thermal stress for the layers.

The bipolar plates should be corrosion-resistant and have high electrical conductivity. Typical materials for the bipolar plates immersed in the cell alkaline environment are titanium and nickel, although nickel is particularly recommended. [23]

316L stainless steel is another commonly used material, but high-pressure AEM operation (30 – 40 % KOH at 70 –80 °C, O_2 side pressure ~30 bar) has caused SCC in 316L. Duplex steels or high-Ni alloys (e.g. Alloy 28) are preferred for withstanding these conditions. [8]

Common materials for bipolar plates with their thermo-mechanical properties are listed in Table 13.

Material	Tensile Strength (MPa)	Young's Modulus (GPa)	Fatigue Strength [MPa]	Elongation at Break [%]	Thermal Conductivity [W/mK]	Specific Heat Capacity [J/kgK]	CTE ($\times 10^{-6}$/K)	Chemical Compatibility	Comments	Thickness [mm]
Stainless Steel 316L	520	200	270	55	16	470	16	Forms passive film	Stress Corrosion Cracking in hot KOH at >80 °C, low cost	0.3-1
Duplex Stainless Steel 2205	740	200	370	28	15	480	13	Highly resistant	Excellent for high pressure/temperature	0.3-1
Nickel Alloy 28	570	200	220	45	12	470	16	Excellent	Used for harsh alkaline O_2 exposure	0.5-2
Titanium Grade 2	420	110	250	23	22	540	9	Excellent	Corrosion resistant but costly	0.3-1

Table 13. Common bipolar plate materials. [27], [28], [29], [30], [31], [21]

2.3.1.5. Gasket

The material of the gasket must be chosen in a way that it maintains the sealing under temperature increase and pressure cycles. If it is too stiff, it leads to poor sealing and potential leakage and if it is too soft, it could face over compression which leads to extrusion or failure. As it is usually a non-metallic material, its thermal expansion coefficient must be compatible with adjacent layers like metallic bipolar plates, otherwise the mismatch could lead to loss of sealing properties of the gasket.

One of the most common materials for gaskets is called PTFE. While PTFE is chemically inert and has excellent sealing properties, it can be stiff and prone to creep (deformation under load). This can lead to a loss of sealing force and potentially leaks. Adding fillers like Grafoil, glass, carbon, or other materials to PTFE increases its mechanical strength, resistance to creep, and wear resistance, especially when dealing with high pressures or temperatures. They are also called Structured PTFE. Glass-Filled PTFE Gaskets are ideal for applications requiring high compressive strength. Expanded PTFE gaskets, also known as ePTFE gaskets, are manufactured by expanding PTFE under controlled conditions. This process creates a highly conformable, flexible gasket material that excels in demanding sealing applications. These gaskets exhibit excellent chemical resistance and can withstand aggressive fluids, including acids, solvents, and acidic substances. Furthermore, they can operate effectively across a broad temperature range, typically from -450°F to 600°F (-268°C to 315°C), making them suitable for extreme environments. [32]

Another suitable gasket material for AEM electrolyser is called EPDM which is rated *“Excellent”* with KOH up to ~50 °C. At 80 °C KOH, EPDM will age and swell; it is generally avoided for hot AEM use. [33]

Common gaskets with their thermo-mechanical properties are listed in Table 14.

Material	Young's Modulus (MPa)	Tensile Strength (MPa)	Shear modulus [MPa]	Elongation (%)	Specific Heat Capacity [J/KgK]	CTE ($\times 10^{-6}$/K)	Thermal Conductivity [W/mK]	Temp Range (°C)	Alkaline Compatibility	Comments	Thickness [mm]
EPDM Rubber	6	13-17.5	-	375-400	2000	-	0.2-0.26	–40 to ~120	Excellent up to 50 °C KOH; degrades at 80 °C	Common but avoided at high T; resilient under compression	0.8-3
PTFE	575	30.5	230	450	1000	80	0.24	–200 to ~260	Excellent (inert)	-	0.25-0.35
FFKM (Kalrez®, etc.)	12.4	16-18.6	-	125-170	974@100°C	229	0.18 @ 100 °C	Up to >200	Excellent	Chemically inert; very low swelling; expensive	-

Table 14. Common gasket materials. [5], [34], [35], [36], [37], [38], [39]

2.3.1.6. Current collector

Current collectors provide low-resistance electrical paths. The current collector sits between the bipolar plate and the end plate and collects and distributes electrons between external circuit and the electrodes where the electrochemical reactions occur. Its function is spreading current evenly across the electrode surface. Without current collector, current might concentrate locally which leads to hot spots, uneven reaction rates and accelerated degradation.

The suitable material for current collector must have low electrical resistance, good thermal conductivity, mechanical stability under compression and corrosion resistance in alkaline environment.

Nickel (or Ni-coated steel) is preferred for anion cells due to good KOH stability. Copper, while very conductive, is not stable in hot KOH unless coated with a more noble metal. Graphite (carbon) plates are chemically stable but must be thick/wired to handle currents.

Stainless steel can serve as current-collecting substrates if alloys (duplex or high-Ni) resist caustic SCC. [40]

The common materials for current collectors with their thermo-mechanical properties are listed in Table 15.

Material	Elongation at Break [%]	Young's Modulus (GPa)	Tensile Strength (MPa)	Thermal Conductivity [W/mK]	CTE ($\times 10^{-6}$/K)	Specific Heat Capacity [J/KgK]	Alkaline Stability	Thickness [mm]	Comments
Copper	60	110	210	385	16.4 @100°C	385	Poor: dissolves as $Cu(OH)_2$ in KOH	2	Must be coated if used
Nickel	30	207	317	60.7	13.1@20°C	460	Excellent	2	Preferred; corrosion-resistant
Graphite / Carbon	–	4.8	–	24	0.6-4.3 @20°C	707.7	Excellent	2-4	Light and inert; weak mechanically
Stainless Steel (316L)	55	200	520	16	16	470	Moderate	2	OK if duplex or coated

Table 15. Common materials for current collectors. [41] ,[42], [43], [44], [21]

2.3.1.7. End plate

End plates are located at the outermost sides of the stack and connected by bolts. They receive the bolt preload and distribute it across bipolar plates, GDLs and other inner components. Their function is to ensure uniform compression of the entire stack. They hold all components together under internal pressure and thermal expansion and ensure that gaskets are properly compressed and maintain all layers aligned.

The material of end plates must have high Young's modulus and tensile strength to provide uniform pressure distribution. Otherwise, there might be over-compression regions at the edges of the membrane causing membrane damage and under-compression regions at the centre of the membrane causing high contact resistance which all lead to performance loss and possible mechanical failure.

Like other components of the cell, end plates must have good thermal conductivity and compatibility of its CTE with other layers to avoid potential risks due to thermal expansion.

Common materials for end plates with their key highlights are listed in Table 16.

Material	Key Highlights	Thickness [mm]
Stainless Steel 316L	Excellent resistance in alkaline media; suitable for AEM environments; substantial safety margin at 30 bar; good thermal conductivity for heat dissipation; moderate CTE reduces thermal stress mismatches.	25
Nickel	Very good corrosion resistance in alkaline and moderately acidic media; resists pitting; safe stress margin at 30 bar; high thermal conductivity aids heat spreading; lower CTE reduces thermal stress mismatches.	25-30
Titanium Grade 2	Outstanding corrosion resistance in alkaline and chloride-rich electrolytes; lower density reduces stack mass; easily sustains 30 bar; moderate thermal conductivity; low CTE minimizes thermal stress mismatches, especially if adjacent hardware is Ti-compatible.	20-25

Table 16. Common materials for end plates. [45]

2.3.2. Different possible cell configurations

Considering the performance, price and availability of materials in markets, 4 different configurations for the cell layers have been determined in following sections.

2.3.2.1. The best performance configuration

In this configuration, the performance of materials has been prioritized rather than price and availability in commercial markets. So, we can see what the material for each layer would be if we want to have the cell with its best performance.

The material selected for each layer is shown in Table 17 and the reason for each selection is described afterwards.

Layer	OER Catalyst	HER Catalyst	Membrane	GDL	Bipolar Plates	Current Collectors	End Plates	Gasket
Material	IrO_2 on Ti Support	Pt/C CCM	PurionX131 Or Sustainion X37-50 RT	Nickel Foam	Titanium Grade 2	Nickel	Titanium Grade 2	PTFE

Table 17. The best performance configuration

IrO_2 on Ti Support:

- IrO_2 is the benchmark OER catalyst offering low overpotential (~250 mV @ 1 A/cm^2) compared to NiFe which is ~300-350 mV @ 1 A/cm^2.

- Titanium support ensures corrosion resistance and mechanical robustness at high pressure and temperature.

Pt/C CCM:

- Pt/C offers the best HER performance with low overpotential (~50 mV @ 1 A/cm^2) and very long durability (>10,000 h), while the overpotential for NiMo is ~80-100 mV @ 1 A/cm^2.

PurionX131 and Sustainion X37-50 RT:

- Exhibits exceptional mechanical strength (100–120 MPa) which is higher than other membranes mechanical strength (e.g.: for Tokuyama A201 = 96 MPa) and very high stability (>18,000 h at 80 °C in 1 M KOH). Sustainion X37-50 RT is also a good option since there are some experiments by researchers showing its great performance.

Nickel Foam as GDL:

Most of the thermos-mechanical properties of nickel are almost the same as stainless steel, but in terms of corrosion resistance in alkaline condition, nickel performs much better than

stainless steel and so it is a better material for having good performance in the long term. The electrical conductivity of nickel is also higher than stainless steel. (14.3 MS/m compared to 7.3 MS/m). [46]

Titanium Grade 2 as bipolar plates and end plates:

- Titanium Grade 2 is Used for both bipolar plates and end plates for its outstanding corrosion resistance in alkaline media compared to nickel and SS 316.
- High strength-to-weight ratio and moderate thermal conductivity support long-term stack stability.

The densities of titanium, SS 316 (stainless steel 316), and nickel are: Titanium: approximately 4.51 g/cm^3, SS 316: approximately 8.0 g/cm^3, and Nickel: approximately 8.90 g/cm^3 [47] and the mechanical properties of these three metals are all high enough to stand operating pressure, so with titanium we can have the required mechanical strength with almost half weight compared to nickel and SS 316.

Thermal conductivity of titanium is 540 J/KgK which is higher than both nickel and ss316 (around 470 J/KgK).

Nickel as current collector:

- Nickel is Preferred as current collector due to its high electrical conductivity and excellent resistance to alkaline corrosion.

Resistance Values (Approximate, in ohm-meters) [48]:

- Copper: 1.7 x 10^-8
- Nickel: 6.99 x 10^-8
- Stainless Steel (316L): 7.4 x 10^-7
- Graphite/Carbon: 10^-5 to 10^-6 (highly dependent on grade and processing)

The electrical resistance of copper is lower than nickel but is not stable in hot KOH unless coated with a more noble metal.

PTFE as gasket:

- Structured or filled PTFE resists creep and is widely used in high-pressure environments.

EPDM is rated *"Excellent"* with KOH up to ~50 °C. At 80 °C KOH, EPDM will age and swell; it is generally avoided for hot AEM use.

FFKM is mechanically weaker than PTFE. (FFKM tensile strength is around 17 MPa while for PTFE is 30.5 MPa).

2.3.2.2. The cheapest configuration

In this configuration, the price of the materials has been prioritized rather than performance and availability in commercial markets. So, we can see what the material for each layer would be if we want to have the cheapest cell.

The material selected for each layer is shown in Table 18.

Layer	OER Catalyst	HER Catalyst	Membrane	GDL / PTL	Bipolar Plates	Current Collectors	End Plates	Gasket
Material	NiFe Mixed (Oxy)hydroxide on Ni Mesh	NiMo on Ni Foam	PiperIon PiperIon20	Stainless steel mesh	SS 316L	SS 316L	SS 316L	PTFE

Table 18. The cheapest configuration

In Table 19, the cost of cheapest material for each layer is provided with the cost of their alternative that has higher cost.

Layer	Chosen Material (Cost)	Higher-Cost Alternative (Cost)
OER catalyst	$Ni^{+}Fe$ mixed (oxy)hydroxide on Ni mesh: ~ € 80 /kg	IrO_2 (high-surface-area nano powder): ~ € 400/g
HER catalyst	Ni–Mo alloy on Ni foam: ~ € 60 /kg	Pt/C : (Pt metal ≈ € 39/g)
Membrane	PiperION A-20 (20 µm) : ~ € 16 /100 cm² sheet	Sustainion X37-50 (50 µm): ~ € 90 /100 cm² PurionX -131 (45 µm) : ~ € 30 /100 cm²
GDL / PTL	Type 316 Stainless Steel Wire Cloth : ~ € 15 /(70 × 70 cm)	Nickel foam: ~ € 63 (50 × 50 cm with 1 mm thickness sheet)
Bipolar plates	SS 316L plate: ~ € 3.8 /kg	Nickel alloy: ~ € 19 /kg
Current collectors	SS 316L foil: ~ € 4 /kg	Cu plate (uncoated): ~ € 8 /kg
End plates	SS 316L: ~ € 4 /kg	Nickel alloy: ~ € 19 /kg
Gasket	PTFE: ~ € 173 /100×100 mm with 10mm thickness sheet (~ € 29 /m²)	FFKM resin cost runs 255–510 € per kilogram (very expensive)

Table 19. Cost of materials. [49], [50], [51], [52], [53], [54], [55], [56], [57], [58], [59], [60], [61]

2.3.2.3. The balanced configuration

In order to have a balance between price and performance of materials, this configuration is determined. The selected material for each layer is shown in Table 20. The reasons for each material selection is described afterwards.

Layer	**OER Catalyst**	**HER Catalyst**	**Membrane**	**GDL / PTL**	**Bipolar Plates**	**Current Collectors**	**End Plates**	**Gasket**
Material	NiFe Mixed (Oxy)hydroxide on Ni Mesh	NiMo on Ni Foam	Sustainion X37-50 RT	Nickel Foam	Duplex Stainless Steel 2205	Nickel-coated Stainless Steel	Duplex Stainless Steel 2205	PTFE

Table 20. The balanced configuration

Catalyst layers:

For catalyst layers, using Pt and Ir increases a lot the cost while their effect on overpotential reduction isn't significant compared to Ni based catalysts. So, using NiFe for OER catalyst and NiMo for HER catalyst is a good compromise between cost and performance.

Membrane:

The cost difference between Sustinion X37-50 RT and PiperION isn't very high, while there're enough experiments by researchers showing the great performance of Sustainion which makes it a reliable option for membrane.

GDL:

Electrical conductivity and corrosion resistance are key characteristics of a GDL which can be better achieved by using nickel foam instead of stainless steel although nickel foam is more expensive.

Bipolar Plate:

While stainless steel has low corrosion resistance and titanium has very high cost, Duplex Stainless Steel 2205 is a compromise between these two metals making it ideal for using as a bipolar plate. It's more corrosion resistant compared to stainless steel and has a lower price compared to titanium. (6.3 € /Kg). [62]

Current Collector:

Due to higher electrical conductivity and corrosion resistance of nickel and lower cost of stainless steel, a good combination could be using nickel as coating on stainless steel for current collectors.

End Plates:

Since the thickness of end plates is higher than other layers, using titanium for end plates increases the cost a lot. So, a good solution is using Duplex Stainless Steel 2205 which is cheaper and has better resistance to corrosion compared to stainless steel 316.

Gaskets:

It's been discussed before the reason for priority of PTFE compared to other options, making it the most widely used gasket.

2.3.2.4. The commercial configuration

In this configuration, the availability in commercial markets of the materials has been prioritized rather than performance and price. So, we can see what the material for each layer would be if we want to have the commercially available cell.

The material selected for each layer is shown in Table 21 and the reason for each selection is described afterwards.

Layer	OER Catalyst	HER Catalyst	Membrane	GDL	Bipolar Plates	Current Collectors	End Plates	Gasket
Material	NiFe Mixed (Oxy)hydroxide on Ni Mesh	NiMo on Ni Foam	Sustainion X37-50	Nickel foam	Nickel-coated stainless steel	Gold coated copper	Stainless steel 316	PTFE

Table 21. The commercial cell configuration

Catalyst layers:

Commercial AEM stacks are designed to use non-precious metals throughout. for example, Enapter notes that its AEM design does not require high-cost noble metal catalysts. [63]

Although it's not stated that they're using Nickel based catalysts, since no other data was found, we can consider the nickel-based catalysts as in the table for OER and HER reactions.

Membrane:

A study was done for commercial membranes for AEMWE [64] indicating that among the mentioned membranes, the Sustainion X37-50 has the highest performance.

GDL:

Nickel foam is commonly used for anode while both nickel foam and carbon paper can be used for cathode side. [65]

Bipolar plates:

Most developers use stainless steel plates, typically coated or plated with nickel for additional corrosion protection. [66], [65]

Current collectors:

Commercial AEM stack designs often use stamped copper or copper-alloy plates. It may be nickel or gold-plated to prevent oxidation. [65] , [67]

End plates:

AEM modules use thick machined steel end-plates to bolt the stack together. [66], [65]

3 Cell Design Study

3.1. Clamping Pressure

This section outlines the step-by-step method for calculating the clamping force in an Anion Exchange Membrane Electrolyzer (AEMEL). The calculation is based on an equivalent stiffness model, with a focus on single cell and stack analysis. The effects of temperature difference between the operational mode and the assembly condition and initial gaps between the Membrane Electrode Assembly (MEA) and sealant are incorporated.

The assembly technique is one of the key techniques to ensure the stack having a long lifetime and high reliability. The clamping load affects the lifetime and performance of the stack system in several ways. Too large a clamping load may cause some components in the stack to produce a stress high enough to give rise to plastic deformation even cracks, while an unreasonable small clamping load may produce a high contact electrical resistance at the interface of the gas diffusion layer (GDL) and the bipolar plate (BPP), and also may cause leakage of water and gases in the seal interfaces. It should also be pointed out that even though a reasonable initial clamping load had been given in the assembly process at room temperature, either the contact electrical resistance or the seal interface pressure or the structure stress may be out of the allowed region of the design due to the thermal deformations of the electrolyser components under working conditions. To overcome those problems occurred during the stack running, the stiffness of both the clamping components and the clamped components have to be optimized.

The basic idea of the following technique to calculate the clamping pressure is first to assume the stack system consisting of a large number of elastic elements (springs) in either series or parallel connections. For each spring, the stiffness coefficient can be obtained using material mechanics analysis for the simple period structures or using FEA for the complex structures. Then a system analysis technique is used to give the optimal design for each structure component in the stack. [68]

3.1.1. Basic model descriptions and assumptions

Stiffness of a solid body is the resistance offered by an elastic body to deformation. Its value depends on the material property, the structure, shape and size, and the boundary conditions of the solid body. As shown in Figure 7, for an elastic bar under tension or compression, the axial stiffness is:

$$k = \frac{EA}{L} \quad (1)$$

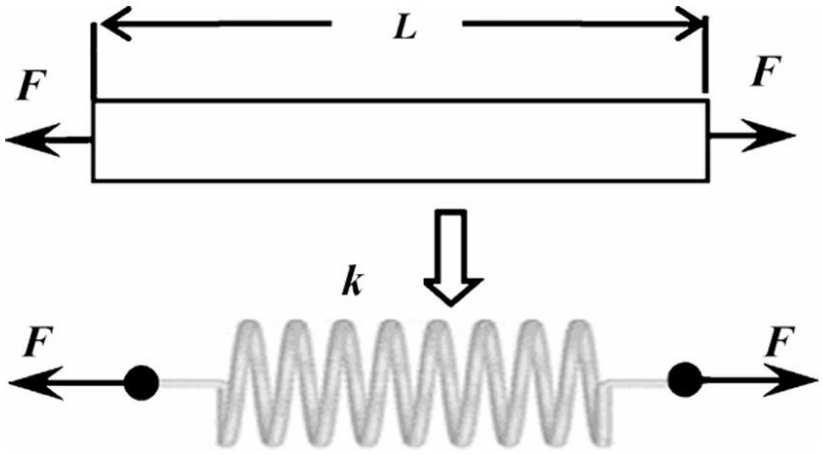

Figure 7. Schematic of the axial equivalent stiffness of an elastic element. [68]

Where k is usually called the equivalent stiffness, E is the elastic modulus, A is the cross-section area, L is the length of the bar along the axial direction.

For a complex structure, the equivalent stiffness cannot be directly calculated using the above equation. A common approach is to simplify the structure into an equivalent model composed of elastic elements typically spring arranged in parallel or series. The deformation of the structure under a given load can then be determined using this simplified equivalent model. The whole stack can be divided into several basic components whose stiffness can be calculated by Eq. (1) according to the load bearing characteristics of the structures along the direction of the clamping load.

Assumptions:

Proper assumptions are needed before building the equivalent stiffness model. For simplification and theory analysis strictness, the following assumptions are stated:

(1) The endplates are treated as rigid body and have an enough high mechanical strength. Although an ideal rigid endplate is difficult to obtain in practice, an endplate with a suitable design can be considered as rigid one approximately.

(2) Each clamping bolt bears the same clamping load and gives the same elongation during assembly.

(3) The bipolar plate has N parallel flow channels, while the number of the bipolar plate ribs is (N−1).

(4) As shown in Figure 8, the bipolar plate is divided into three regions: the BPP-sealant, the BPP-rib and the BPP-base.

(5) MEA is considered as the sandwich structure: GDL+PEM (proton exchange membrane) +GDL.

(6) It is assumed that there are no gaps at the connection interfaces of the stack before assembly, i.e., all the MEA and sealants have the same thickness.

(7) The assembly process is accomplished at room temperature.

(8) This model has been developed for a PEM fuel cell stack, but since the overall structure of the PEM fuel cells and AEM electrolysers are the same regarding the clamping pressure, it's been also used in our study for AEM stacks.

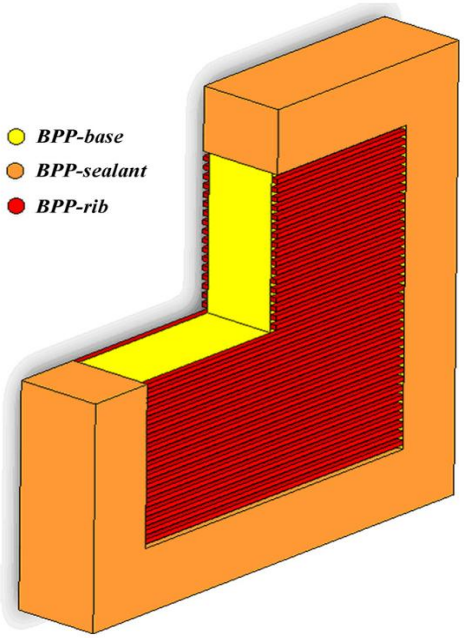

Figure 8. Schematic of the three regions of the bipolar plate. [68]

3.1.2. Single cell equivalent stiffness

As Figure 9 depicts, a single cell consists of three types of components: a membrane electrode assembly, two bipolar plates and the sealants. They are all included in the following equivalent stiffness model of the single cell.

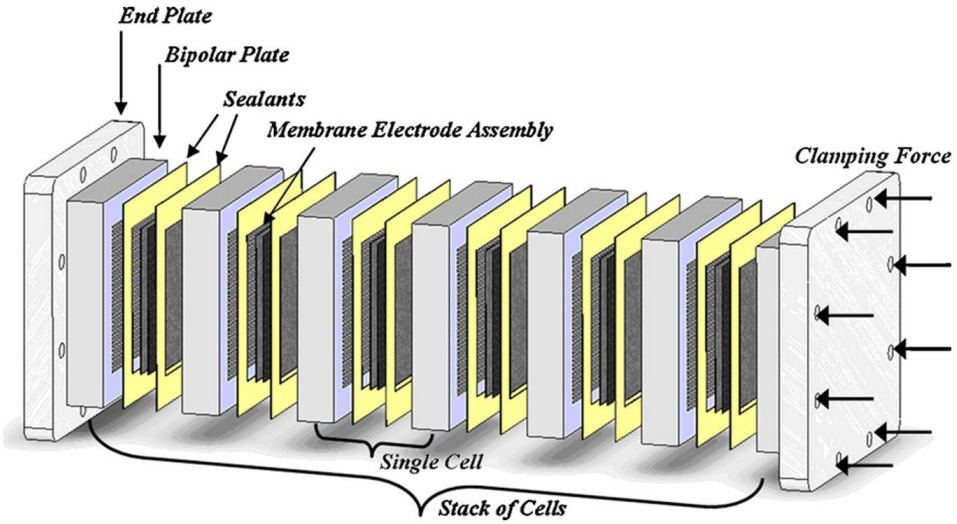

Figure 9. Schematic of the stack hardware. [68]

From the view perpendicular to the flow channels, we have a mechanical equivalent stiffness model of the single cell as shown in Figure 10, where δ equals the thread pitch times the pretightening cycles of the nuts, and the arrow Z represents the positive direction of the vectors such as displacement or load. The stiffness of each spring in the model equals the equivalent stiffness of the basic component, so called the assembled component.

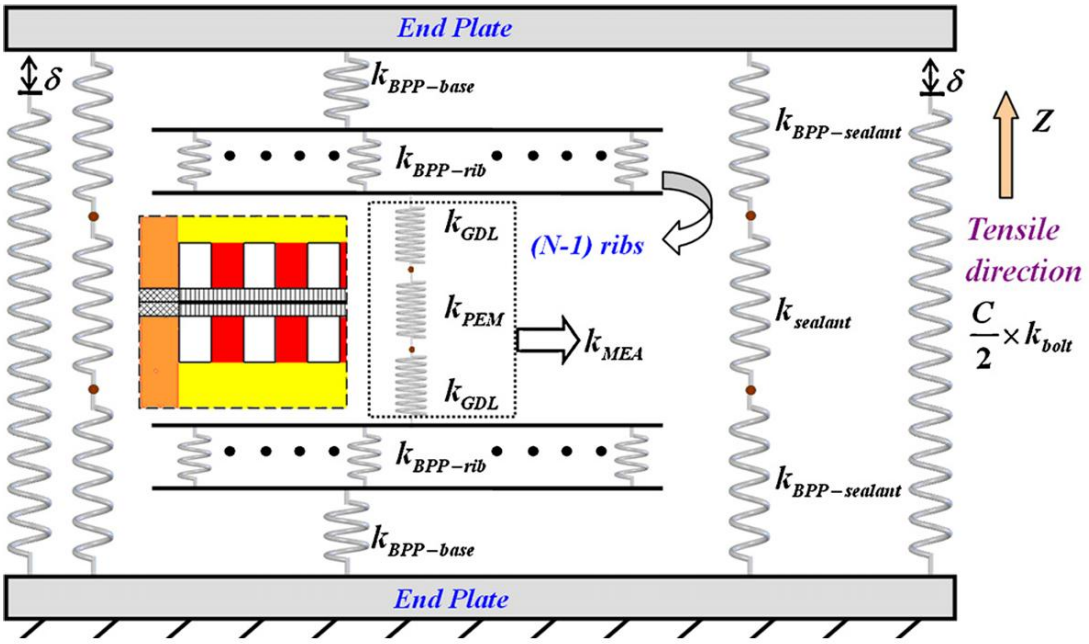

Figure 10. Schematic of the equivalent stiffness model of the single cell. [68]

Based on assumption (2), we can make further simplification for the system as shown in Figure 11.

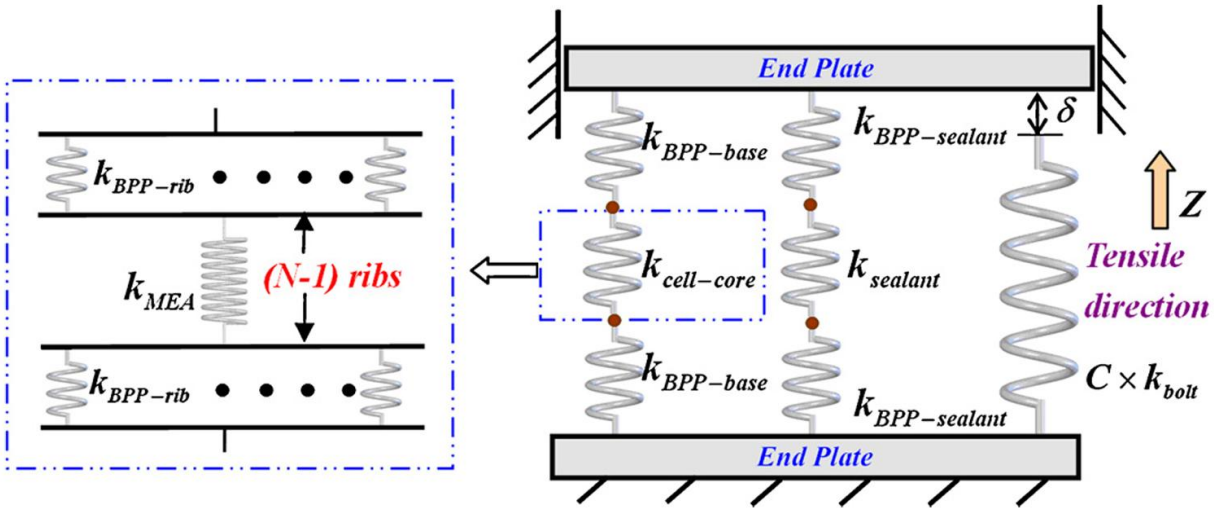

Figure 11. Schematic of the simplified equivalent stiffness model of the single cell. [68]

Subsequently, the equivalent stiffness model can be finally simplified by combining the stiffness of the BPP-sealant and the sealant (basic components) in series as the assembled component: external-cell and combining the stiffness of the BPP-base and cell-core in series as the assembled component: internal cell. After those simplifications, the system of

one single cell can be simplified as what is shown in Figure 12. It consists of two end plates, C clamping bolts, the internal-cell and the external-cell.

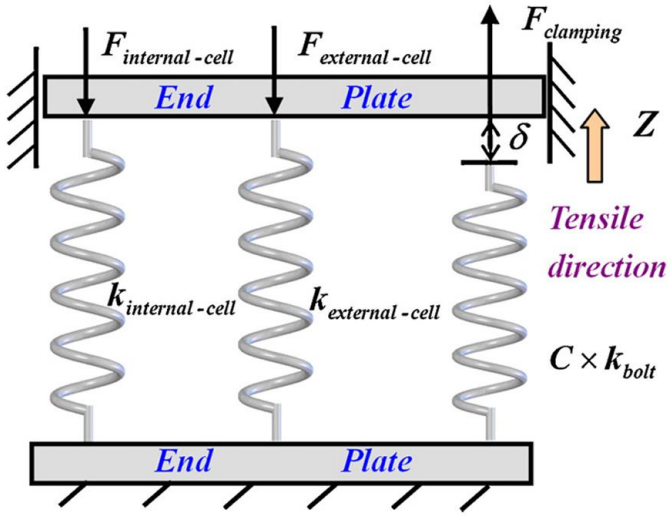

Figure 12. Schematic of the final equivalent stiffness model of the single cell. [68]

Based on this model, the equivalent stiffness of a single cell is given:

$$k, single\ cell\ =\ k, internal\_call + k, external\_cell \tag{2}$$

where k is the equivalent stiffness corresponding to the component. For the internal-cell, an assembled component, the equivalent stiffness can be calculated as:

$$k, internal\_cell = \frac{1}{\frac{2}{k,BPP\_base} + \frac{1}{k,cell\_core}} \tag{3}$$

where the equivalent stiffness of the assembled component cell core is:

$$k, cell\_core = \frac{1}{\frac{2}{(N-1)* k,bipolar\_rib} + \frac{1}{k,MEA}} \tag{4}$$

The equivalent stiffness of the MEA is:

$$k, MEA = \frac{1}{\frac{2}{k,GDL} + \frac{1}{k,AEM}} \tag{5}$$

In the same way, for the assembled component external-cell, the equivalent stiffness can be calculated as follows:

$$k, external\_cell = \frac{1}{\frac{2}{k,bipolar\_sealant} + \frac{1}{k,sealant}} \tag{6}$$

Based on the conditions of compatible displacement and static load equilibrium in Z direction (clamping direction), the deformation of the whole single cell under the clamping load is:

$$Z^F, single\_cell = -\frac{C\ k,bolt}{C\ k,bolt+k,single\_cell}\delta \quad (7)$$

Where Z^F single-cell is a negative number indicating the structures are under compression since δ is positive for bolt stretching. Then the clamping loads applied on the single cell are:

$$F, internal\_cell = k, internal\_cell\ Z^F, single\_cell \quad (8)$$

$$F, external\_cell = k, external\_cell\ Z^F, single\_cell \quad (9)$$

The total clamping load applied on the single cell is the sum of F internal-cell and F external-cell, which equals the load applied on the clamping bolts.

$$F, clamping = F, internal\_cell + F, external\_cell \quad (10)$$

3.1.3. Sensitivity analysis

To assess the effect of changing the main parameters on the clamping force of a single cell, a sensitivity analysis is done. For the basic components of a single cell and their required parameters for calculating the clamping force, the following table is considered as a case study. The varying parameters are k,bolt, k,internal_cell, k,external_cell and δ.

Basic component	BPP-base	BPP-rib	BPP-sealant	sealant	GDL	AEM	bolt
material	Titanium grade 2	Titanium grade 2	Titanium grade 2	PTFE	Nickel foam	PurionX-131	Stainless steel 316
Elastic modulus [GPa]	110	110	110	0.575	200	2	200
Area [m^2]	0.0025	$0.35*10^{-4}$	0.0024	0.0024	0.0025	0.0025	$58*10^{-6}$
Thickness [m]	$3.2*10^{-3}$	$0.4*10^{-3}$	$4*10^{-3}$	$0.7*10^{-3}$	$0.5*10^{-3}$	$1*10^{-3}$	$70*10^{-3}$

Table 22. Required data for calculating the clamping force

Considering the data on the table and assuming 8 M10 bolts, 10 ribs for each bipolar plate and $\delta = 10\ \mu m$, we can obtain:

k,internal_cell = 3.965 GN/m

k,external_cell = 1.86 GN/m

k,bolt = 0.166 GN/m

F,clamping,tot = 10.79 KN

for sensitivity analysis, the range of 0.5-2 of the main values for varying parameters are considered. (Figure 13)

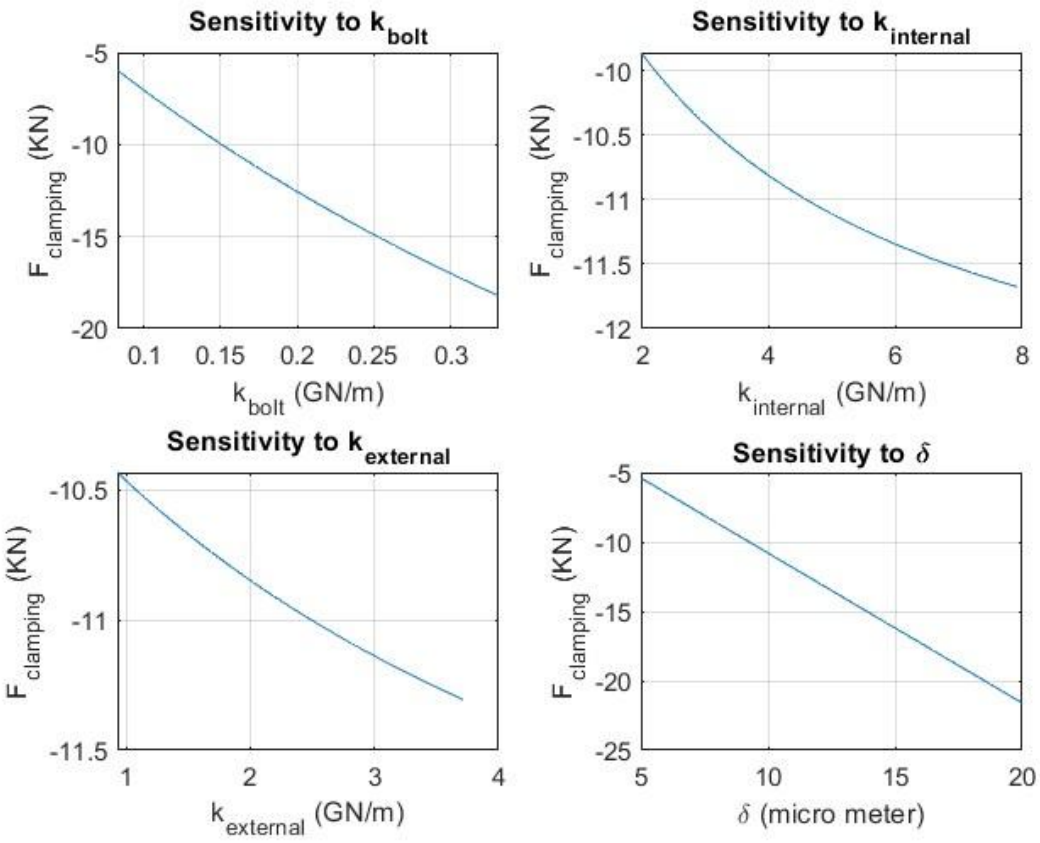

Figure 13. Sensitivity of clamping force to varying parameters

It's clear that δ and k,bolt have significant effect on the clamping force and for cell components, the internal components have higher effect.

To assess the effect of all the basic components' stiffness on the clamping force, another sensitivity analysis is done. (Figure 14)

It's notable that sealant and AEM stiffness have a higher impact on the clamping force than other basic components, meaning that these non-metallic components must be selected more carefully.

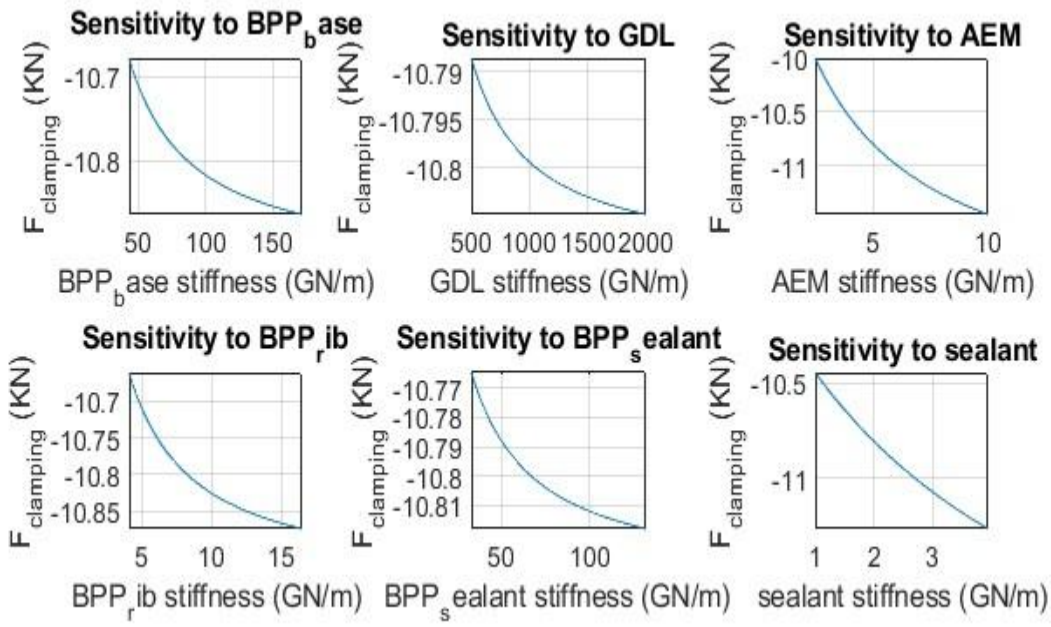

Figure 14. Sensitivity of clamping force to basic components' stiffness

3.1.4. Optimum clamping pressure

The optimal clamping pressure for AEMWE devices typically ranges from 1.5 to 3.0 MPa. [19]

Excessive compression (>3 MPa) risks membrane puncture, GDL collapse and mass-transport losses, whereas insufficient compression (<1.5 MPa) can lead to poor sealing and heightened contact resistance. Whether we're tightening a single AEM cell or a multi-cell stack, each MEA still wants roughly 2.8–3.0 MPa across its active area to minimize contact resistance and prevent leaks. In the following parameters regarding the clamping of the cell will be assessed and each of them could be a way to validate the sufficient clamping of the electrolyser devices.

The force applied on each bolt is:

$$F, bolt = \frac{F, clamping, tot}{n} \quad (11)$$

where n is the number of bolts. The stress applied on each bolt is:

$$\sigma, bolt = \frac{F,bolt}{A,s} \quad (12)$$

where A,s is the tensile stress area of the bolt and $\sigma, bolt$ must be lower than allowable stress of the bolt material.

The clamping pressure can be obtained by:

$$P, clamping = \frac{F,clamping,tot}{A,membrane} \quad (13)$$

This is also another parameter that can be used to check if the bolts tightening is enough for having both good performance and sealing.

In our case study, the resulting pressure would be:

$P = \frac{F,clamping}{A,membarne} = \frac{10.79\ KN}{0.0025} = 4.3\ MPa$; which is slightly higher than the upper limit, so different parameters should be optimized to reach the best range of pressure.

Finally, the bolt torque can be obtained by:

$$T = K\ d\ F, bolt \quad (14)$$

Where K is the torque coefficient which is typically 0.15 – 0.25 for steel bolts and is usually selected as 0.2 in articles and d is the nominal diameter of the bolt.

3.1.5. Stack stiffness and clamping force

The AEMEL stack is comprised of numerous cells connected via bipolar plates. For this cyclic cell characteristic, stiffness of the whole stack can be obtained by combining the single cell equivalent model in sequence. Figure 15 depicts the equivalent clamping stiffness model of a stack. Therefore, the equivalent stiffness model of the stack can be simplified as the similar model shown in Figure 12. But here it is composed of the following components: two endplates, C clamping bolts, the internal-stack and the external-stack. Now the stack stiffness can be written:

$$k, stack = k, internal\_stack + k, external\_stack \quad (15)$$

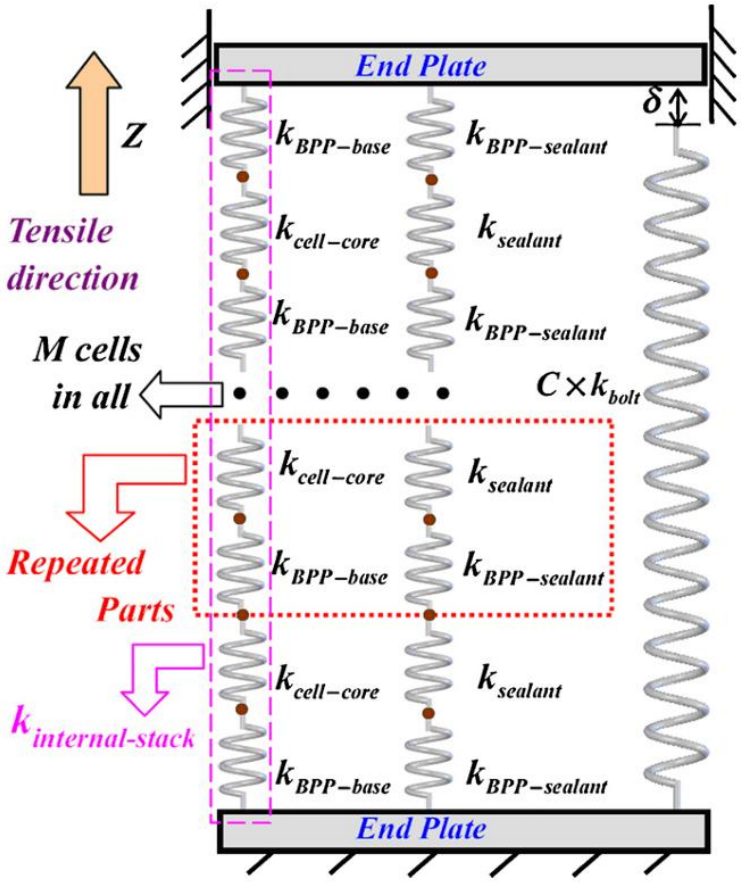

Figure 15. Schematic of the equivalent stiffness model of the stack. [68]

Where the stiffness of the internal-stack and the external-stack can be calculated as follows:

$$k, internal\_stack = \frac{1}{(M+1)*\frac{1}{k,bipolar\ plate\_base}+M*\frac{1}{k,cell\_core}} \quad (16)$$

$$k, external\_stack = \frac{1}{(M+1)*\frac{1}{k,bipolar\ plate\_sealant}+M*\frac{1}{k,sealant}} \quad (17)$$

By using the same formulas of the single cell and substituting the stack equivalent stiffness, the deformation and clamping force of the stack could be obtained.

$$Z^F, stack = -\frac{C\ k,bolt}{C\ k,bolt+k,stack}\delta \quad (18)$$

$$F, internal\_stack = k, internal\_stack\ Z^F, stack \quad (19)$$

$$F, external\_stack = k, external\_stack\ Z^F, stack \quad (20)$$

$$F, clamping = F, internal\_stack + F, external\_stack \quad (21)$$

3.1.6. Effect of temperature

Thermal expansion affects deformation and internal stress. When the temperature is changed by ΔT, the free axial thermal deformation will be:

$$\Delta L = \alpha \Delta T L \tag{22}$$

The thermal stress will be generated inside the structure if this deformation is fully or partially constrained.

As shown in Figure 16, the thermal deformation of the whole fuel cell stack can be obtained based on the compatible displacement and static load equilibrium conditions:

$$Z^T, stack = \frac{C\ k,bolt\ Z^T,bolt+k,internal\_stack\ Z^T,internal\_stack+k,external\_stack\ Z^T,external\_stack}{C\ k,bolt+k,internal\_stack+k,external\_stack} \tag{23}$$

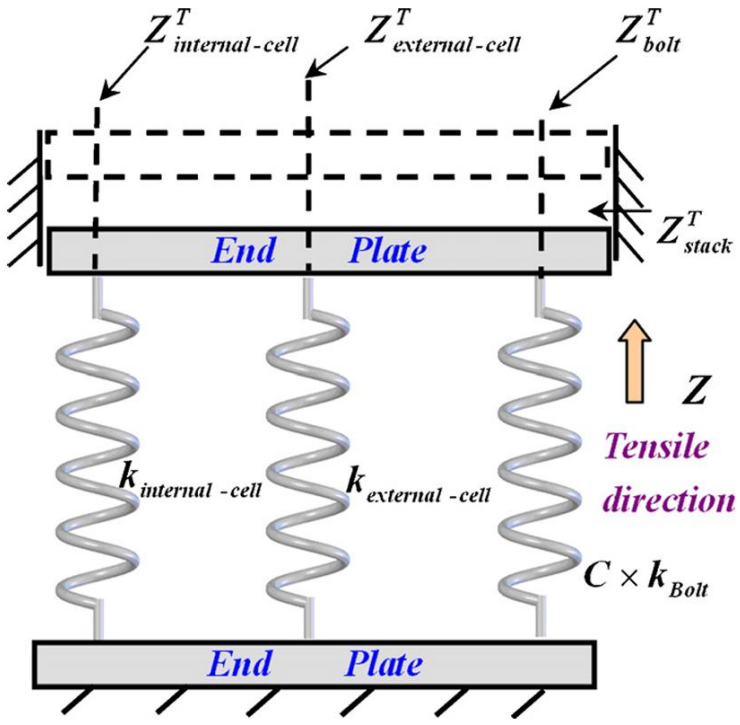

Figure 16. Schematic of the equivalent stiffness model of the stack when considering the thermal effect. [68]

Where the thermal deformation of internal and external stack can be obtained by following formulas:

$$Z^T, internal\_stack = (M+1)Z^T, BPP\_base + MZ^T, cell\_core \quad (24)$$

$$Z^T, external\_stack = (M+1)Z^T, BPP\_sealant + MZ^T, sealant \quad (25)$$

Where the thermal deformation of the cell core is the sum of the thermal deformation of an AEM, two GDLs and two bipolar plates ribs. The thermal deformation of basic components (Z^T) should be calculated using the formula for free axial deformation.

By considering the temperature effect, the combined loads applied on the stack are:

$$F, internal\_stack = k, internal\_cell\ Z^F, stack + k, internal\_stack(-Z^T, internal\_stack + Z^T, stack) \quad (26)$$

$$F, external\_stack = k, external\_cell\ Z^F, stack + k, external\_stack(-Z^T, external\_stack + Z^T, stack) \quad (27)$$

So, the total force applied on the stack in operational mode which must be restrained by clamping bolts is the sum of two above forces.

3.1.7. Effect of gap between MEA and sealant

What is discussed above is based on the assumption that there is no gap before assembling at either the interface between the bipolar plate and the MEA or the interface between the bipolar plate and the sealant. This is only an ideal case. In practice, there are usually small gaps before assembling at one of the interfaces mentioned above.

In the case of unequal thickness of the MEA and the sealant before assembly, the bipolar plate will first contact with either the sealant or the GDL. It is assumed that all the cells have the same gap, Z^F initial, defined as below:

$$Z^F, initial = L, MEA\ -\ L, sealant \quad (28)$$

Where L,MEA and L,sealant are the thickness of the MEA and the sealant, respectively. When Z^F,initial is positive, the gap occurs at the interface of the sealant and the bipolar plate; but when Z^F, initial is negative, the gap occurs at the interface of the MEA and the bipolar plate. Here the total pretightening displacement of the clamping bolts is:

$$\delta, \text{total} = \delta, \text{initial} + \delta, \text{fasten} \quad (29)$$

Where δ, initial is the pretightening displacement occurring before the gap vanishes at the initial stage of the assembly, δ,fasten is the design displacement variable of the clamping bolts after gaps vanish. In the case of L,MEA>L,Sealant, we have (see Figure 17a):

(a)

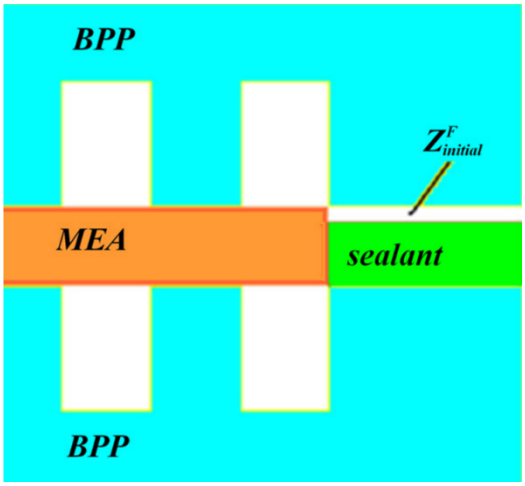

(b)

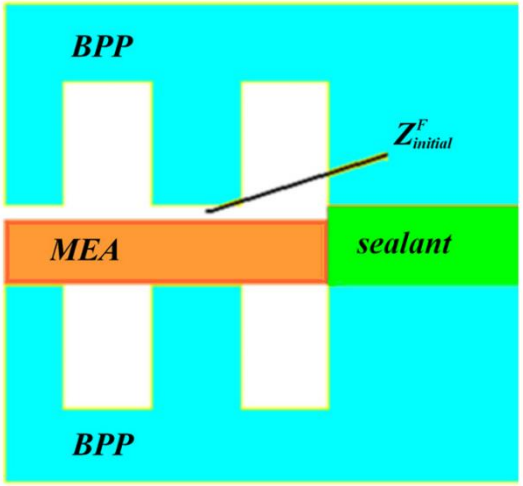

Figure 17. Schematic of the unequal thickness of the MEA and sealant before assembly: (a) a gap exists at the interface of the sealant and the BPP; (b) a gap exists at the interface of the MEA and the BPP. [68]

$$\delta, \text{initial} = \frac{MZ^F, initial(Ck,bolt+k,internal\_stack)}{C\ k,bolt} \quad (30)$$

And the total deformation of the whole stack can be obtained:

$$Z^F, total = -(MZ^F, initial) + Z^F, stack = -(MZ^F, initial) - \frac{C\ k,bolt}{C\ k,bolt+k,stack}\delta, fasten \quad (31)$$

where $Z^F, stack$ denotes the whole stack deformation after the gap vanishes.

Here the clamping load applied on the stack structure is:

$$F, internal\_cell = k, internal\_stack\ Z^F, total \quad (32)$$

$$F, external\_cell = k, external\_stack\ Z^F, total \quad (33)$$

And the total force of the clamping bolts for the whole stack is obtained by summing these two forces.

In the case of L,sealant>L,MEA, we have (see Figure 17b):

$$\delta, \text{initial} = -\frac{MZ^F, initial(Ck,bolt+k,internal\_stack)}{C\ k,bolt}$$

(34)

and the total deformation of the whole stack is:

$$Z^F, total = (MZ^F, initial) - \frac{C\ k,bolt}{C\ k,bolt+k,stack}\delta, fasten \quad (35)$$

The clamping load applied on the stack structure is calculated the same as first situation.

The effect of tolerance of different layers could be assessed in this part where it could increase or decrease the thickness of layers and consequently the gap between the mentioned interfaces leading to different clamping forces for the same stack.

3.2. Selection of proper geometry for high pressure AEMEL

Designing a high-pressure AEM electrolyser is not just about choosing materials. It's heavily driven by geometry. At 30 bar, geometry directly affects mechanical integrity, sealing reliability, pressure distribution, electrical resistance, and fluid management. If the geometry is poorly selected, even the best materials will fail.

There are various cell designs for the high-pressure AEM electrolysis; in some designs, only the cathode is pressurized for the high-pressure hydrogen generation; therefore, in the anode chamber, the water can be circulated with an ordinary pump and the handling with the high pressurized oxygen can be eliminated by this means. In another design, both the anode and the cathode semicells are pressurized so that the high-pressure differentiation on the cell components especially on the sensitive membrane is discarded. In both designs, the vulnerable polymeric membrane must be supported with an appropriate type of the material and the design. [69]

In the following sections, three different common cell configurations are described and some important cell aspects like pressure tolerance and safety, mass transport, thermal management and cooling efficiency and leak prevention at high pressure are assessed.

Then, the effects of geometric parameters of layers on the performance of the cell are assessed which the effects of bipolar plate and gaskets are further described under separate sub-chapters as they have much more impact compared to other layers.

3.2.1. Tubular design

Analogue to the planar cell design, the anode, cathode and membrane form the tubular AEM electrolysis cell. The arrangement however is concentric, a tubular membrane separates the inner from the outer half cells as shown in figure 18. [70]

While the outer half-cell can be handled similar to planar cells, the tubular geometry implies constraints concerning catalyst application and electrical connection for the inner half-cell.

The electrical current needs to be conducted towards the electrical connection at the end of the cell. For an inline production by co-extrusion, which fabricates an endless MEA, established catalyst application methods such as spray or blade coating on the membrane need a high effort and are hardly applicable. However, a porous transport electrode (PTE) approach with a separate catalyst application onto the porous transport layer enables the inline production by co-extrusion.

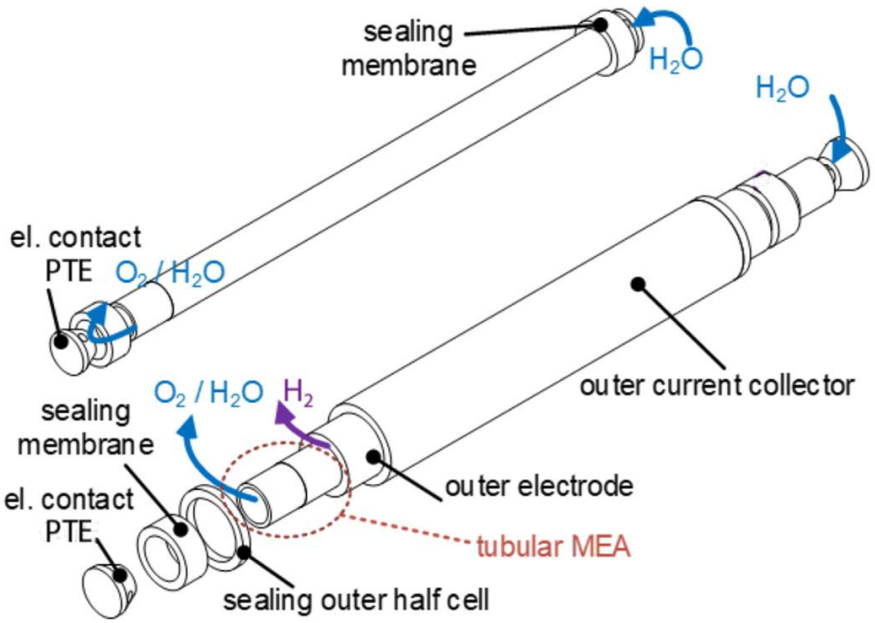

Figure 18. Top: Tubular MEA with sealing and connection. Bottom: Complete tubular cell. [70]

While in planar cells the mechanical force, which is needed to connect the components electrically, can be achieved by an outer clamping force, the electrical connection in tubular cells can be achieved by the geometrical compression of the PTE. The cathode PTE is compressed from 950 µm to 500 µm which corresponds to a compression rate of 47%. [70]

Some of the advantages of tubular design are: Tubular cells are naturally resistant to internal fluid loads. Research into coaxial configurations has demonstrated the ability to reach pressures of 100 bar or more by leveraging the structural strength of the cylindrical geometry. They avoid the massive endplates of planar designs and can be integrated directly into high-temperature steam or water lines.

Some of the disadvantages of tubular design are: The primary drawback is the complexity of manufacturing. Depositing uniform catalyst and membrane layers onto curved surfaces requires advanced techniques like dip coating or thermal spraying. Furthermore, the volumetric power density of tubular stacks is generally lower than that of planar designs.[71]

3.2.2. Circular design

Circular configurations are frequently used in modular systems and research-grade AEM electrolyzers, such as those developed by Enapter. Round bipolar plates are stacked horizontally or vertically, often housed within a cylindrical pressure vessel.

The circular geometry is inherently optimal for high-pressure containment. Mechanical stresses are distributed uniformly along the circumference, minimizing localized deformation and seal failure. Circular stacks can utilize simpler, more economical O-ring seals rather than custom-molded gaskets. [72]

Smaller circular modules (e.g., Enapter's 2.4 kW single core) can be quickly assembled into larger "multicore" systems, providing high redundancy and the ability to adapt to fluctuating renewable energy inputs. [73]

In circular stacks, O-rings are the preferred sealing solution due to their reliability under high pressure. These must be engineered with materials that resist "explosive gas decompression" (EGD), where high-pressure hydrogen absorbed into the seal material expands rapidly during pressure fluctuations, leading to internal fractures. [74]

The circular-shaped flow fields have advantages over the other flow fields because they offer more homogeneous pressure on the active area. However, the distribution of water becomes difficult at higher surface areas. [69]

3.2.3. Planar design

The planar configuration is the standard for most commercial electrolyzer stacks, including large-scale PEM and alkaline systems. Rectangular or quadratic plates are stacked vertically or horizontally and held together by massive endplates and tie rods.

This design is highly modular and allows for high active area utilization (up to 2000 cm^2 per cell in some PEM variants). Manufacturing is standardized through stamping or photochemical machining of flat sheets. [75]

Rectangular designs suffer from non-uniform stress distribution, particularly at the corners. To operate at high pressure (e.g., > 30 bar), they require thick, heavy endplates to prevent bowing of the stack and to ensure a homogeneous pressure distribution across the gasket surfaces.[76]

For planar stacks, precision-molded rubber gaskets are required to compensate for manufacturing tolerances in the bipolar plates. Gaskets must maintain their sealing performance across extreme temperature ranges (from -60 °C to +200 °C) and resist "creep" or deformation under the continuous mechanical load required to maintain electrical contact between the cell components. High-pressure back-up rings are often used to prevent the extrusion of elastomeric seals through the gaps between the bipolar plate and the cell frame at pressures up to 800 bar. [77]

The geometry of the electrolyzer stack must also manage the heat generated by electrochemical losses. In high-pressure AEM systems, temperature uniformity is vital to prevent localized degradation of the polymer membrane. Sharp spatial and transient gradients of overpotential, current density, and temperature within planar cells can lead to high thermal stress and increased degradation rates. These gradients are often exacerbated by the interconnect geometry. For instance, in rectangular stacks, the areas near the water inlet may be significantly cooler than those near the gas outlet, leading to non-uniform swelling and potential delamination of the MEA. [78]

Overall, if our target is extreme pressures where every leak or local stress could be critical (pushing to +100 bar differential as a design goal), we should consider a round cell outline or add rounded corners plus reinforced frame to reduce stress concentrations, but this may complicate packing efficiency. The literature indicates that either approach can work if the mechanical design and materials (membrane, seals, endplate stiffness) are addressed. When manufacturability, area-efficiency, and stackability are priorities and the design includes stiff endplates, sealing and mechanical design to handle the pressure, the planar design is suggested. The tubular design represents a specialized solution for ultra-high pressure environments, offering the best structural integrity at the cost of manufacturing complexity and lower volumetric power density.

3.3. Selection of proper design for layers

3.3.1. Gaskets

Modern high-pressure AEM electrolyzers increasingly utilize high-grade engineering plastics for cell frames to reduce weight and avoid the formation of "sludge" common in metallic frames. For high-pressure AEM systems, reinforced thermoplastics like PSU and PPSU are preferred due to their dimensional stability and impact strength. However, designers must account for the lower Young's modulus compared to steel; under high hydrostatic pressure, these plastic frames can deform radially, potentially compromising the stack seal. [79]

Different sealing structures for PEMFC that can be adapted to electrolyzers are as follows:[80]

3.3.1.1. Direct-sealed (face gasket) frame

A simple face gasket compressed in the inactive (non-active) edge region of the MEA. In many implementations a *double* sealing is used: (1) a gasket pressed *directly onto the membrane* (first seal) and (2) a ring/gasket compressed between the MEA and the bipolar plate (BPP) (second seal). The schematic of this frame is shown in Figure 19.

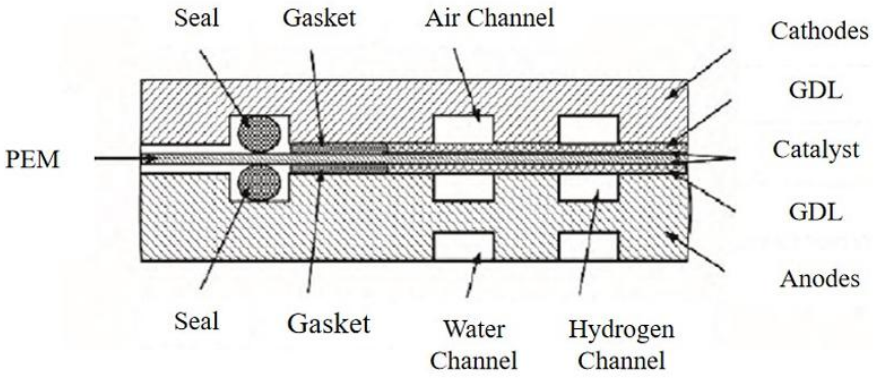

Figure 19. direct sealing structure. [80]

Advantages:

- Very simple to design and manufacture.
- Easy to disassemble and reassemble (good for R&D and frequent servicing).
- Lower cost and simpler supply chain (standard gasket materials).

Disadvantages:

- Poor performance at high differential pressure: intended for *low* to moderate pressures (leakage and extrusion risk increase with ΔP).
- Gasket sits in direct contact with membrane, so, material compatibility is critical (neutral, non-reactive materials required); wrong choice can damage the membrane.
- Localized sealing failures can occur if gasket contact pressure is non-uniform (sensitive to assembly errors).
- Its typical applications are Lab single cells, prototyping, low-pressure stacks.

3.3.1.2. Rigid (protective) wrapped frame

A rigid frame (plastic, resin or metal) placed/formed around the MEA edge; the rigid frame and protective layers (e.g., PTFE sheets) are compressed to provide sealing. Often a rubber gasket is added on top of the rigid frame face to improve sealing with the BPP.

The schematic of this frame is shown in Figure 20.

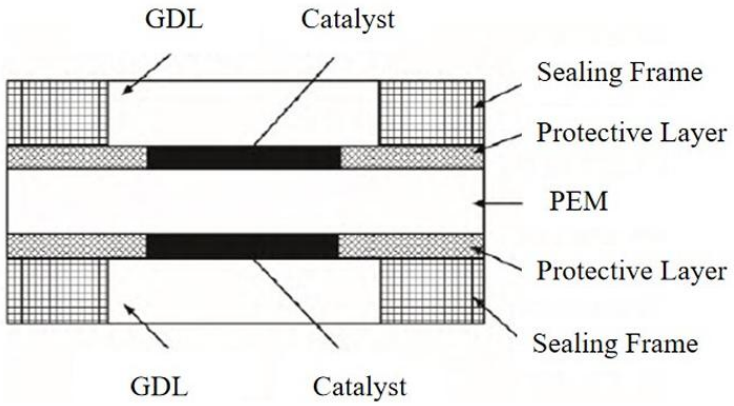

Figure 20. rigid protective frame sealing structure. [80]

Advantages

- Better mechanical protection of the membrane (reduces damage from over-compression).
- Can maintain good sealing at higher temperatures and pressures relative to direct-seal (more robust), so it is used in demanding applications.
- Easier to control contact pressure distribution with a designed rigid frame.

Disadvantages

- More complex manufacturing tolerances (frame size/flatness matter).
- Gaps between rigid frame and BPP can permit gas overflow unless secondary gaskets are used.
- Higher cost and more difficult to rework in the field than simple gaskets.

Its typical applications are higher-performance stacks, automotive fuel cells (the review mentions usage in automotive systems (e.g., industry examples like Hyundai NEXO-class applications), where mechanical robustness and higher operating pressures are required.

3.3.1.3. Seal-wrapped PEM frame (plastic frame bonded to PEM)

The PEM outer edge is fixed into a plastic frame via injection molding (the frame becomes an integrated sealing rim). The molded frame mates with the BPPs and forms the main sealing element. The schematic of this frame is shown in Figure 21.

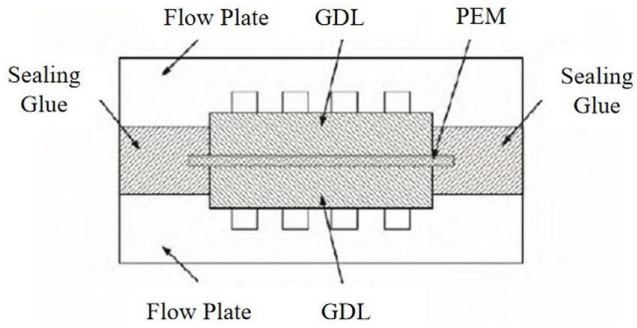

Figure 21. PEM-wrapped frame sealing structure. [80]

Advantages

- Excellent for mass production and stack assembly (the integrated frame simplifies alignment and reduces assembly variability).
- Can reduce contact resistance and be tuned through material choice (thermoplastic selection) and geometry.

Disadvantages

- Difficult to repair (integrated part means a leak often requires replacing the MEA/frame assembly).
- Injection molding parameters and material selection must be tightly controlled (thermal stress, chemical compatibility).

Its typical applications include industrial and high-volume production stacks, where rework is less frequent and factory assembly quality is prioritized. Potentially suitable for higher-pressure systems if frame material and geometry are designed accordingly.

3.3.1.4. Seal-Wrapped Membrane Electrode-Type Frame

The sealing material (adhesive, light-curing sealant) wraps the MEA edge and often penetrates into the GDL/catalyst layer, producing a soft, integrated frame around the active region; sometimes a *flow-shaped* sealing member is formed that bonds MEA edge to flow-field plate. The schematic of this frame is shown in Figure 22.

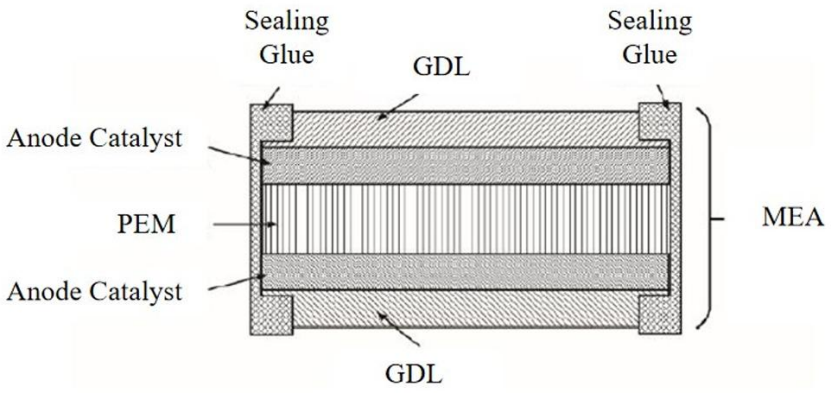

Figure 22. MEA-wrapped frame sealing structure. [80]

Advantages

- Very good sealing performance and chemical/corrosion resistance. The sealant penetration increases contact uniformity and robustness.
- High power-density potential and good stability in extreme conditions (suitable for harsh/industrial environments).

Disadvantages

- Manufacturing complexity (special adhesives, light-curing steps, controlled injection) and high equipment cost.
- Difficult to repair or re-disassemble (integrated soft frames are effectively permanent).
- Under operating heat/pressure the sealant can melt/penetrate further (beneficial to sealing but must be controlled to prevent degradation of active layers).

Its typical application includes industrial, aerospace, underwater, or other environments where leak-tightness and chemical resistance are critical and maintenance is limited. Also, when maximum power density and minimized internal leakage are prioritized.

For ≥30 bar differential and electrolyzer safety, we should prefer rigid wrapped frames or injection-molded / MEA-wrapped integrated frames (better resistance to extrusion/leakage than simple face gaskets).

If we must use face-gaskets in planar high-pressure electrolyzers, we should design anti-extrusion features (deep grooves, tongue-and-groove or dovetail profiles if possible), controlling clamp torque precisely and using higher-stiffness endplates.

3.3.2. Bipolar Plates and flow channels

The bipolar plate (BPP) serves as the mechanical backbone of the electrolyzer stack and the conduit for fluid and electrical transport. The geometry of the flow fields inscribed on these plates is a critical factor in managing bubble dynamics and ensuring uniform reactant distribution, especially in high-pressure environments where gas volume changes drastically. [81]

Structural Parameters: Width, Depth, and Rib Ratio

The optimization of channel geometry involves a delicate balance between pressure drop, water transport, and electrical contact.

Channel Depth and Width: The depth of the flow channel has the most profound impact on the pressure drop across the cell. While deeper channels (e.g., > 1.5 mm) reduce the power required for pumping, they may lead to inefficient bubble removal and stagnant zones where gas can accumulate. Narrower, shallower channels (e.g., 1 mm depth and 3 mm width) have been identified as optimal for minimizing pressure drop while maintaining high flow velocity to sweep away generated oxygen and hydrogen bubbles. [82]

Rib-to-Channel Ratio: The ribs of the bipolar plate provide electrical contact with the Porous Transport Layer (PTL). A high rib-to-channel ratio improves electrical conduction and mechanical support for the MEA but reduces the active surface area exposed to the reactant flow. Optimization studies suggest that maximizing the ratio of channel width to rib width, in conjunction with high PTL permeability, yields the best performance by facilitating the Solid-Liquid-Gas three-phase catalytic reactions. [83]

Flow Field Patterns

The spatial arrangement of channels, whether parallel or serpentine, dictates the uniformity of the electrochemical environment across the cell. Since the planar design was found to be the proper geometry for high pressure AEM electrolyser, the flow field patterns related to circular designs are not assessed in this section.

Parallel Flow Fields: Parallel channels offer the lowest pressure drop and are the simplest to manufacture. However, they suffer from flow maldistribution; if gas bubbles block one channel, the fluid redistributes through others, leading to hot spots and localized drying of the membrane.

Serpentine Flow Fields: Continuous zigzag paths ensure that any obstructions are eventually cleared by the pressure of the fluid. This pattern is standard for smaller research-scale AEM stacks (e.g., 5 cm^2 or 10 cm^2 units) because it maximizes reactant contact and water management. The primary downside is the high pressure drop, which scales poorly with larger active areas, requiring more robust and energy-intensive pumping systems.[81]

The serpentine flow field has three common categories which are single serpentine, double serpentine and triple serpentine. To better understand the effect of these designs on the cell performance, in the following, the results of an article comparing all these four flow fields are provided. [84]

All flow field areas were equivalent to the active electrode area, which is 10 cm^2, with channels approximately 2 mm wide and 3 mm deep. The illustration of these flow field designs is shown in Figure 23.

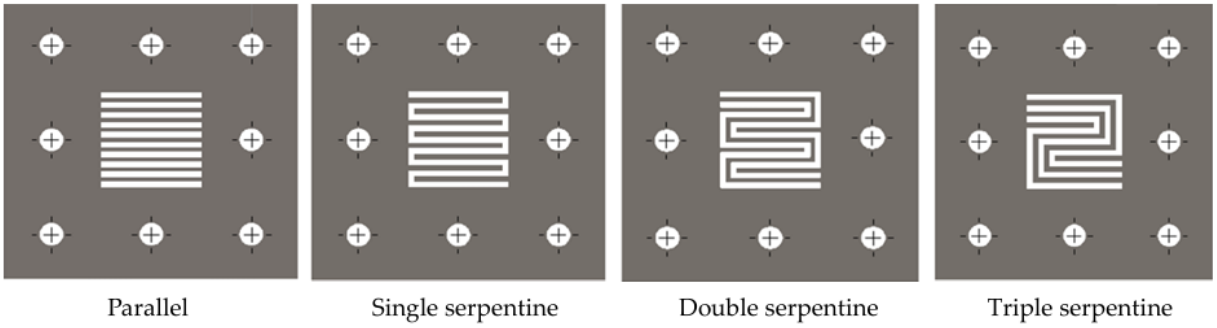

Figure 23. Illustration of flow field designs. [84]

The performance (current-voltage curve) of the cell assembled with different flow channel designs is reported in Figure 24.

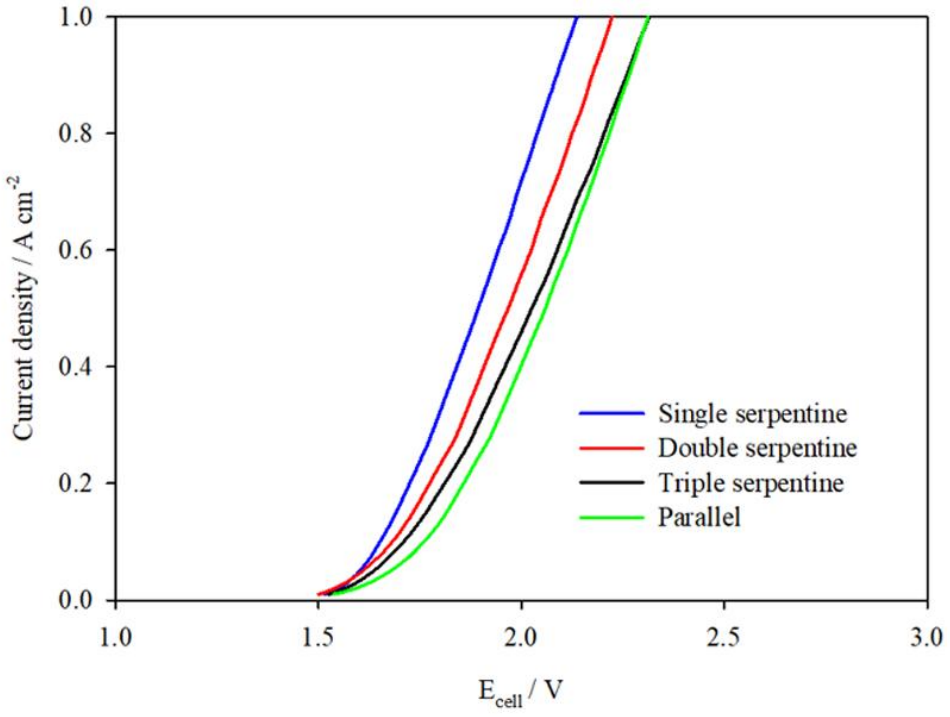

Figure 24. I-U curves of the cell assembled with various flow field channels. [84]

The flow channel designs can be ranked based on ascending cell voltages from best to worst performance: single serpentine > double serpentine > triple serpentine > parallel.

It should be noted that the reported cell performance does not directly correlate to the electrode area exposed to the electrolyte flow, which indicates that the performance is more reliant on flow channel design, and hence electrolyte flow distribution, across the electrode.

At low current densities, numerous small, spherical oxygen bubbles form on the surface of the liquid/gas diffusion layer (LGDL) and remain attached due to surface tension. As the current density increases, the water flow's dynamic pressure overcomes the adhesion forces, causing the bubbles to detach and enter the flow stream. Initially, the bubbles are dispersed throughout the water, representing a bubbly flow regime. With further increases in current density, the bubbles coalesce into elongated Taylor bubbles (also known as gas slugs) which dominate the channel. These slugs sweep through the channel, clearing smaller bubbles downstream. In designs with longer channel paths, such as the single serpentine flow-field, the flow transitions into an annular regime at high current densities. In this regime, gas slugs occupy the central core of the channel, pushing the liquid to the walls. This sequence of bubble formation, growth, detachment, coalescence, and sweeping is consistent across various flow-field designs and operating conditions.

As seen in Figure 24, the electrolyser assembled with parallel flow channels consistently reported the largest cell voltage at low and high current densities, demonstrating poorer cell performance. This can be explained by the flow of electrolyte across the electrode which is only in one direction, making it liable to nonuniform flow distribution and uneven distribution of temperature and pressure. In contrast, the electrolyser assembled with serpentine flow channels reports lower cell voltages, attributing to the continuous flow paths which provide better flow distribution over the same electrode area and thus ensures better management of hydrogen and oxygen bubble production and temperature distribution.

It is apparent that the cell performance decreases when the number of serpentine channels in the flow-field design increases, particularly at higher current densities where overpotential becomes more dependent on mass transfer. As the pump speed used was constant for the experiments, it is likely that the electrolyte mass flow rate through the channels decreases as the electrolyte flow is split across more channels.

The removal of bubbles in the single serpentine channel design is therefore more efficient and the effect on performance is especially significant at higher current densities where the rate of reaction, and hence bubble production rate, is faster. As the mass flow rate of electrolyte through the single serpentine flow channel is higher, reactant utilization and product removal are improved, which results in better cell performance.

Visualization of bubble evolution process in different flow channel designs is significant to better understand the effects of flow channel design on two-phase flow behavior in the channel, which subsequently determines the electrolyte flow distribution, H2 removal rate, and pressure drop of the electrolyser. For this purpose, the results of another article are provided for three different flow-field channels; the parallel, single serpentine and the less commonly used pin flow channels. [85]

The cross-sectional area of the channels is 1 × 1 mm^2, and the surface area of the channels are 25 × 25 mm^2. The configuration of the channels is with Z-type arrangement, where the KOH inlet is defined at the bottom left and the outlet is defined at the top right of the channel. There are 28 H_2 inlets at the back wall of the channel to simulate the H_2 bubbles coming from the straight-through pores of the GDL into the channel during the water electrolysis experiments. The illustration of these flow-fields is shown in Figure 25.

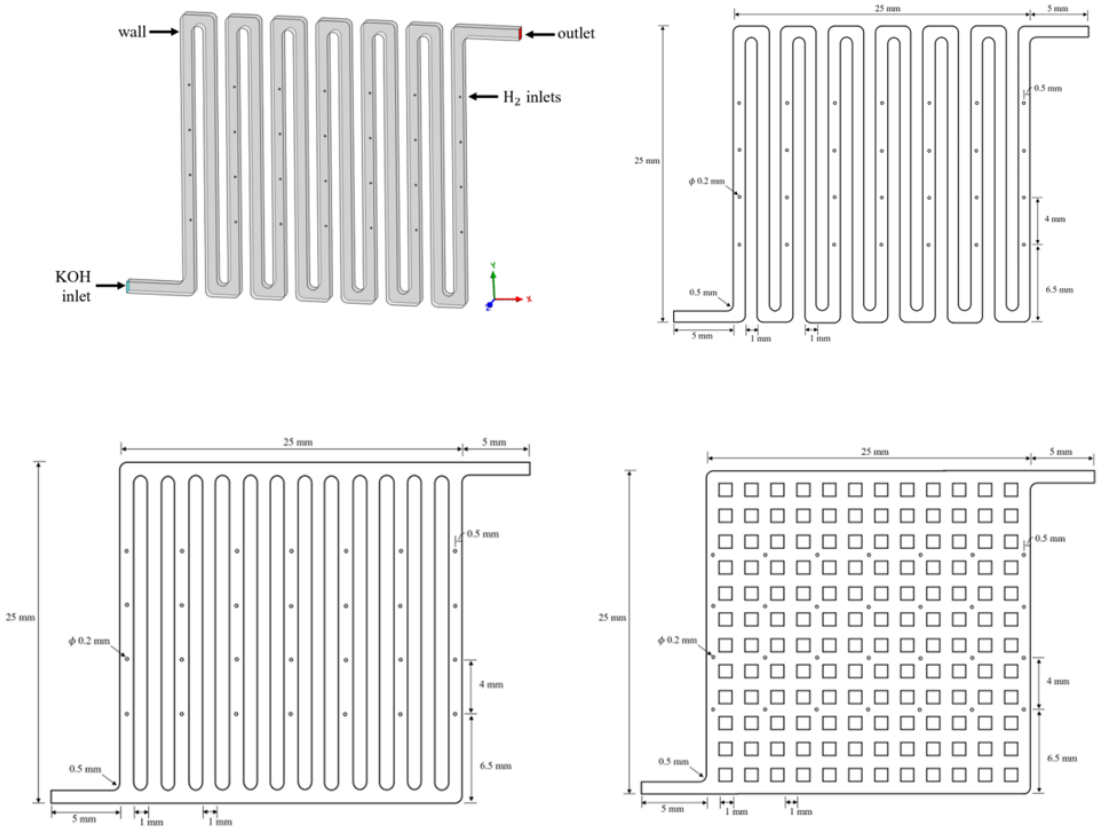

Figure 25. illustration of flow-fields; single serpentine on the top, parallel at the bottom left and the pin type at the bottom right. [85]

The bubble volume and the frequency (the number of bubbles inside channels) for the mentioned flow-fields after 160 ms of operation are reported in Figure 26.

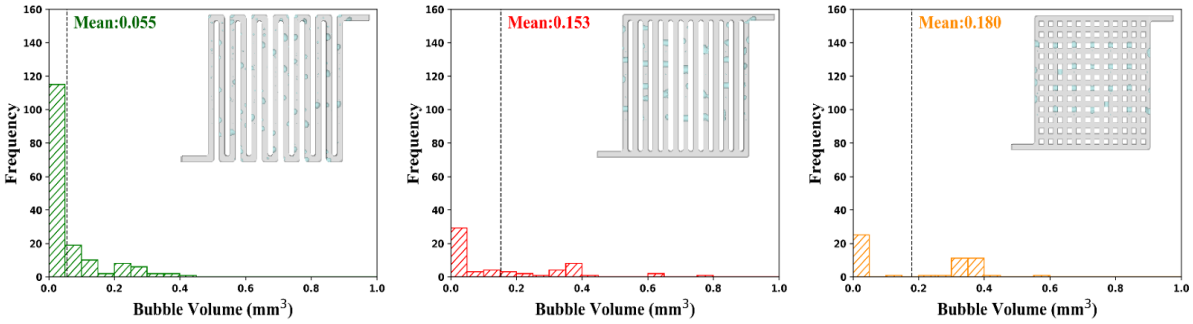

Figure 26. bubble volume and frequency for different flow-fields. [85]

The mean value in above picture is the average size of the bubbles. The size of the bubbles in single serpentine is relatively smaller and has a smaller number of slug than parallel and pin while the number of bubbles (frequency) in the single serpentine is the largest, whereas that in the pin is the smallest.

The pin flow channel has the largest mean bubble volume and so, bubble removal in parallel and pin are not as efficient as in single serpentine.

When the number of possible paths that fluid (electrolyte) can flow through increases, the flow velocity in the channel decreases. Different flow channel designs may also lead to different numbers of low velocity region (LVR) in the electrolyser. LVR is defined as the region with flow velocity less than or equal to 0.05 m/s, which is less than or equal to 10% of the inlet velocity. Analyzing the number and the location of LVR in different flow channel configuration is important to avoid bubble blockage and hence, to increase the efficiency of an electrolyser. The velocity distribution of different flow-fields is shown in Figure 27.

From the results, it is clear that for pin flow channel, almost the entire channel is considered as LVR, except the regions close to the inlet and outlet. As a result, the efficiency of the bubble removal from pin is quite low. The parallel channels flow-field has the lower LVR leading to its outperformance in bubble removal compared to other fields.

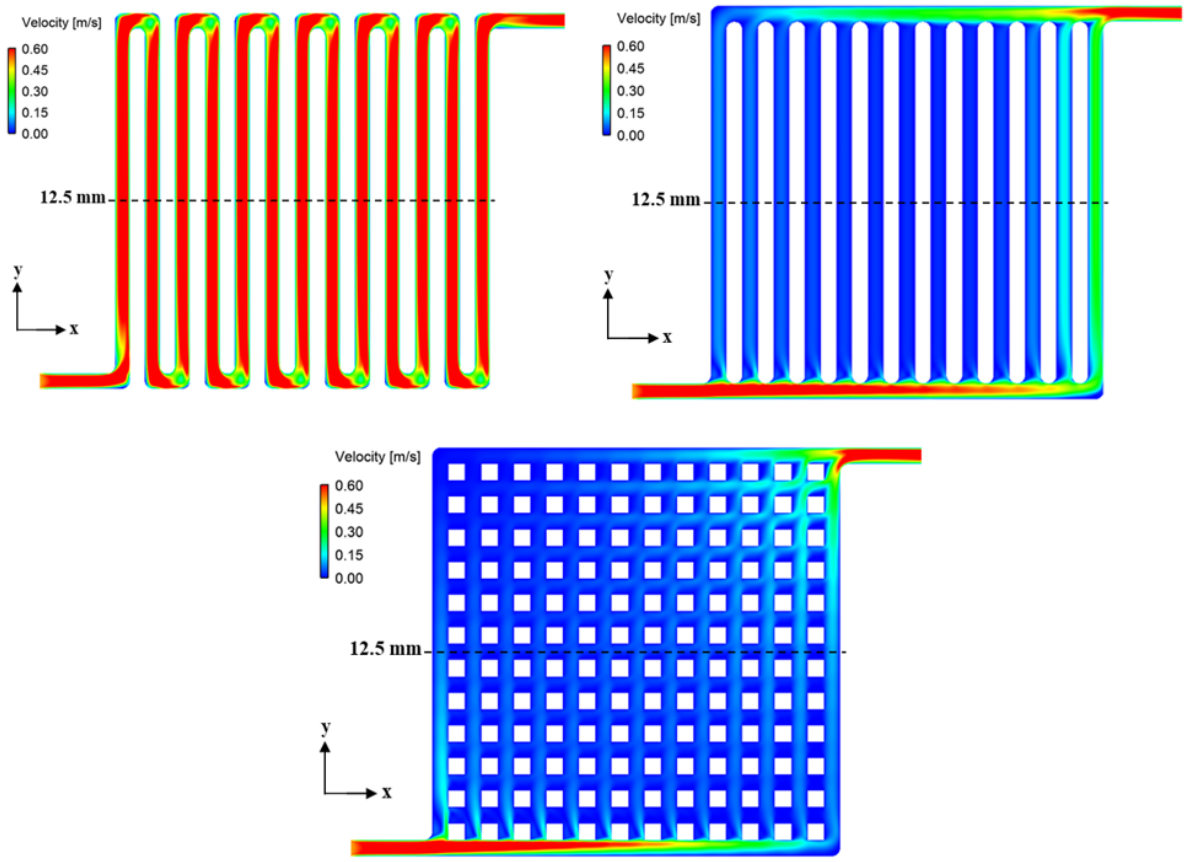

Figure 27. Velocity distribution for different flow-fields channels. [85]

3.3.3. Other layers

The membrane electrode assembly (MEA) is the weakest component in a typical AEM electrolyzer especially at high pressures. The thickness of the membrane has influence on the performance and on the working conditions of a AEM electrolyzer. Because thinner membrane leads to low ionic resistance, generally voltage efficiency is higher; on the other hand, diffusion can cause lower faradic efficiency in thinner membranes, especially at high pressures. Furthermore, safety-related issues must be taken into consideration. When high-pressure hydrogen production is taken into consideration, the thicker the membrane, the less diffusion of gases, hence the safer environment. [69]

Commonly, the MEA is supported with microporous metallic plates for high-pressure hydrogen production. The plates must be strong enough to withstand the high pressure. The

plates are used for multipurpose reasons besides using as supporting elements. It is also used as a gas diffusion layer; hence, it allows the reactants to reach the catalyst layer while the products are removed through the porous medium.

End plates are used to compress the stack with an appropriate pressure. Because we are dealing with high pressure in this thesis project, the end plates are chosen of thicker material compared with the fuel cells.

4 COMSOL Model Development

This chapter is devoted to modelling the high pressure AEM electrolyser single cell to see some results related to electrochemical and thermos-mechanical aspects of the cell. The electrochemical results could be used to assess the current density and applied voltage of the cell and hence the performance and efficiency of the cell. The thermo-mechanical results could be used to assess the temperature distribution across all components and mechanical stress and strain of different layers so they must be compatible with the material limitations and cell constraints.

The 3D geometry of the model was built in COMSOL Multiphysics version 6.2, a Multiphysics simulation and finite element analysis program.

General assumptions, computational domain, geometry, mesh, boundary conditions and numerical implementation are all components of the model, later in this chapter are deeply described into detail.

4.1. Geometry

For creating the geometry of the 3D model, some parameters are derived from previous sections and some from a commercial high pressure AEM electrolyser cell (NREL). All that must be defined for the geometry of membrane, anode and cathode electrodes and gas diffusion layers are the width, height and depth of these layers. The active area of the cell is 25 cm^2 with 5 cm in width and 5 cm in height for the membrane. The same dimensions are used for anode and cathode electrodes and gas diffusion layers. For the thickness of these layers, the data derived from chapter 2 are used which is provided in Table 23.

component	membrane	anode electrode	cathode electrode	anode GDL	cathode GDL
thickness [µm]	0.05	0.53	0.36	0.56	0.5

Table 23. thickness of internal layers of the high pressure AEMEL

The 3D geometry of components in above table is shown in Figure 28.

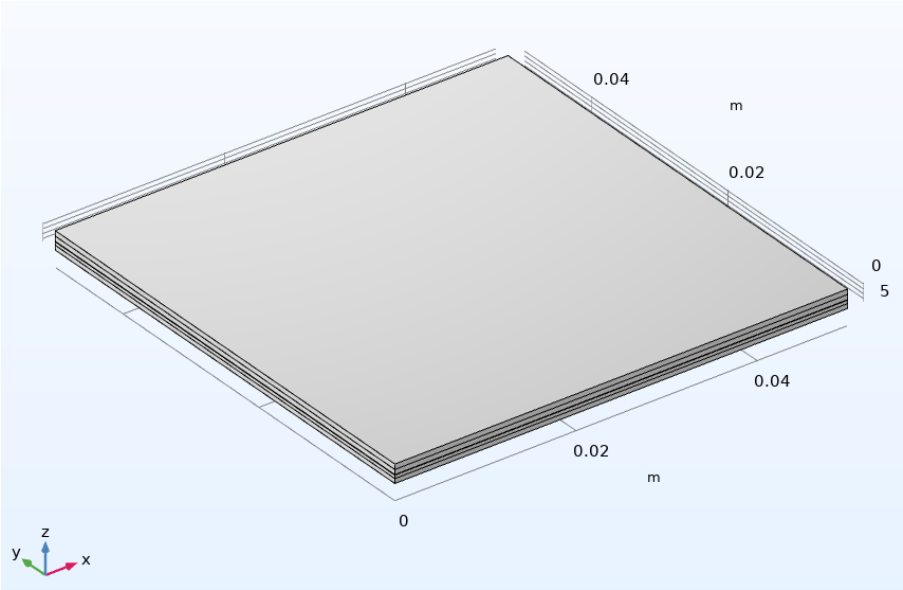

Figure 28. 3D geometry of internal components (membrane, electrodes and GDLs).

For creating the geometry of flow-fields, bipolar plates, gasket, current collector and end plate, due to the complexity and importance of all detailed geometrical aspects of these components, it was preferred to use commercial cases since their stability and performance have been validated before by experts. Since this kind of information are very rare to find and are considered classified for companies, the only commercial electrolyser company/institution providing all these components' geometrical details was NREL (National Renewable Energy Laboratory) in USA. [86]

The active area of this commercial electrolyser is 25 cm^2 and its operating pressure is 30 bar which are the same as the studied model in this thesis project and so the gasket, bipolar plates, current collector and end plate of the studied model are derived from this commercial electrolyser.

The flow-field configuration used in this device is triple serpentine which is shown in Figure 29.

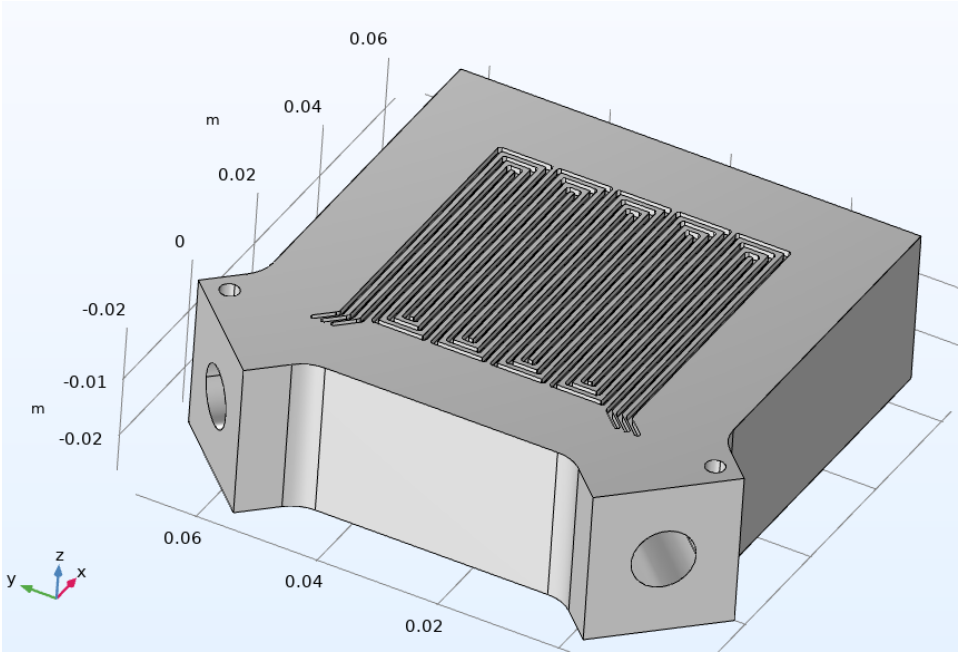

Figure 29. 3D geometry of the bipolar plate with the flow-fields.

The dimensions of the channels and bipolar plate are as follows; the channel depth is 1 mm, the channel width is 0.83 mm, and the rib length is 0.83 mm. the rib is defined as the area between two adjacent channels. So, the channel to rib ratio which is a common parameter for designing the channels would be 1:1 which is an acceptable value. The thickness of the bipolar plate is 25.4 mm. inlet and outlet of the fluids are also visible at two edges of the bipolar plate.

The gasket required for sealing the cell is shown in Figure 30. Its thickness is 0.25 mm and so considering the length of internal components (membrane, anode and cathode electrodes and gas diffusion layers) which is 2 mm, the required number of gaskets to seal this length would be 8 which are put together. It is also worth noting that the internal void surface of the gasket is exactly equal to 25 cm^2 and so internal components would be in contact with the gaskets. The two cylindrical holes inside the gasket are just for alignment purpose with the bipolar plates.

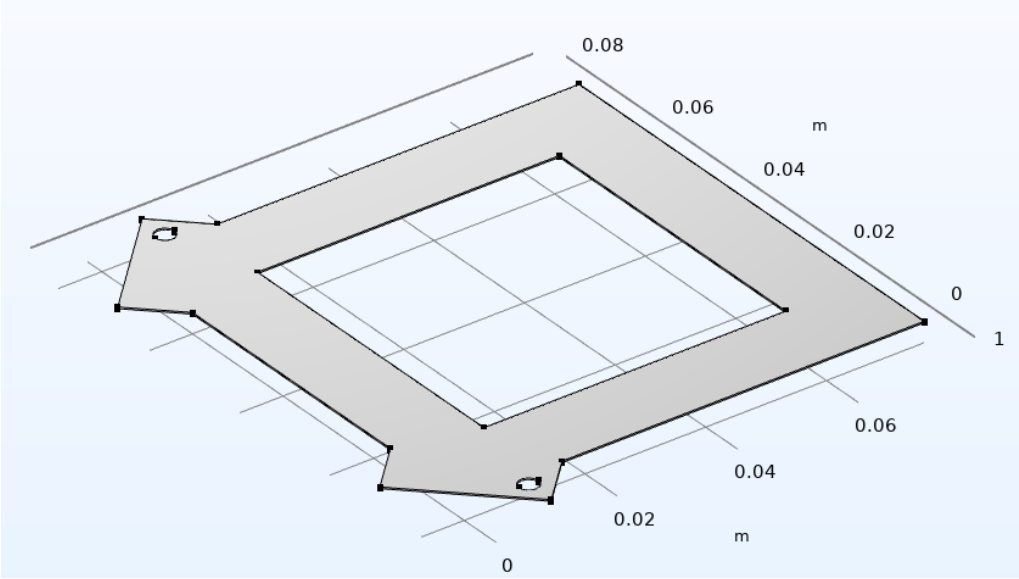

Figure 30. 3D geometry of the gasket.

The final 3D geometry of the single cell containing all components is shown in Figure 31.

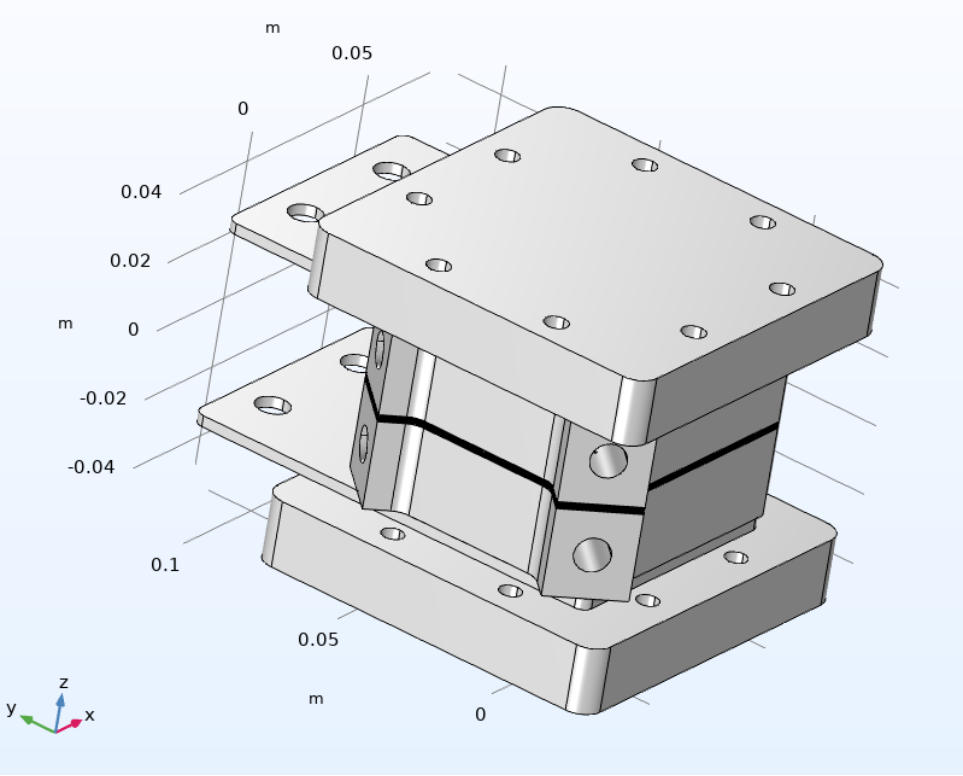

Figure 31. 3D geometry of the single cell.

The bipolar plate used for anode and cathode sides is the same. The covering surface of the triple serpentine channels is 25 cm^2 and is adjusted to be in contact with the gas diffusion layers. Current collectors are considered at both anode and cathode side with holes suitable for connecting the cables. The thickness of the current collector is 3.17 mm. the direction of the current collectors is selected based on the real commercial device.

Finally, the end plates are considered at both anode and cathode side with 8 holes provided for installing the bolts and applying the clamping torque. The thickness of the endplate is 19 mm.

To better visualize the internal parts of the components specially the bipolar plate and channels, a close shot image with transparency is provided in Figure 32.

It is visible that there is a connecting section between the inlet and outlet of the bipolar plate and the triple serpentine flow-field. The purple components are the 8 gaskets which are perfectly aligned between the two bipolar plates and preventing the fluids from leakage and mixing with each other.

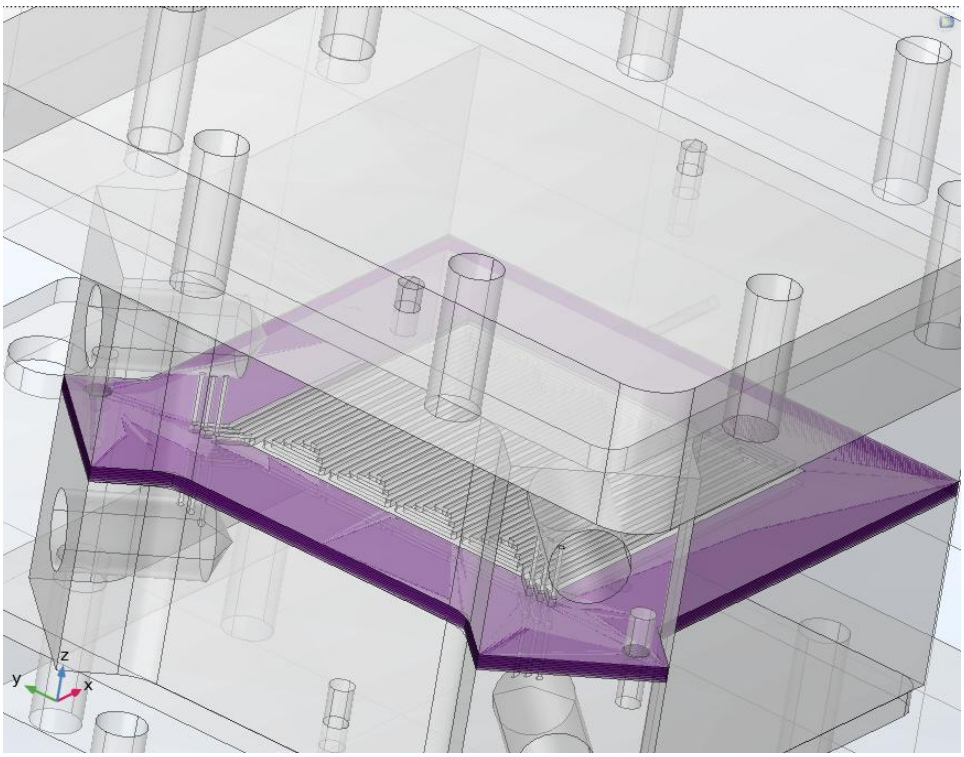

Figure 32. 3D geometry of the model with transparency.

4.2. Mesh

COMSOL uses the finite element method (FEM) which the continuous geometry is divided into small elements called mesh and the equations of desired physics are solved locally for each element. The global solution would be the assembly of all elements' calculations.

There are two options for the sequence type in COMSOL software; the "physics-controlled mesh" and the "user-controlled mesh". In the first one, COMSOL automatically generates the mesh based on selected physics interfaces, geometry size and features with good accuracy. In this case, only the element size is selected by the user from the list of extremely fine to extremely coarse. The highest resolution is achieved if extremely fine is selected but the computational time is very high. The fastest solution is achieved by selecting the extremely coarse, but the results are not very accurate in this case. This method has been chosen for the current study with Normal mesh size which is a good compromise between accuracy and computational time. The 3D mesh of the single cell is shown in Figure 33.

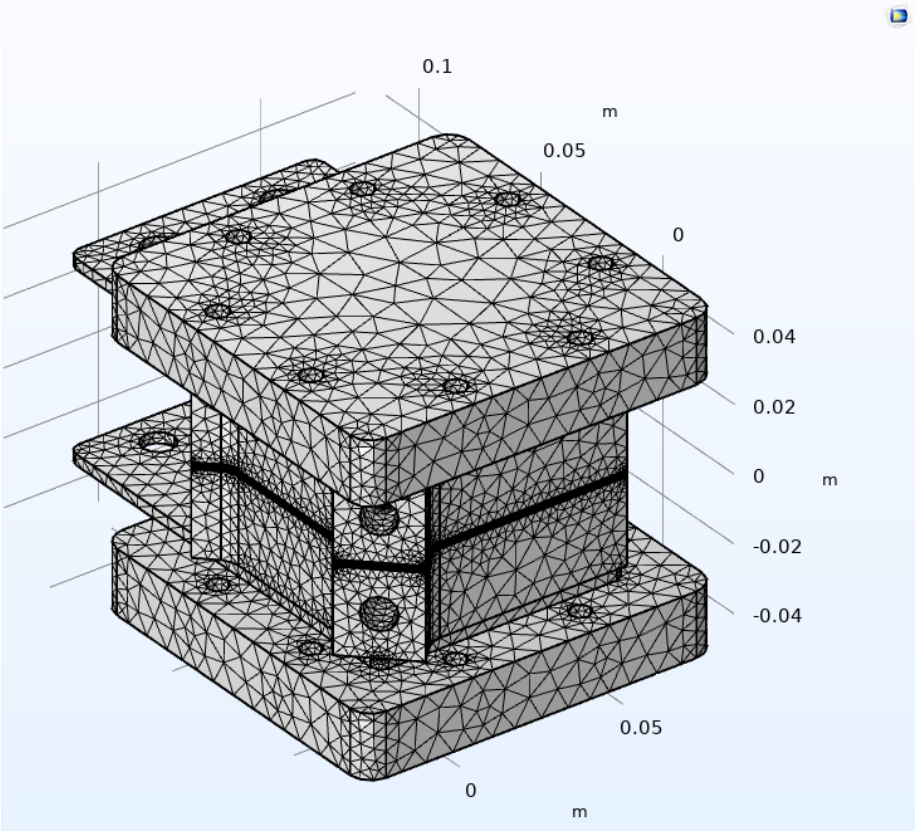

Figure 33. 3D mesh of the single cell.

If the “the user-controlled mesh” was selected, the user must explicitly define the element size, the mesh type and other required parameters and can cause errors if they are poorly defined.

From Figure 33, it is visible that close to edges, holes and across thin layers like gaskets, the number of elements increase to have enough accuracy through all the geometry. To better visualize this aspect, the current collector and end plate of the anode side are removed, and the top view of the cell is shown in Figure 34. It is clear that the number of the elements are much higher across the gaskets and flow channels compared to current collector and end plate since they could be more sensitive to mechanical force due to their thinner dimensions and the electrochemical reactions occur across the channels.

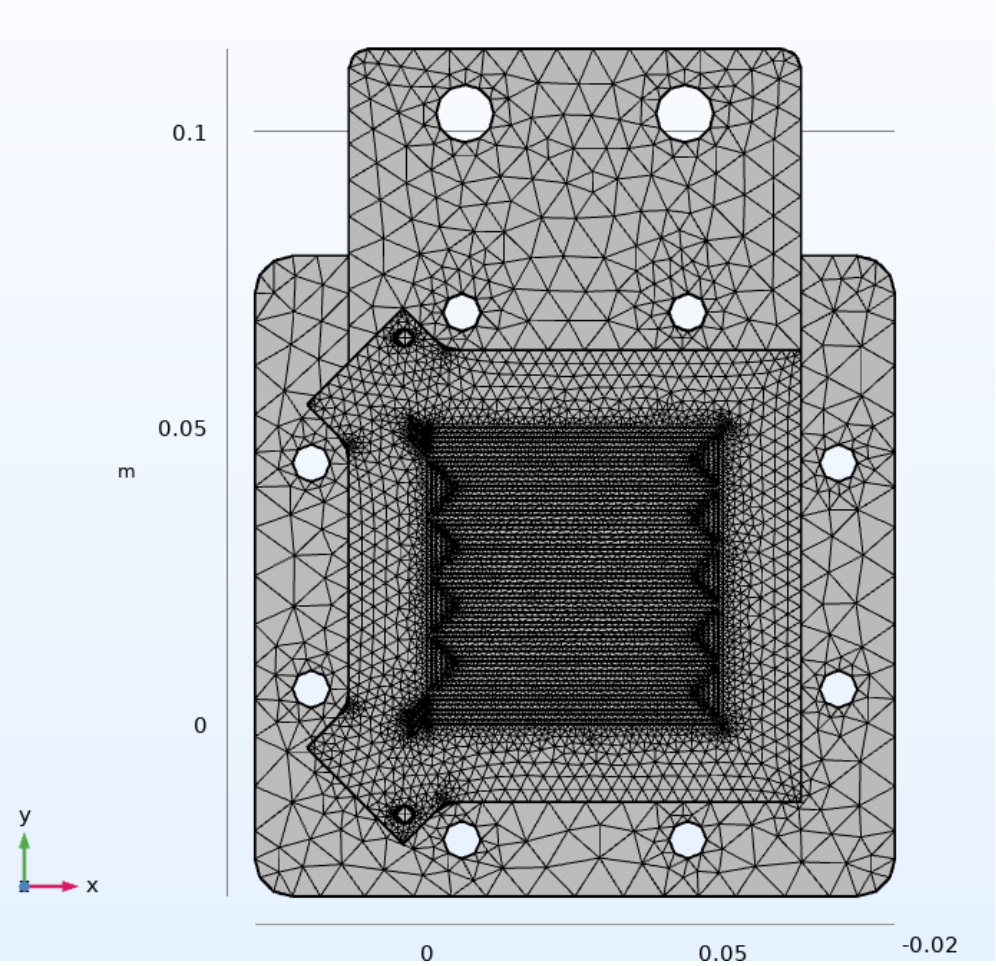

Figure 34. top view of the 3D mesh geometry.

4.3. Materials

The material for each of the domains must be defined with the necessary properties that are related to the selected physics. So, it is better to select the physics first and then defining the materials. In this case, if any material property which is necessary for calculation is missed, the COMSOL would warn about it.

There are two options for defining the materials; the first and common way is “add material from library” and the second one is “blank material”. So many different materials with their properties are defined in COMSOL material library that could be selected easily. The second approach is manually defining all the necessary properties of the material. The material for membrane and was defined manually by selecting blank material and for other domains (components), the materials in the COMSOL library were selected that will be discussed in the following.

As seen in chapter 2, different materials could be used for different layers of the AEM electrolyser. In this study, the materials were mainly selected based on having a balance between cost and performance.

Starting from the membrane, the PurionX-131 was selected. The properties of this membrane material are provided in Table 24. Where manufacturer data were unavailable, typical values for hydrated polymer AEMs were adopted from literature for the properties of PurionX-131. [87]

Property	Variable	Value	Unit	Property group
Thermal conductivity	k_iso ; kii = k_...	0.1	W/(m·K)	Basic
Density	rho	800	kg/m³	Basic
Heat capacity at constant pressure	Cp	3000	J/(kg·K)	Basic
Coefficient of thermal expansion	alpha_iso ; al...	1e-4	1/K	Basic
Young's modulus	E	2E9	Pa	Young's modulus and Poisson's ratio
Poisson's ratio	nu	0.4	1	Young's modulus and Poisson's ratio
Electrolyte conductivity	sigmal_iso ; s...	5	S/m	Electrolyte conductivity

Table 24. material properties of the membrane. [88]

For the gaskets, the PTFE was chosen from the COMSOL material library as it is the most common gasket material used in electrolysers. The properties of the PTFE gasket are provided in Table 25.

Property	Variable	Value	Unit	Property group
Coefficient of thermal expansion	alpha_iso ; al...	100e-6[1/K]	1/K	Basic
Heat capacity at constant pressure	Cp	1050[J/(kg*K)]	J/(kg·K)	Basic
Density	rho	2200[kg/m^3]	kg/m³	Basic
Thermal conductivity	k_iso ; kii = k_...	0.24[W/(m*K)]	W/(m·K)	Basic
Young's modulus	E	0.4e9[Pa]	Pa	Young's modulus and Poisson's ratio
Poisson's ratio	nu	0.46	1	Young's modulus and Poisson's ratio
Relative permittivity	epsilonr_iso ;...	2	1	Basic

Table 25. material properties of the PTFE gasket.

The material for both anode and cathode electrodes and gas diffusion layers were chosen to be Nickel from the library of the COMSOL. Since there are many different materials under Nickel material in the COMSOL library, the one that is close to common materials in porous electrodes and GDLs is “Nickel [solid, annealed]”. As can be seen in Table 26, the material properties of the Nickel are defined by COMSOL itself.

Property	Variable	Value	Unit	Property group
Hardening function	sigmagh		Pa	Elastoplastic material model
Coefficient of thermal expansion	alpha_iso ; al...	(alpha_solid_1(T...	1/K	Basic
Electrical conductivity	sigma_iso ; si...	sigma_solid_an...	S/m	Basic
Density	rho	rho_solid_1(T)	kg/m³	Basic
Young's modulus	E	E(T)	Pa	Young's modulus and Poisson's ratio
Poisson's ratio	nu	nu(T)	1	Young's modulus and Poisson's ratio
Electrolyte conductivity	sigmal_iso ; s...	3	S/m	Electrolyte conductivity
Thermal conductivity	k_iso ; kii = k...	k_solid_anneale...	W/(m·K)	Basic
Resistivity	res_iso ; resii...	res_solid_anneal...	Ω·m	Basic
Heat capacity at constant pressure	Cp	C_solid_1(T)	J/(kg·K)	Basic
Surface emissivity	epsilon_rad	epsilon(T)	1	Basic
Tangent coefficient of thermal expansion	alphatan_iso...	CTE(T)	1/K	Thermal expansion
Thermal strain	dL_iso ; dLii...	(dL_solid_1(T)-d...	1	Thermal expansion
Bulk modulus	K	kappa(T)	N/m²	Bulk modulus and shear modulus
Shear modulus	G	mu(T)	N/m²	Bulk modulus and shear modulus

Table 26. material properties of the Nickel electrodes and GDLs.

finally, for the bipolar plate, current collector and end plate, the duplex stainless steel has been chosen from the COMSOL library with the title “UNS S32205 (duplex stainless steel) in 40 g/L H2SO4 and 1 g/L HCl at 90 C”. the material properties of this material are defined by COMSOL itself as we’ve already seen for the Nickel and are provided in Table 27.

	Property	Variable	Value	Unit	Property group
☑	Density	rho	7695	kg/m³	Basic
☑	Electrical conductivity	sigma_iso ; si...	1.3E6	S/m	Basic
☑	Thermal conductivity	k_iso ; kii = k_...	15	W/(m·K)	Basic
☑	Heat capacity at constant pressure	Cp	500	J/(kg·K)	Basic
☑	Coefficient of thermal expansion	alpha_iso ; al...	13e-6	1/K	Basic
☑	Young's modulus	E	200E9	Pa	Young's modulus and Poisson's ratio
☑	Poisson's ratio	nu	0.3	1	Young's modulus and Poisson's ratio
	Local current density expression	ilocmat	iloc_exp(E_vs_ref...	A/m²	Local current density
	Equilibrium potential	Eeq	Eeq_vs_SHE	V	Equilibrium potential
	Temperature derivative of equilibrium potential	dEeqdT	0[V/K]	V/K	Equilibrium potential
	Reference concentration	cEeqref	0[mol/m^3]	mol/m³	Equilibrium potential

Table 27. material properties of the bipolar plate, current collector and end plate.

4.4. Physics

The main goal of the thesis project is to have the thermo-mechanical simulation of the high pressure AEM electrolyser. To achieve this goal, three physics must be studied in COMSOL as follow: Heat Transfer in Solids (ht), Solid Mechanics (solid) and Secondary Current Distribution (cd). By selecting these physics, two other Multiphysics would be shown in COMSOL called “Electrochemical Heating” and “Thermal Expansion” that would be assessed in the following sections.

4.4.1. Heat transfer in solids

To obtain the temperature distribution across all components, this physic was selected as it solves the energy equation formulas which are related to the heat transfer in solid materials. As there is no simulation of fluids through channels and other layers, the selection of this physics was an appropriate selection since only the heat conduction through components, the heat convection of the cell with ambient and the heat sources related to electrochemical reactions were supposed to be analysed.

The energy transfer equation in porous computational domains (both anodic and cathodic catalyst layers and gas diffusion layers) can be defined as [89]:

$$\nabla \cdot \left(\rho_{\text{eff}} C_{p,\text{eff}} \mathbf{u} T\right) = \nabla \cdot \left(k_{\text{eff}} \nabla T\right) + S_T$$

Where ρ_{eff}, $C_{p,eff}$, and k_{eff} are the effective density, effective heat capacity and effective thermal conductivity, respectively, which can be calculated as:

$$\rho_{\text{eff}} = (1-\varepsilon)\rho_s + \varepsilon\rho_f$$

$$C_{p,\text{eff}} = (1-\varepsilon)C_{p,s} + \varepsilon C_{p,f}$$

$$k_{\text{eff}} = (1-\varepsilon)k_s + \varepsilon k_f$$

Here, ρ_s, $C_{p,s}$, and k_s are the density, heat capacity, and thermal conductivity of the solid phase, respectively that were defined based on the material properties from the previous section. ρ_f, $C_{p,f}$ and k_f denote the density, heat capacity and thermal conductivity of the fluid phase (1M KOH solution), respectively. The ε is the porosity of the catalyst layer and gas diffusion layer materials which are equal to 0.5 for both anodic and cathodic GDLs and 0.25 for both anodic and cathodic catalyst layers. [89]

for other remaining nonporous domains, the simple form of energy transfer equation has been used. So, in COMSOL, separate “Solid” nodes were selected to define the material properties of porous and nonporous domains separately.

In the energy transfer equation, S_T represents the source term of the energy equation, which includes the entropy heat and irreversible heat generated by the electrochemical reaction in the CLs, as well as the ohmic heat generated during the charge transfer process. These heat sources related to electrochemical reactions are included in the “electrochemical heating” Multiphysics and there is no need to take them into consideration under the current Heat Transfer physic.

For the convection heat transfer of fluids in anode and cathode channels and the convection of the whole cell with its surrounding ambient, three “heat flux” nodes were selected. The heat transfer coefficient for hydrogen through cathode flow-field channels and 1M KOH solution through anode flow-field channels were defined as 1400 W/m^2K and 3500 W/m^2K respectively. [90], [91]. For the convection of the whole solid cell with the ambient, the heat transfer coefficient was set to 20 W/m^2K [92].

Other required data for this physic are as follow; the reference and the initial temperature were defined as 293.15 K which is the ambient temperature.

In Figure 35 and Figure 36, the domains selected for the convection heat transfer of fluids in anode and cathode channels are shown respectively.

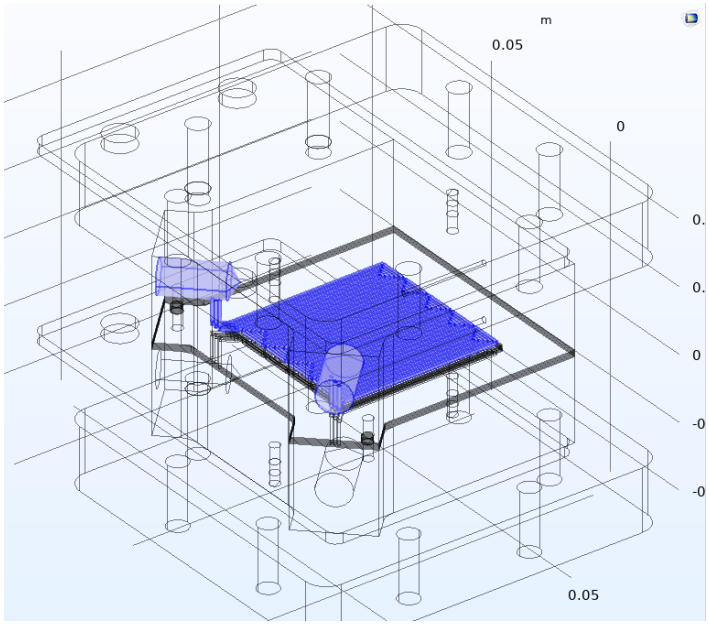

Figure 35. anode channels domain for convection heat transfer.

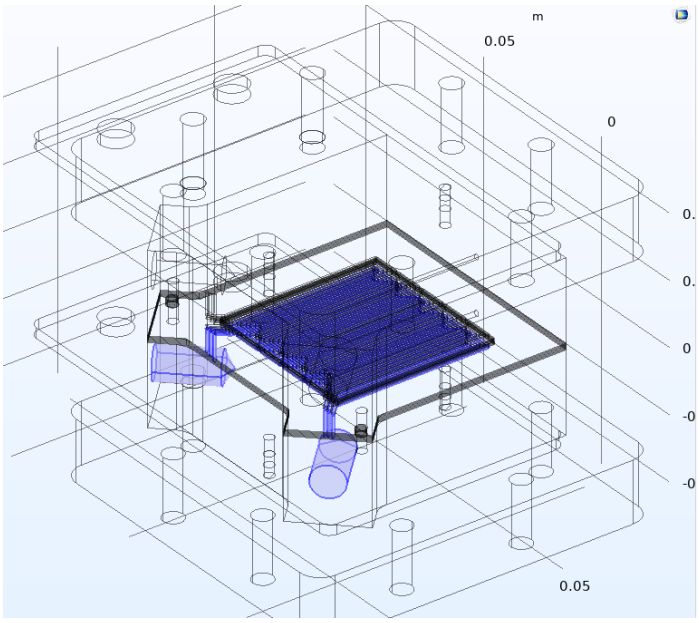

Figure 36. cathode channels domain for convection heat transfer

4.4.2. Solid mechanics

To obtain the pressure distribution and mechanical strain across all components, this physic was selected as it solves linear and nonlinear elasticity equations. All the components have elastic behaviour except the membrane. So, the “linear elastic material” node has been selected to define all the elastic components behaviour under clamping force and the “hyperelastic material” has been selected to define the membrane.

The required applying force was calculated based on the formulas in chapter 3 and it became equal to 21 KN which is applied as a “boundary load” on the upper surface of the anode endplate which is at the top of the cell. To fix the cell from any movement and so behaving like a rigid body, a “fixed constraint” was applied on the lower surface of the cathode endplate which is at the bottom of the cell. The “rigid connector” node was selected and three points on the same surface where the “fixed constraint” is applied are defined to prevent the cell from rotation around x-y-z axes. [93]

For linear elastic materials, the “material symmetry” was selected as Isotropic and the required material properties like the young’s modulus and the poisson’s ratio are derived from the “material” section. Regarding the hyperelastic membrane, the “material model” was selected as Neo-Hookean and the Simo-Pister was selected for the “volumetric strain energy”.

In figure 37, the surface of the applied boundary load is shown.

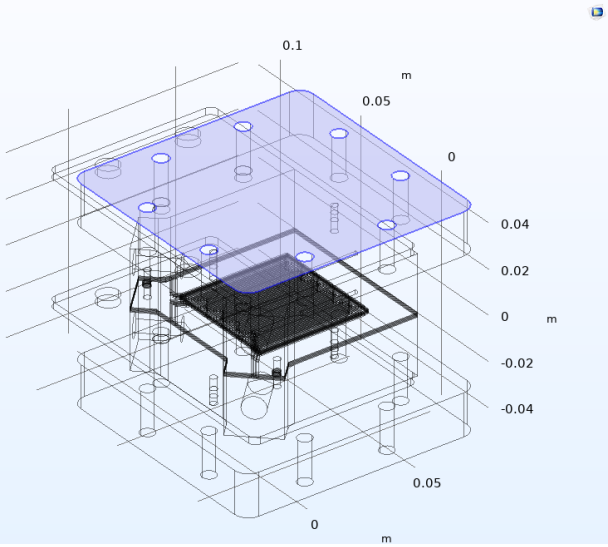

Figure 37. surface of the applied boundary load.

In Figure 38and Figure 39, the constraints applied on the bottom surface of the cathode endplate are shown.

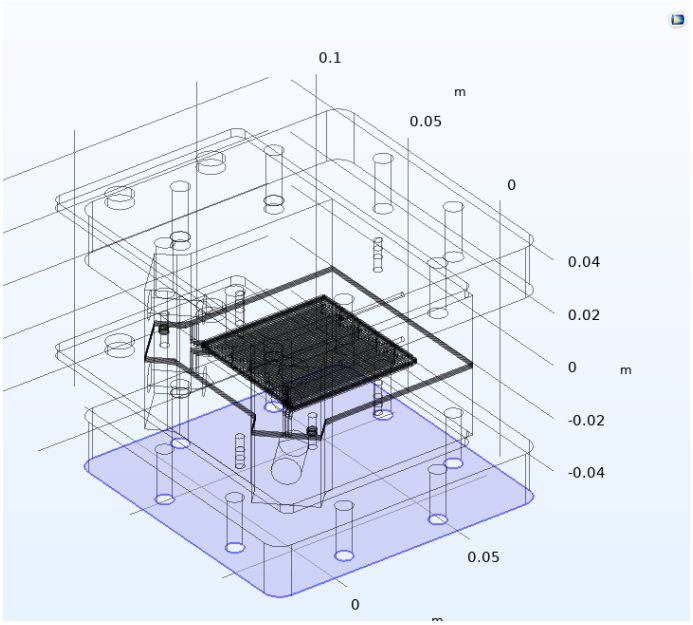

Figure 38. the fixed constraint surface.

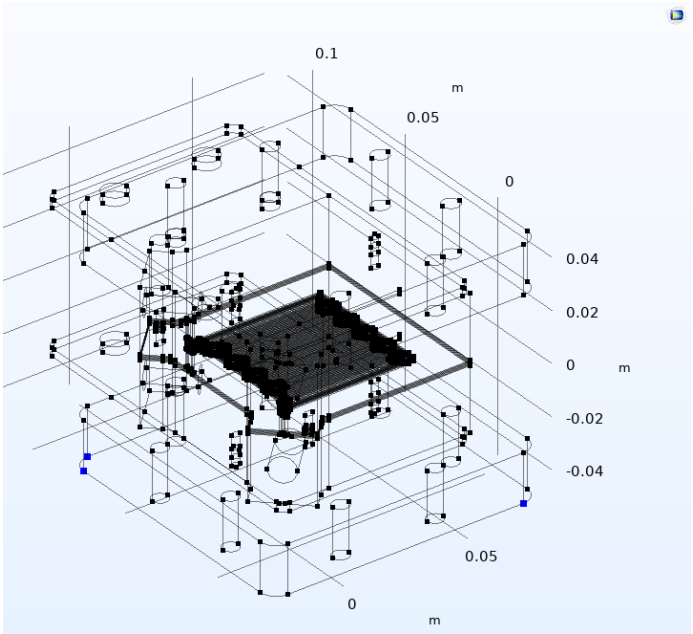

Figure 39. three points as rigid connectors.

4.4.3. Secondary current distribution

To obtain the current distribution and electric potential across electrochemical reaction zones, this physic was selected. What matters more in this section is obtaining the I-U curve of the cell from the results of this physic which represent the performance of the cell and could be compared with the I-U curves of other models.

On the anode, the electro-oxidation of hydroxide ions is a complicated multi-step electrochemical process, and its reaction mechanism is yet to be completely understood. For the sake of simplicity, the Butler-Volmer equation is used for the OER as follow [94]:

$$j_a = i_{0,a}\left\{\exp\left(\frac{\alpha_a nF}{RT}\eta_a\right) - \exp\left(\frac{-(1-\alpha_a)nF}{RT}\eta_a\right)\right\}$$

Where $i_{0,a}$ is the anode exchange current density and η_a is the anode overpotential. With respect to the electro-reduction of water on the cathode, the Butler-Volmer equation is employed for the HER:

$$j_c = si_{0,c}\left\{\exp\left(\frac{\alpha_c nF}{RT}\eta_c\right) - \exp\left(\frac{-(1-\alpha_c)nF}{RT}\eta_c\right)\right\}$$

Where $i_{0,c}$ is the cathode exchange current density and η_c is the cathode overpotential.

With the anode and cathode overpotentials obtained from the equations presented above, the total voltage loss and the applied voltage can be assessed:

$$V_{loss} = \eta_a + \eta_c + i_{cell}\left(R_{contact} + \frac{l_M}{\sigma_M}\right)$$

$$V_{applied} = E + \eta_a + \eta_c + i_{cell}\left(R_{contact} + \frac{l_M}{\sigma_M}\right)$$

Where E is the Nernst potential of an AEM water electrolyzer, which is given by:

$$E = E^0 - 0.9 \times 10^{-3}(T - 298) + \frac{RT}{nF}\ln\left(\frac{P_{H_2}P_{O_2}^{1/2}}{P_{H_2O}}\right)$$

And the system resistance is composed of the contact resistance ($R_{contact}$) and the membrane resistance (l_M/σ_M).

The nodes that were defined for this physic are as follows; the “electrolyte” for defining the membrane, two “porous electrode” nodes for defining the anode and cathode electrodes and catalyst layers, the “current conductor” node for defining other metallic layers like both anodic and cathodic GDLs, bipolar plates and current collectors that are not involved in the electrochemical reactions but just conduct and transfer electrons. The “electric potential” node for defining the anode current collector as the component where the applied voltage of the cell would be implied on it. The “electric ground” node for defining the cathode current collector as the component which is assumed that is connected to the ground and so its voltage is equal to zero.

The required parameters that must be defined for the nodes of this physic are as follows; the “effective conductivity correction” was selected as Bruggeman for both electrolyte and electrode current conduction in anode and cathode. Both electrolyte and electrode volume fractions were inserted equal to 0.5 and the reference equilibrium potential for the OER was 1.188 [V] and for the HER was zero. The exchange current density for anode and cathode was selected as 0.37 [A/m^2] and 0.43 [A/m^2] respectively. Anodic and cathodic transfer coefficients were both defined as 0.5 and the active specific surface area for both anode and cathode electrodes was inserted 10^6 [1/m]. Finally, the applied voltage on the cell that must be defined as boundary electric potential was set to 1.5 [V]. [94], [95]

4.4.4. Multiphysics

By selecting the three mentioned physics, COMSOL itself would suggest some Multiphysics nodes that could be studied which is taking the effects of two physics and their equations simultaneously to get some solutions that could not be achieved by solving the physics separately. In the following sub-sections, two Multiphysics would be described which are electrochemical heating and the thermal expansion.

4.4.4.1. Electrochemical heating

Electrochemical heating Multiphysics takes into account the heat transfer in solids physic and the secondary current distribution physic together to obtain the heat transfer and temperature distribution across the reaction zones due to heat sources related to electrochemical reactions. The secondary current distribution solely provides the distribution of current density and the electric potential and the heat transfer in solids solely

provides the temperature distribution due to convection and conduction and none of them contains the heat sources related to electrochemical reactions.

The electrochemical heat sources are as follows; for a porous electrode, joule heating (Q_{JH}) and electrochemical sources (Reversible (entropy) heat and Irreversible reaction heat (activation losses)) (Q_m) are summed up for a total heat source (Q_h) in the domain according to [96] :

$$Q_h = Q_{JH} + \sum_m a_{v,m} Q_m$$

$$Q_{JH} = -\left(\mathbf{i}_s \cdot \nabla \phi_s + \mathbf{i}_l \cdot \nabla \phi_l\right)$$

$$Q_m = \left(\phi_s - \phi_l - E_{eq,m} + T\frac{\partial E_{eq,m}}{\partial T}\right) i_{loc,m}$$

The heat is produced via above mentioned electrochemical phenomena and is conducted through the layers and some part of it would be absorbed by fluids passing through the anode and cathode channels and part of would be transferred via convection to the ambient. The output of this Multiphysics would be the real temperature distribution and electrochemical characteristics across the components and would be taken as reference for validation.

4.4.4.2. Thermal expansion

The thermal expansion Multyphysics takes into account the heat transfer in solids physic and the solid mechanics physic together to obtain the more accurate pressure distribution and mainly the deformation of components due to considering the thermal stress applied on all components since the operating temperature is higher than atmospheric temperature and some extra stress would be implied on components because of the temperature difference.

The solid mechanics physic solely solve the pressure distribution across components at reference temperature which is not the operating temperature and so the stress and strain distribution plots obtained from this physic show lower values compared to values obtained from the thermal expansion Multiphysics which are more realistic and would be used as reference for validation of pressure and strain distribution across components.

5 Results

The purpose of this thesis project was to have the thermo-mechanical modelling of the high pressure AEM electrolyser. To achieve this goal three different physics were used in COMSOL software to obtain the temperature and pressure distribution across all components. Besides, the most important characteristic of the electrolyser which is the I-U curve was also derived from the results to have a reference for comparing the current high-pressure model with other models in literature in terms of performance.

In the following sections, the three above mentioned characteristics would be described in detail and finally they would be validated by comparing them with most similar models found in the literature.

5.1. Polarization curve

The polarization curve shows the produced current density of the cell by applying a specific voltage to the cell. The higher current density produced by the cell for a specific applied voltage, the better performance of the cell would be.

The polarization curve (I-U curve) of the model was derived by doing a parametric sweep study in COMSOL for the applied voltage of the cell. By this study, the common range of applied voltage of the cell was determined which is from 1.5 [V] to 2.2 [V] with an increasing step of 0.1 [V], and COMSOL solved the electrochemical heating Multiphysics for this range of voltage values. The outcome was a set of current values for each specific applied voltage. Since the current density is needed for the polarization curve which is current passing through the unit of the active area, the obtained total current values were divided by the surface area of the active area which is 25 cm^2 to get the current density values for each specific applied voltage. Finally, the curve was plotted using EXCELMS software which is shown in Figure 40.

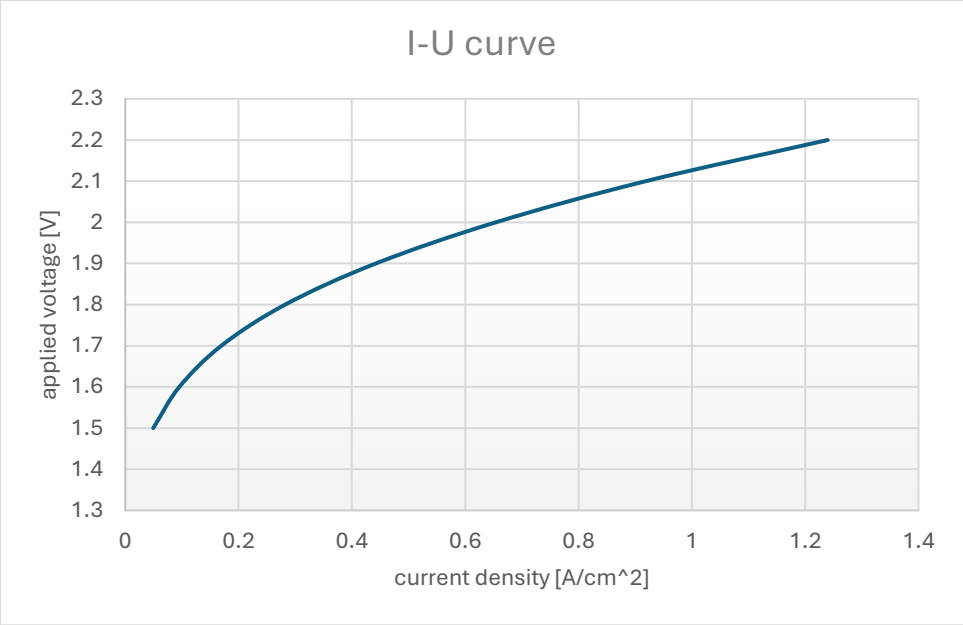

Figure 40. Polarization curve of the model.

Increasing the applied voltage of the cell leads to increasing the produced current density which in other terms means higher production of hydrogen. Since higher production of hydrogen is usually the purpose of operating electrolysers, higher values of applied voltages could be used but at the other hand it leads to higher power consumption which is not desirable. A good balance between these two parameters is choosing the applied voltage equal to 2 [V] which in our case, leads to 0.65 [A/cm^2] of produced current density.

5.2. Temperature distribution

The temperature distribution is obtained by computing the electrochemical heating Multiphysics as it contains both heat sources related to electrochemical reactions and heat transfer phenomena. The temperature distribution is assessed to make sure that all components of the cell are operating under safe conditions specially the membrane and gaskets which are the polymeric components of the cell and are more sensitive to high temperatures and must be protected from the degradation. Besides, vaporized water must be avoided through the layers, and this limits the operating temperature across the layers containing water.

The temperature distribution across the whole cell is shown in Figure 41.

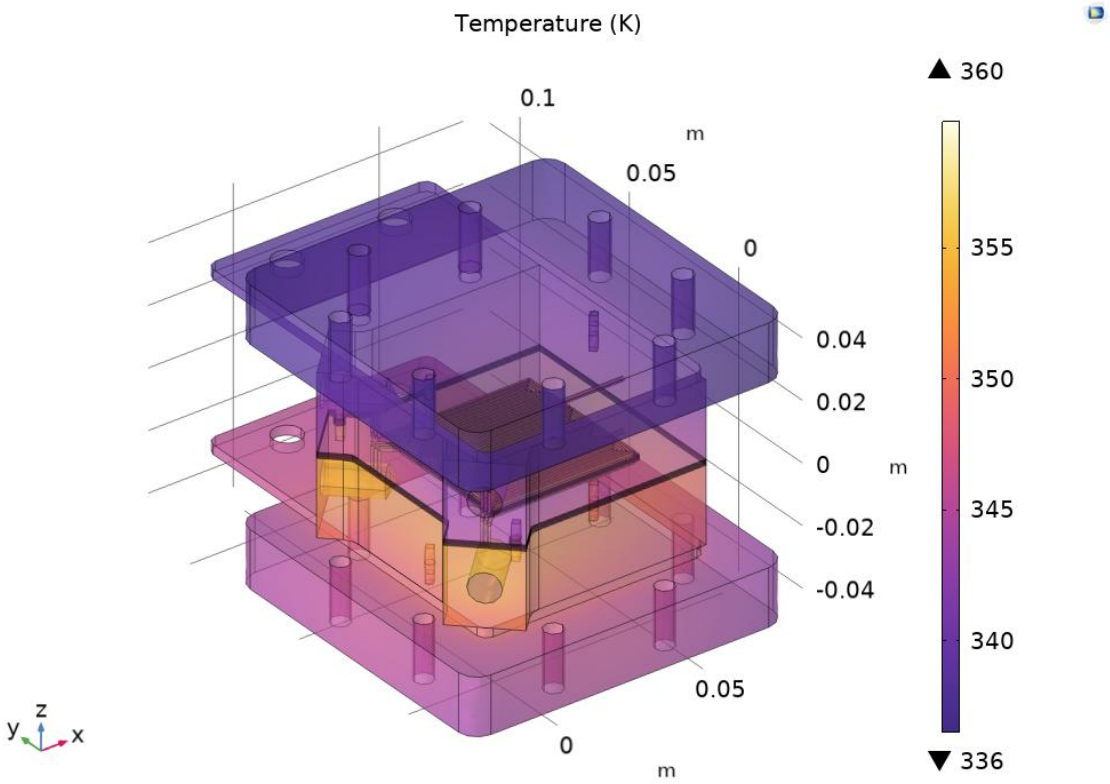

Figure 41. Temperature distribution across the cell.

The hottest points of cell are across the membrane where the electrochemical reactions occur and produce heat. Moving to outer layers of cell, the temperature decreases due to convection of heat with ambient and absorbing heat by the fluids passing through the anode and cathode channels. The temperature at the membrane surface is 360 K and due to selecting same materials for both anode and cathode sides, the temperature distribution across anode and cathode components are almost the same. The significant difference is between anode and cathode bipolar plates where the anode bipolar plate has lower temperature compared to cathode bipolar plate. The temperature distribution of components from the side view is also shown in Figure 42.

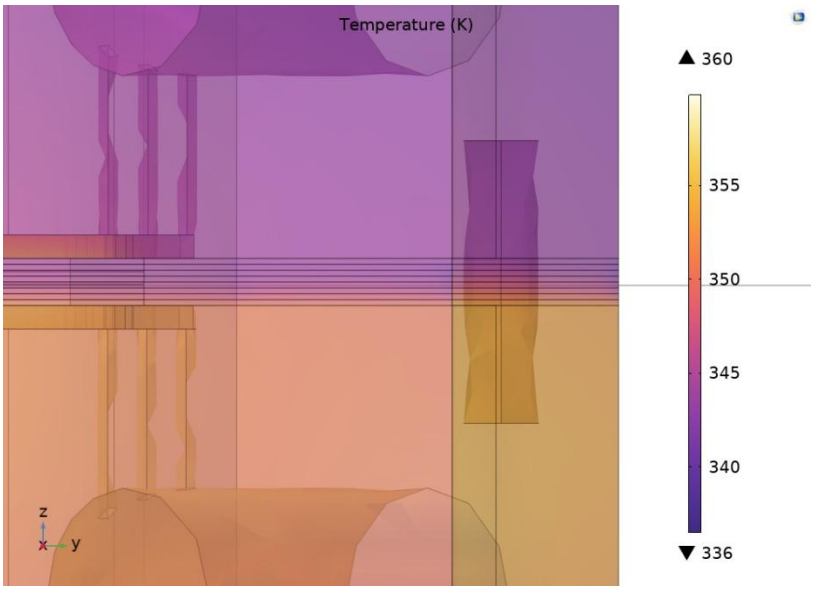

Figure 42. Temperature distribution of the cell from side view.

As mentioned before, two components which are more sensitive to high temperature are membrane and gasket which are shown in Figure 43 and Figure 44 respectively, the temperature distribution of these two components.

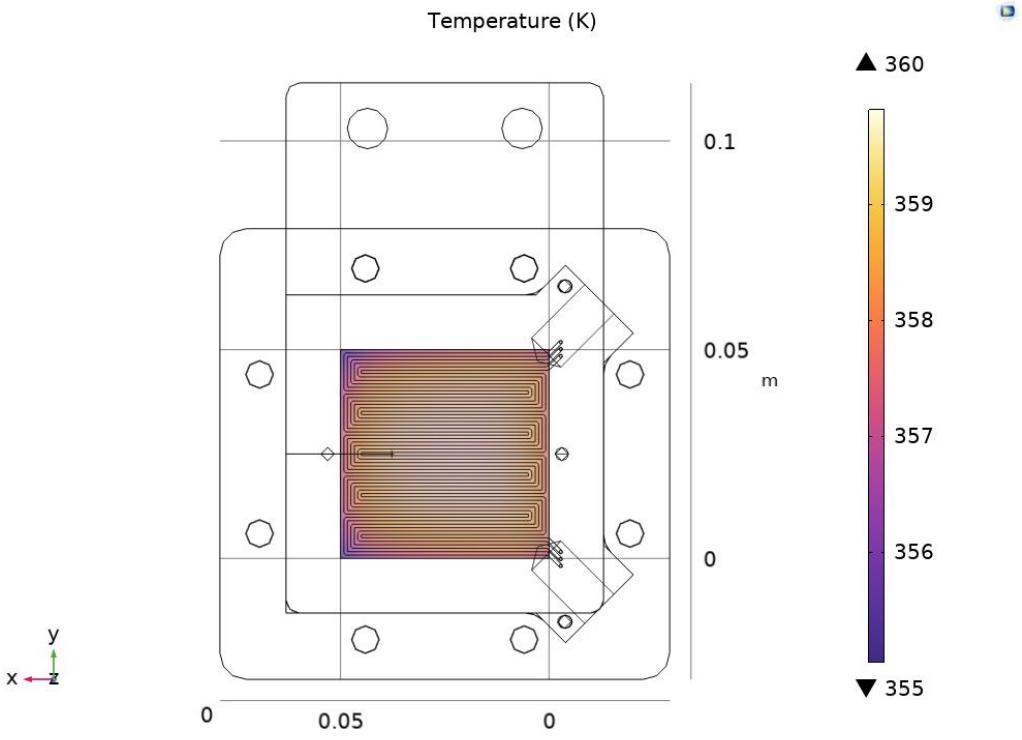

Figure 43. Temperature distribution across the membrane.

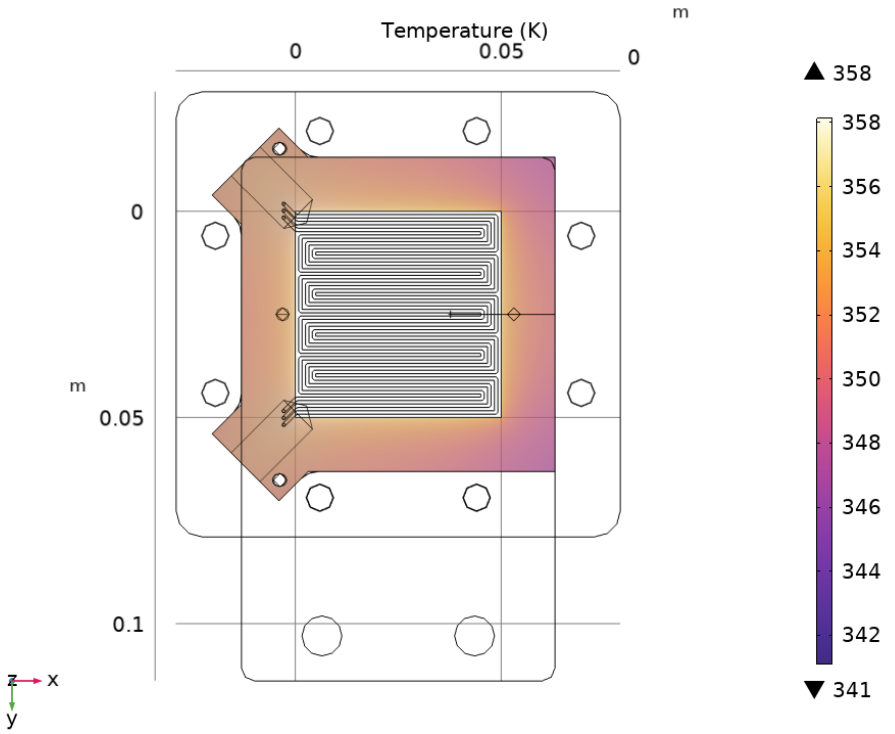

Figure 44. Temperature distribution across the gaskets.

5.3. Pressure distribution

The pressure distribution and deformation distribution is obtained by computing the thermal expansion Multiphysics as it considers both stress from the clamping pressure and from the thermal stress across all layers of the cell. Since the real temperature distribution could be obtained by computing the electrochemical heating Multiphysics, all physics and Multiphysics had been selected to provide the necessary temperature fields for thermal expansion computation.

The pressure and deformation distribution are assessed to make sure that all components of the cell don't fail under mechanical and thermal loads, and their mechanical limits are not violated. The deformation of components is also important since higher values could lead to failure of the cell and poor performance. Like the temperature distribution, the pressure distribution is mostly crucial for membrane and gaskets which can tolerate much less pressure compared to other metallic components.

On the other hand, low pressure values for the components could lead to leakage problems as some components might lose being perfectly sealed. The pressure indicator used to

assess the mechanical behaviour of components is Von Mises stress. If the Von Mises stress exceeds the material's yield strength, the material will permanently deform under the clamping bolt. The Von Mises stress distribution of the entire cell is shown in Figure 45.

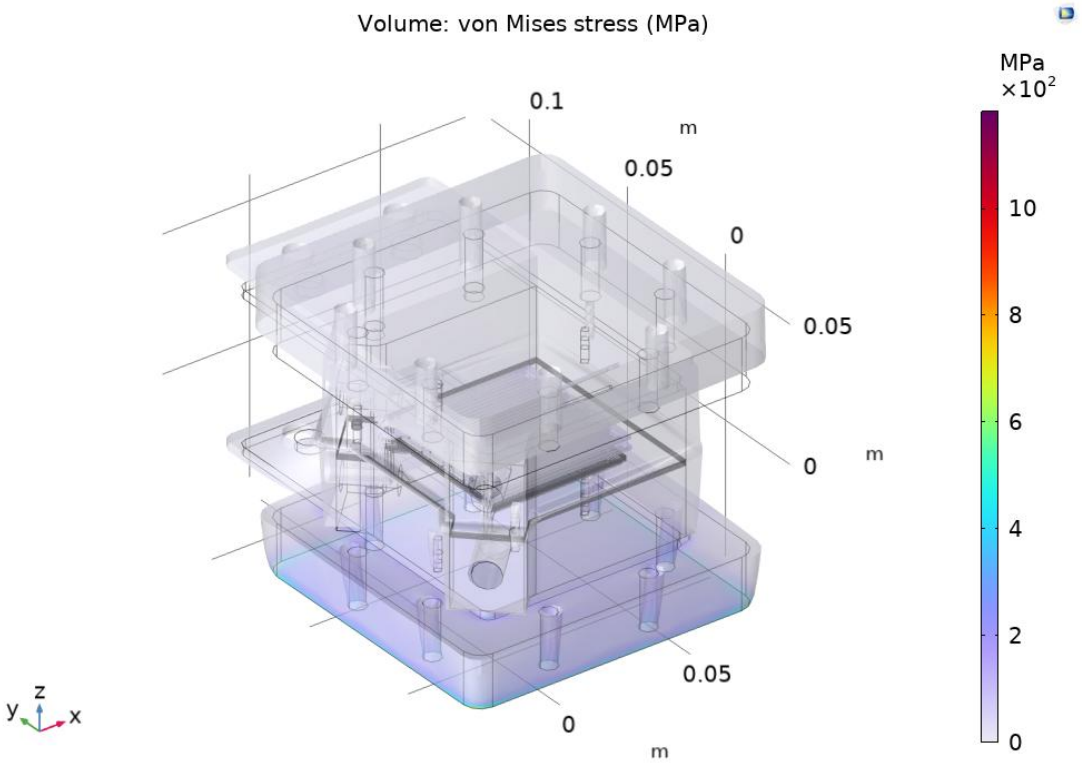

Figure 45. distribution of Von Mises stress across the cell.

It is cleat that the most critical parts of cell that are heavily under high values of stress are located at the edges of the cathode end plate at the bottom of the cell where it was assumed that its surface is fixed. to better visualize the Von Mises stress for other components which have much lower stress values, the same parameter is depicted for anode end plate and the membrane in Figure 46 and Figure 47 respectively.

The highest stress values on the anode end plate are located at the edges of its contact with current collector which is around 45 MPa which is still much lower than the yield strength of the anode end plate material that was selected as duplex stainless steel. The uniform stress distribution across the membrane leads to proper contact with electrodes which is very important for the performance of the cell.

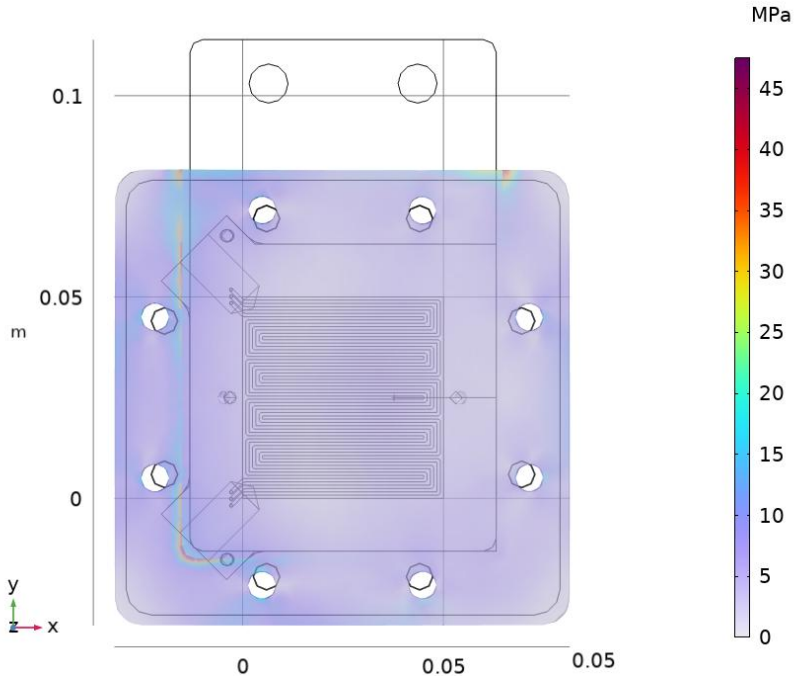

Figure 46. Von Mises stress of anode end plate.

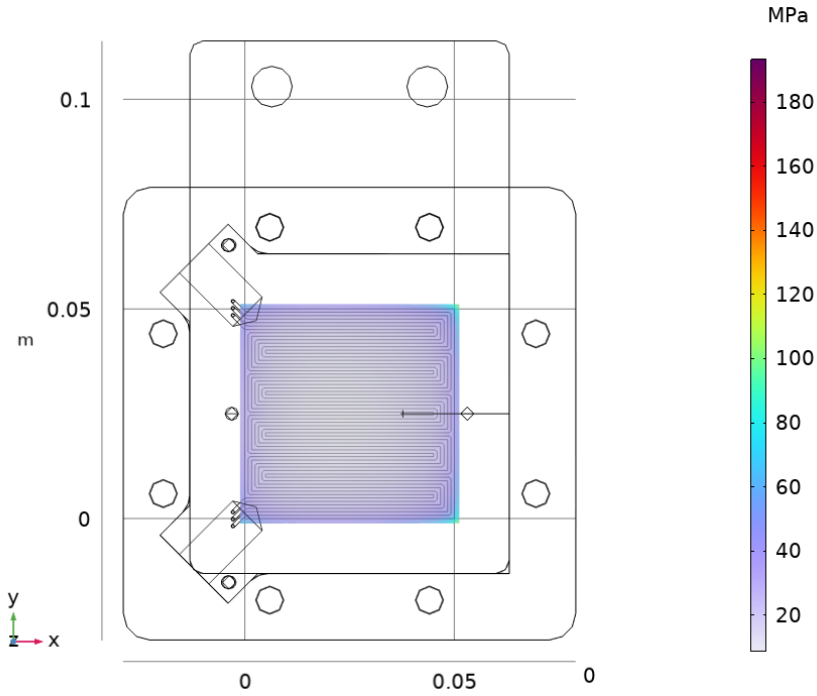

Figure 47. Von Mises stress of membrane.

Another important parameter that must be assessed in this section is the deformation (strain) of the components which could lead to mechanical failure if it reaches to high values. The strain of components is affected by clamping pressure applied by the bolts and the thermal expansion due to working at relatively high temperatures. The deformation of the entire cell is shown in Figure 48.

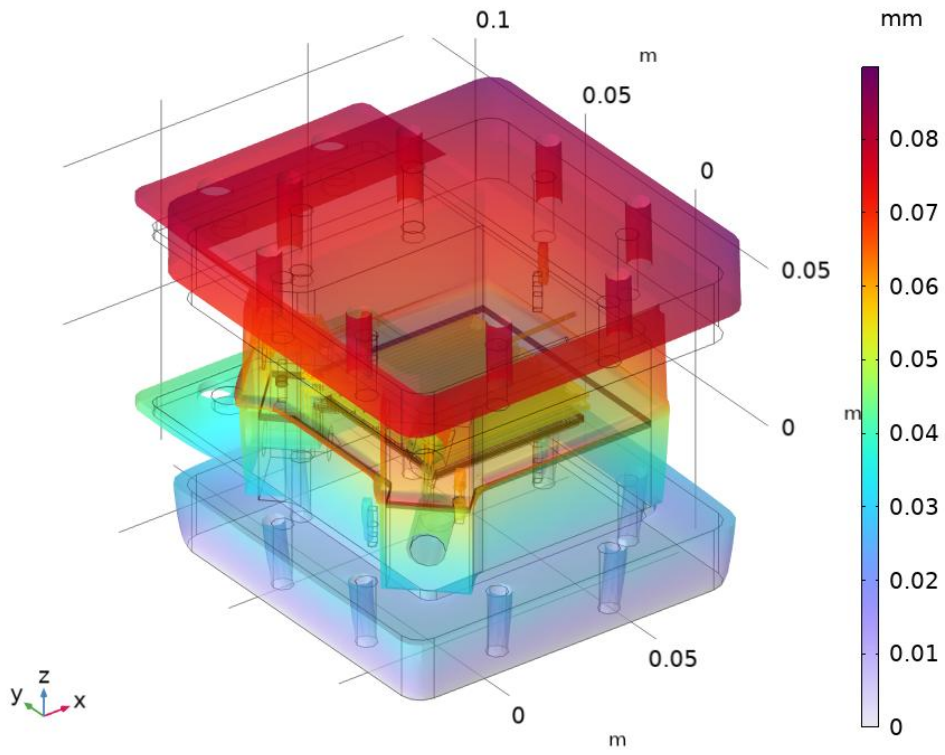

Figure 48. Total deformation of the cell components.

Among all components of the cell, gaskets are very sensitive to deformation since they're polymeric and are face more displacement compared to metallic parts and also, they are on the external parts of the cell where more pressure is applied on these areas and any failure of gaskets due to high deformation could decrease the safety and performance of the cell. The deformation of the gaskets is shown in Figure 49.

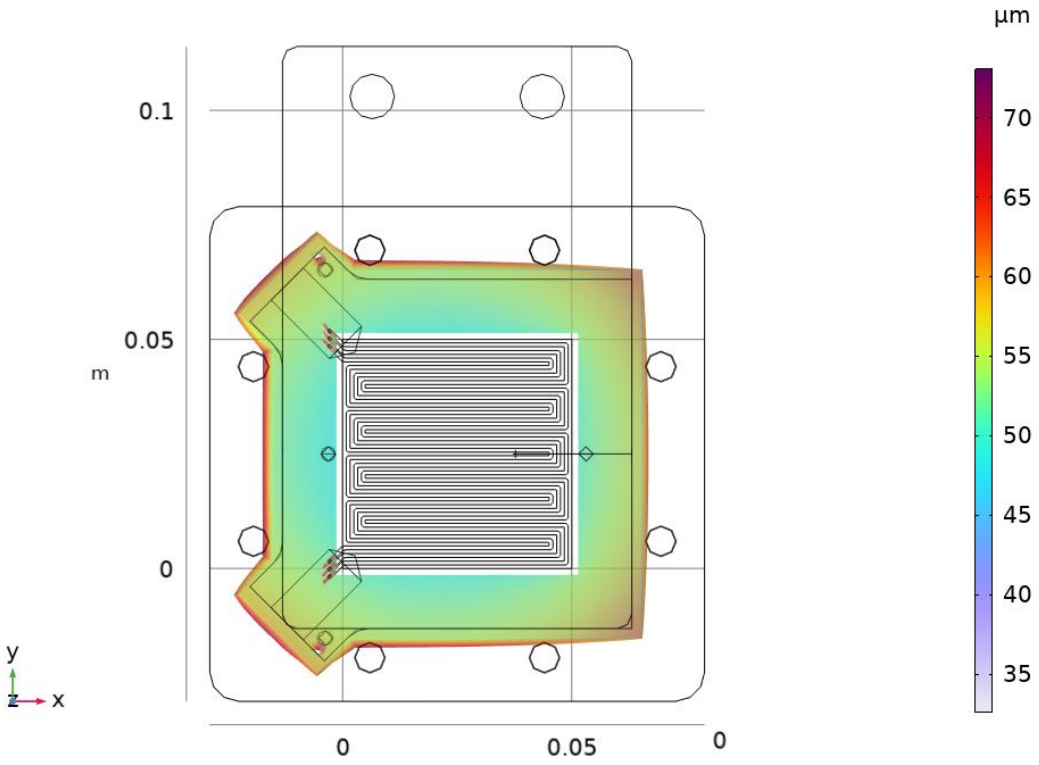

Figure 49. Deformation of gaskets.

The displacement of the edges of the gaskets is clear from the above figure, but the values are in the order of micrometres which is very low and wouldn't lead to any problem. It's also visible that the deformation at the edges of the gaskets are higher compared to internal parts due to higher effects of clamping loads across these areas.

5.4. Validation of results

After obtaining the results, it's necessary to validate them by comparing them with the results of similar models to see if the range of values for each parameter are acceptable or not. In the following, three different sections are provided to assess the validation of results which were already discussed. For validation of I-U curve, some models with similar operating conditions were selected, but for validation of temperature and pressure distribution, only one article having the most similar operating conditions were selected for each of them.

5.4.1. Validation of polarization curve

The main operating conditions of the studied model of this thesis project are as follows:

Operating Temperature: 70 °C

Operating Pressure: 30 bar at both sides

Electrolyte concentration: 1 M KOH water solution at the anode side and dry cathode feed

Membrane dimensions: 5 cm * 5 cm

To create the polarization curve of the model, the I-U curve required data derived from the COMSOL is provided in Table 28.

applied voltage [V]	total current [A]	current density [A/cm^2]
1.5	1.2343	0.049372
1.6	2.3846	0.095384
1.7	4.236	0.16944
1.8	7.0543	0.282172
1.9	11.054	0.44216
2	16.345	0.6538
2.1	22.963	0.91852
2.2	30.994	1.23976
using normal current density vector to calculate the total current		
electrode active area = 25 cm^2		

Table 28. I-U curve required data.

For better visualizing and comparing all similar models with the current model, a single plot was created containing the polarization curves of all models and a table containing the main operating conditions of the provided models.

The I_U curves for the purpose of validation are provided in Figure 50.

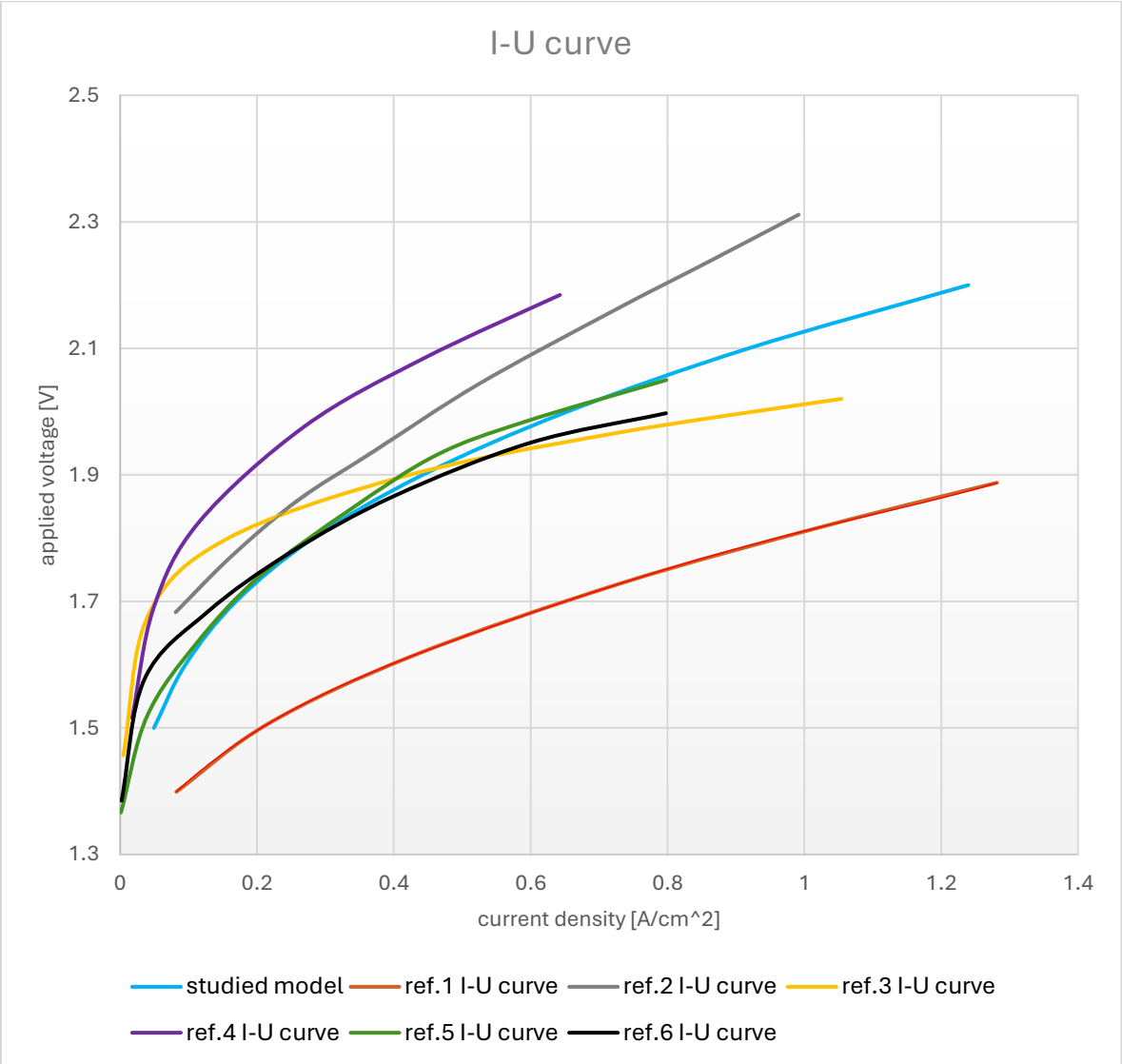

Figure 50. I-U curves for validation of the studied model.

The links for each reference article with their main operating conditions are provided in Table 29 that could be compared to the operating conditions of the current model studied.

reference number	operating temperature [°C]	operating pressure [bar]	KOH concentration	active surface area [cm^2]	membrane type	electrode catalysts	electrode material	cathode feed type	flow rate [ml/min]
studied model	70	30	1 M	25	PurionX-137	-	Nickel	dry	-
1	60	1	1	1.8	HTMA-DAPP	IrO2 for anode and PtRu/C for cathode	-	wet	100
2	60	1	1	10	Fumatech,FAA-3-50	Ni-Fe-Co hydroxide for anode and Ni-Mo alloy for cathode	Nickel mesh	wet	270
3	60	1	1	5	Sustanion	NiFe2O4 for anode and NiFeCo for cathode	Nickel for anode and Stainless steel for cathode	wet	-
4	60	1	1	1	Sustanion (X37-50 RT)	NiFe2O4 for anode and Raney Ni for cathode	Nickel fiber for anode and SS 316L fiber for cathode	wet	1.56
5	70	30 (differential pressure)	1	-	PiperION60	-	Raney-Nickel	dry	500
6	70	1	pure water	-	self-crosslinking quaternary ammonia polysulfone	-	Ni-Fe anode and Ni-Mo cathode	wet	-

Table 29. Operating conditions of models for validation. Ref.1 [97], Ref.2 [98], Ref.3 [6], Ref.4 [99], Ref.5 [100], Ref.6 [94]

It's also clear the I-U curves obtained from references number 5 and 6 have the closest behavior to our studied model.

5.4.2. Validation of Temperature distribution

The article used for validation of the temperature distribution applied some heat sources and sinks to consider the heat related to electrochemical reactions which in our case are all included in the "electrochemical heating" Multiphysics in COMSOL. In the reference article [101], The channels on the anode (oxygen) side were filled with water while the channels on the cathode side contained only the produced hydrogen gas. The entropic heat of the formation and evaporation of hydrogen was applied there, resulting in a heat sink on the cathode. On the anode side the produced oxygen is assumed to dissolve in the water at once, hence its entropic heat is assumed to be zero.

Heat sources/sinks were implemented in the catalyst layers where the electrochemical reactions take place and, in the membrane, where ohmic resistance produces considerable heat at the chosen current density. The entropic heat on the anode side is neglected. They assumed instant dissolution of the oxygen in the water there, so that no heat is consumed to vaporize the produced oxygen. On the cathode side the entropic heat is included. The configuration of the reference model is shown in Figure 51.

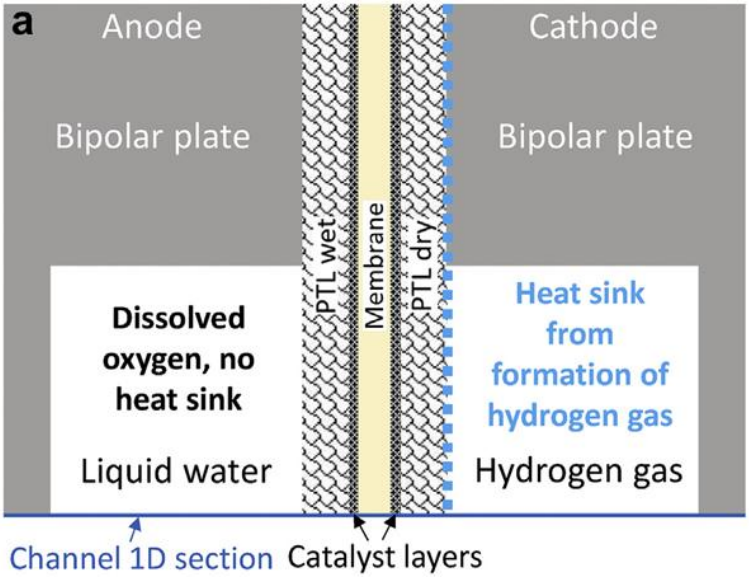

Figure 51. cell configuration of the reference model for validation. [101]

The reference model components materials are as follows: the Bipolar plate is made from stainless steel, the same as our studied model while the PTL material is Titanium which has lower thermal conductivity compared to Nickel GDL used in our model. The operating temperature was maintained at 80 °C which is 10°C higher than the model studied in this project. But in this section, mainly, the distribution of temperature and its gradient across different layers is what must be assessed and verified.

The temperature profile of the reference electrolyzer with an anion exchange membrane with different relative humidities, differentiated by their respective water uptake values of λ = 0 for RH = 0 and λ = 12 for RH =100 is shown in Figure 52.

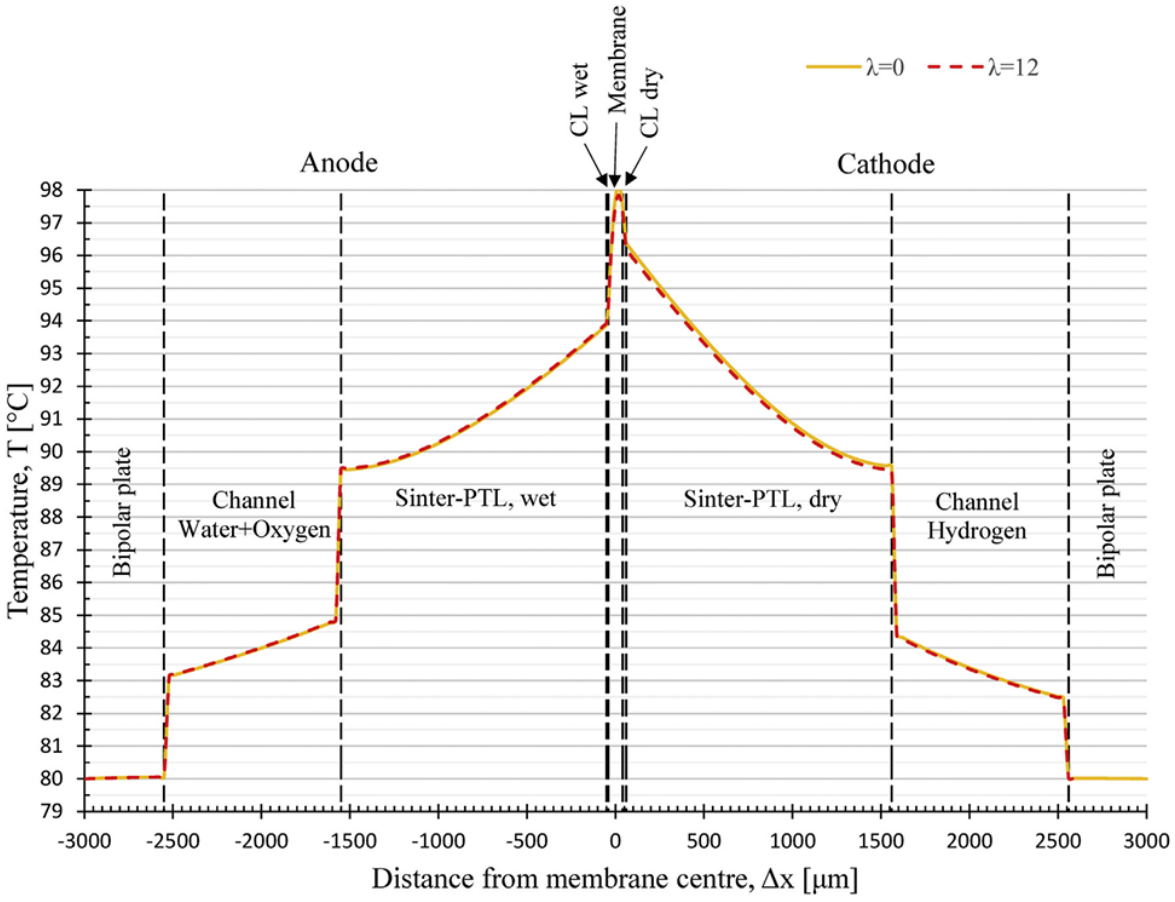

Figure 52. Temperature distribution of the reference AEMEL for validation. [101]

As the operating temperature is 10 °C higher than our model, the temperature distribution of our model shown in Figure 42 is very similar to the above plot only with a 10 °C shift. While the maximum temperature at membrane is 98 °C in the reference model, it's around 87 °C (360 K) in our model which indicates that the values of temperature obtained by the COMSOL simulation are valid.

For AEMEL at high current density, ignoring heat removal by convection across anode and cathode channels overpredicts temperature significantly. That's why the temperature distribution in GDL and bipolar plates in our model are higher compared to reference model since there's just an approximate modeling for the flow of anode and cathode channels which play a significant role in removing the heat from the center of the cell.

5.4.3. Validation of Pressure distribution

The reference model used for validation of mechanical aspects of the studied model was a PEM water electrolyser consists of a single cell with 9 cm^2 active area [102]. The structure of a PEMWE is similar to an AEMWE, so their pressure distribution and deformation could be compared with each other. The configuration of the reference model is shown in Figure 53.

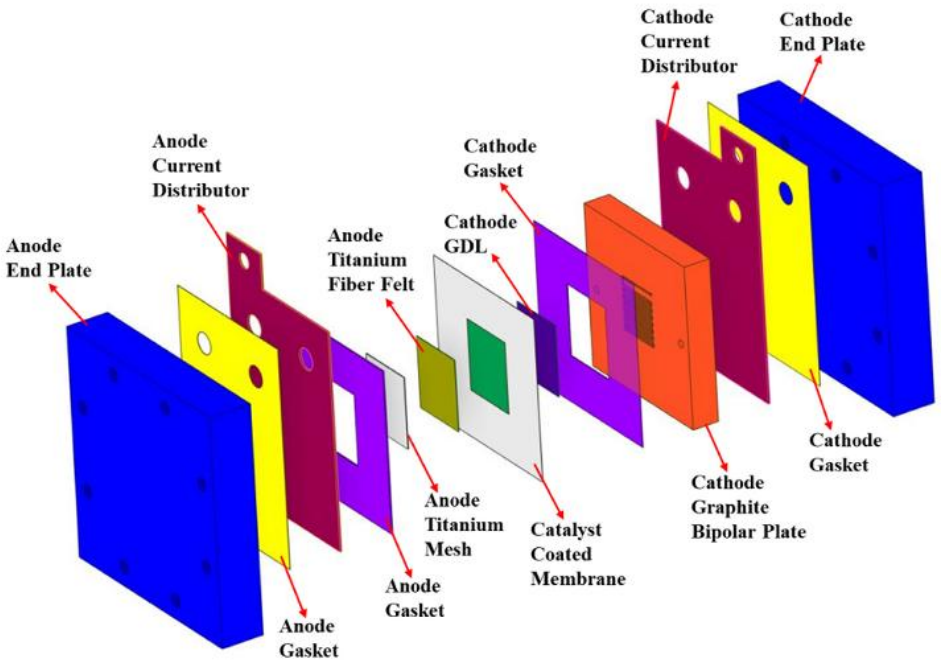

Figure 53. Cell configuration of the reference model for validation. [102]

The von mises stress (MPa) for the CCM and anode end plate (as the surface of the applying force) of the reference model is presented in the following with a bolt torque of 3 N.m which would be around 19000 N of clamping force considering the fact there are 8 bolts and assuming ¼" the size of the bolts since It's not mentioned in the reference model. The distribution of Von Mises stress across the membrane is shown in Figure 54 that could be compared with the thesis model in Figure 47.

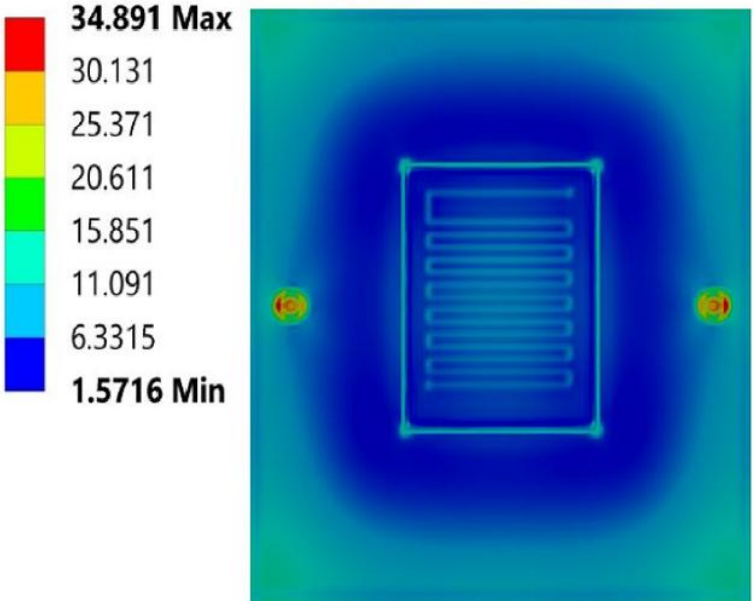

Figure 54. Von Mises stress of the membrane in reference model. [102]

For both CCM and end plate, the von mises stress is around 10 MPa for most parts of the surface which is very similar to the results of our model. The distribution of Von Mises stress across the anode end plate of the reference model is shown in Figure 55 that could be compared with the thesis model in Figure 46.

There is higher stress at the edges of the membrane and the contact edge of anode end plate and current collector in our model compared to the reference model due to the possible reasons of having differences in geometries and lower clamping force in the reference model compared to the thesis model. Besides, according to COMSOL website, a mesh that isn't fine enough (or properly placed) can produce misleadingly high-pressure peaks at edges and corners. These are usually numerical artifacts from poor resolution of contact geometry, singular corners, contact enforcement and extrapolation, not necessarily the "true" physical peak. [103]

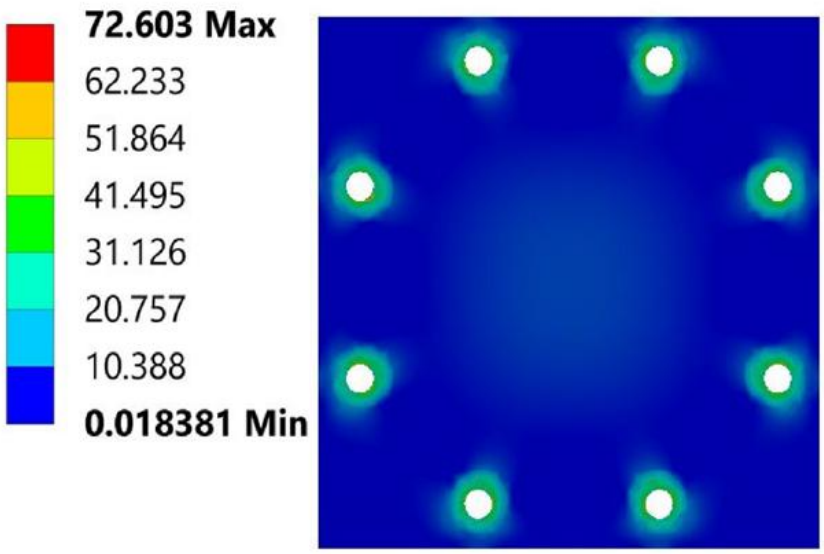

Figure 55. Von Mises stress across the anode end plate of the reference model. [102]

Finally, the deformation of cell (in mm) in the reference model is shown in Figure 56 which is mainly focused on the end plates and could be compared to the thesis model result in Figure 48. Since the clamping force is applied through bolts in the reference model, it's clear that the deformation is higher around the bolts while it's lower at the center. But in the thesis model, the clamping force was applied equally on the end plate surface, so the deformation is the same across the end plate surface.

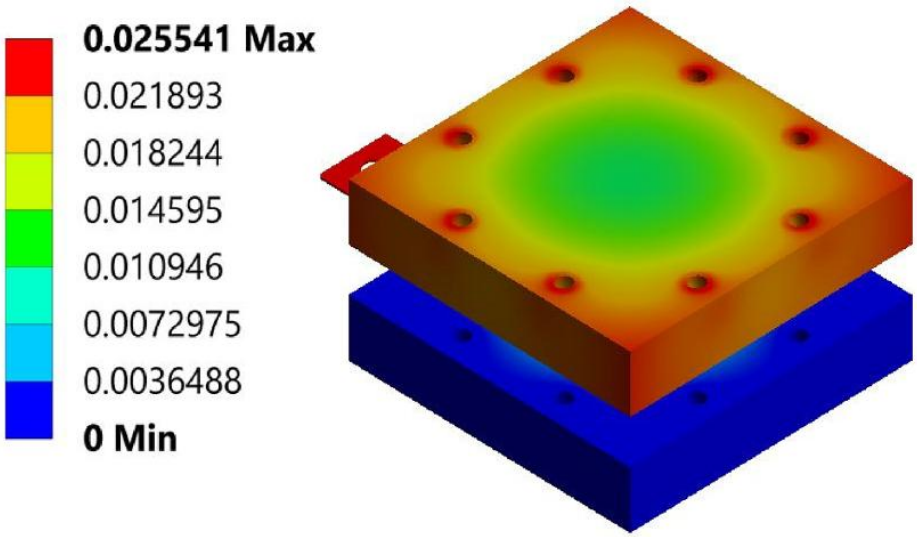

Figure 56. Deformation of the cell in reference model. [102]

6 Conclusion and Future Work

6.1. Conclusion

This thesis successfully developed a comprehensive 3D thermo-mechanical model of a single-cell AEM electrolyser. The necessity of moving towards more green technologies due to climate change and other important factors highlights the importance of development of systems such as electrolysers to produce cleaner hydrogen. Among different types of electrolysers, AEMWE has recently been under improvement due to its main advantage of not using the precious materials as catalysts like PEMWE. Firstly, different most used materials for all layers of a high pressure AEM electrolyser were provided with their main thermo-mechanical and electrical characteristics to have a broad overview of all possible options in terms of materials when trying to assemble a single cell. Based on the user priorities, whether it is economic or high performance, different configurations of layers' materials are assessed.

Through literature review and design studies, it was determined that maintaining a clamping pressure between 1.5 and 3.0 MPa is vital to prevent both leakage and mechanical failure of sensitive components like the membrane and gaskets. To realize the effect of different parameters affecting the clamping force, a sensitivity analysis has been done, and it was found that the bolts, membrane and the gaskets have the highest impact on the clamping force of the single cell electrolyser. Three different common cell designs were compared and it was found that although the tubular and circular designs could maintain very high operating pressures, but for this thesis case which the operating pressure is 30 bar at both anode and cathode side, the selection of a planar design satisfies all the requirements of a proper geometry as it has some main advantages like easier manufacturing rather than tubular design and better distribution of water compared to circular design. The importance of geometry aspects becomes more critical for gaskets and flow channels and so they were assessed in more detail. But, due to the complexity of the designing components, the high pressure AEM electrolyser model developed and manufactured by the NREL institution was used for creating the geometry of the thesis model as it was developed for 30 bar operating pressure with the same active area of the current study.

The physics studied in COMSOL were Heat Transfer in Solids, Structural Mechanics and Secondary Current Distribution. The simulation results revealed that:

- Electrochemical Performance: The polarization curve indicated a current density of approximately 0.65 A/cm^2 at an applied voltage of 2 V, which is consistent with experimental behaviors seen in literature.
- Thermal Management: The highest temperatures (peak ~360 K) were concentrated in the membrane, where reactions occur, while outer layers remained cooler due to convective heat transfer to the ambient environment.
- Mechanical Stability: Von Mises stress peaked at the edges of the cathode end plate, while stress distribution across the membrane remained uniform, ensuring proper contact with the electrodes.

Validation against PEMWE and AEMWE reference models confirmed that the resulting temperature and pressure profiles are within acceptable physical ranges.

6.2. Future Work

To enhance the accuracy and applicability of the current model, several improvements are proposed for future research:

- Physics Settings: The model currently uses an approximate modeling approach for cooling. Future iterations should incorporate full fluid dynamics (CFD**)** within the flow channels to more accurately represent heat removal by the circulating electrolyte and product gases.
- Geometry Optimization: To reach higher differential pressures (up to 100 bar), research should explore circular cell outlines or reinforced frames to minimize the localized stress concentrations typically found at the corners of planar designs.
- Material Selection: Further investigation into structured or glass-filled PTFE and reinforced thermoplastics like PPSU could improve sealing reliability and long-term resistance to creep at elevated temperatures.
- Mesh Refinement: To eliminate potential numerical artifacts such as misleading stress peaks at component edges, more refined local mesh settings and advanced contact enforcement techniques should be employed.

References

[1] N. Du, C. Roy, R. Peach, M. Turnbull, S. Thiele, and C. Bock, “Anion-Exchange Membrane Water Electrolyzers,” Jul. 13, 2022, *American Chemical Society*. doi: 10.1021/acs.chemrev.1c00854.

[2] S. Shiva Kumar and H. Lim, “An overview of water electrolysis technologies for green hydrogen production,” Nov. 01, 2022, *Elsevier Ltd*. doi: 10.1016/j.egyr.2022.10.127.

[3] P. Sun *et al.*, “Criteria Air Pollutants and Greenhouse Gas Emissions from Hydrogen Production in U.S. Steam Methane Reforming Facilities,” *Environ. Sci. Technol.*, vol. 53, no. 12, pp. 7103–7113, Jun. 2019, doi: 10.1021/acs.est.8b06197.

[4] R. Bernat, J. Milewski, O. Dybinski, A. Martsinchyk, and P. Shuhayeu, “Review of AEM Electrolysis Research from the Perspective of Developing a Reliable Model,” Oct. 01, 2024, *Multidisciplinary Digital Publishing Institute (MDPI)*. doi: 10.3390/en17205030.

[5] L. Xia, S. Holtwerth, C. Rodenbücher, W. Lehnert, M. Shviro, and M. Müller, “Effects of mechanical pressure on anion exchange membrane water electrolysis: A non-negligible yet neglected factor,” *J. Power Sources*, vol. 590, Jan. 2024, doi: 10.1016/j.jpowsour.2023.233802.

[6] I. V. Pushkareva, A. S. Pushkarev, S. A. Grigoriev, P. Modisha, and D. G. Bessarabov, “Comparative study of anion exchange membranes for low-cost water electrolysis,” *Int. J. Hydrogen Energy*, vol. 45, no. 49, pp. 26070–26079, Oct. 2020, doi: 10.1016/j.ijhydene.2019.11.011.

[7] S. A. Lee, J. Kim, K. C. Kwon, S. H. Park, and H. W. Jang, “Anion exchange membrane water electrolysis for sustainable large-scale hydrogen production,” Jun. 01, 2022, *John Wiley and Sons Inc*. doi: 10.1002/cnl2.9.

[8] E. López-Fernández, C. G. Sacedón, J. Gil-Rostra, F. Yubero, A. R. González-Elipe, and A. de Lucas-Consuegra, “Recent advances in alkaline exchange membrane water electrolysis and electrode manufacturing,” Nov. 01, 2021, *MDPI*. doi: 10.3390/molecules26216326.

[9] S. Garg, C. A. Giron Rodriguez, T. E. Rufford, J. R. Varcoe, and B. Seger, “How membrane characteristics influence the performance of CO2 and CO electrolysis,” Nov. 01, 2022, *Royal Society of Chemistry*. doi: 10.1039/d2ee01818g.

[10] Y. Wang *et al.*, “Potential technology for seawater electrolysis: Anion-exchange membrane water electrolysis,” Jul. 20, 2023, *Cell Press*. doi: 10.1016/j.checat.2023.100643.

[11] “https://www.fuelcellstore.com/anion-exchange-membrane/purionx-131”.

[12] “https://webthesis.biblio.polito.it/28404/1/tesi.pdf#:~:text=Finally%2C%20AEM%20electrolysers%20combine%20using%20a%20polymeric,holy%20grail%20of%20electrolyser%20technologies%20(Electrolyzers%2C%202023)”.

[13] “https://juser.fz-juelich.de/record/903454/files/Electrochemical-%20and%20mechanical%20stability%20of%20catalyst%20layers%20in%20anion%20exchange%20membrane%20water%20electrolysis.pdf#:~:text=match%20at%20L604%20mechanical%20thin,Aemion%20for%2030%20min%20at”.

[14] E. K. Volk, M. E. Kreider, S. Kwon, and S. M. Alia, “Recent progress in understanding the catalyst layer in anion exchange membrane electrolyzers – durability, utilization, and integration,” Jan. 01, 2024, *Royal Society of Chemistry*. doi: 10.1039/d3ey00193h.

[15] E. López-Fernández, C. G. Sacedón, J. Gil-Rostra, F. Yubero, A. R. González-Elipe, and A. de Lucas-Consuegra, “Recent advances in alkaline exchange membrane water electrolysis and electrode manufacturing,” Nov. 01, 2021, *MDPI*. doi: 10.3390/molecules26216326.

[16] R. Narducci, J. F. Chailan, A. Fahs, L. Pasquini, M. L. Di Vona, and P. Knauth, “Mechanical properties of anion exchange membranes by combination of tensile stress-strain tests and dynamic mechanical analysis,” *J. Polym. Sci. B Polym. Phys.*, vol. 54, no. 12, pp. 1180–1187, Jun. 2016, doi: 10.1002/polb.24025.

[17] X. Zhang *et al.*, “Enhancement of the mechanical properties of anion exchange membranes with bulky imidazolium by ‘thiol-ene’ crosslinking,” *J. Memb. Sci.*, vol. 596, Feb. 2020, doi: 10.1016/j.memsci.2019.117700.

[18] C. E. Ayala, R. L. Pérez, J. K. Mathaga, A. Watson, T. Evans, and I. M. Warner, “Fluorescent Ionic Probe for Determination of Mechanical Properties of Healed Poly(ethylene- co-methacrylic acid) Ionomer Films,” *ACS Appl. Polym. Mater.*, vol. 4, no. 2, pp. 832–841, Feb. 2022, doi: 10.1021/acsapm.1c01325.

[19] J. Lei *et al.*, “Understanding and resolving the heterogeneous degradation of anion exchange membrane water electrolysis for large-scale hydrogen production,” Dec. 01, 2024, *Springer*. doi: 10.1007/s43979-024-00101-y.

[20] "https://www.matweb.com/search/DataSheet.aspx?MatGUID=e6eb83327e534850a062dbca3bc758dc&ckck=1".

[21] "https://www.makeitfrom.com/material-properties/ACI-ASTM-CF3M-SCS16A-J92800-Cast-Stainless-Steel".

[22] "https://www.attelements.com/nickel-metal-and-alloys/nickel-foamniti-foam.html".

[23] K. Haraldsen and Leth-Olsen, "STRESS CORROSION CRACKING OF STAINLESS STEELS IN HIGH PRESSURE ALKALINE ELECTROLYSERS."

[24] "https://www.fuelcellstore.com/toray-carbon-paper-090#:".

[25] "https://cheersonic-liquid.com/en/aem-porous-transport-layer-and-bipolar-plate/".

[26] S. J. You, X. H. Wang, J. N. Zhang, J. Y. Wang, N. Q. Ren, and X. B. Gong, "Fabrication of stainless steel mesh gas diffusion electrode for power generation in microbial fuel cell," *Biosens. Bioelectron.*, vol. 26, no. 5, pp. 2142–2146, Jan. 2011, doi: 10.1016/j.bios.2010.09.023.

[27] "https://tmnetch.com/etched-products/fuel-cell-bipolar-plate-2/titanium-bipolar-plates/".

[28] J. André, L. Antoni, J. P. Petit, E. De Vito, and A. Montani, "Electrical contact resistance between stainless steel bipolar plate and carbon felt in PEFC: A comprehensive study," *Int. J. Hydrogen Energy*, vol. 34, no. 7, pp. 3125–3133, Apr. 2009, doi: 10.1016/j.ijhydene.2009.01.089.

[29] "https://www.makeitfrom.com/material-properties/Grade-2-3.7035-R50400-Titanium".

[30] "https://www.makeitfrom.com/material-properties/UNS-N08028-Alloy-28-Stainless-Steel".

[31] "https://www.makeitfrom.com/material-properties/UNS-S32205-Stainless-Steel".

[32] "https://specialtygaskets.com/blogs/news/solving-sealing-challenges-with-ptfe-gaskets-expert-insights#:~:text=C.,Carbon%2DFilled%20PTFE%20Gaskets".

[33] "https://www.plasticpipeshop.co.uk/assets/images/technical/EPDM%20chemical%20compatibility.pdf#:~:text=Lye%3A%20Ca,Hydroxide%20Good%20up%20to%2022oC".

[34] “https://designerdata.nl/materials/plastics/rubbers/ethylene-propylene-diene-m-class-rubber”.

[35] “https://www.makeitfrom.com/material-properties/Ethylene-Propylene-Diene-Rubber-EPDM-EPT”.

[36] “https://designerdata.nl/materials/plastics/thermo-plastics/polytetrafluoroethylene-(teflon)”.

[37] “https://www.makeitfrom.com/material-properties/Perfluoroelastomer-FFKM”.

[38] “https://www.lookpolymers.com/polymer_DuPont-Performance-Polymers-Kalrez-1050LF-FFKM-Perfluoroelastomer.php”.

[39] “https://www.fuelcellstore.com/epdm-rubber-50A”.

[40] Q. Xu *et al.*, “Anion Exchange Membrane Water Electrolyzer: Electrode Design, Lab-Scaled Testing System and Performance Evaluation,” Sep. 01, 2022, *Elsevier B.V.* doi: 10.1016/j.enchem.2022.100087.

[41] “https://www.matweb.com/search/DataSheet.aspx?MatGUID=9aebe83845c04c1db5126fada6f76f7e&ckck=1”.

[42] “https://www.matweb.com/search/DataSheet.aspx?MatGUID=e6eb83327e534850a062dbca3bc758dc”.

[43] “https://www.matweb.com/search/DataSheet.aspx?MatGUID=3f64b985402445c0a5af911135909344”.

[44] “https://redox-flow.com/product/current-collectors-x-cell/”.

[45] “https://www.scribner.com/knowledgebase/high-pressure-electrolyzer-cell-fixture/”.

[46] C. A. Mills *et al.*, “Improvement in the Electrical Properties of Nickel-Plated Steel Using Graphitic Carbon Coatings,” *Adv. Eng. Mater.*, vol. 21, no. 10, Oct. 2019, doi: 10.1002/adem.201900408.

[47] “https://www.vestedmetals.net/”.

[48] “https://www.bartleby.com/questions-and-answers/table-17.1-resistivities-and-temperature-coefficients-of-resistivity-for-various-materials-at-20c-te/003151c9-edf1-451f-a3e3-9bdb63accaea”.

[49] “https://www.alibaba.com/showroom/nimo-catalyst.html?utm_source”.

[50] “https://www.fuelcellstore.com/iridium-oxide-high-surface-area-and-high-performance-3161610?utm_source”.

[51] “https://www.alibaba.com/showroom/nimo-catalyst.html?utm_source”.

[52] “https://www.goldavenue.com/en/platinum-price/usd”.

[53] “https://www.fuelcellstore.com/versogen-piperion-aem-self-supporting-20um-73800000?utm_source”.

[54] “https://www.fuelcellstore.com/sustainion-x37-50-grade-rt-membrane”.

[55] “https://www.fuelcellstore.com/fuel-cell-cars/fuel-cell-components/stainless-steel-wire-cloth-316”.

[56] “https://www.fuelcellstore.com/gas-diffusion-layers/wire-mesh-and-cloth/nickel-foam-1mm-2691011”.

[57] “https://mepsinternational.com/gb/en/products/europe-stainless-hot-rolled-plate-316-price-forecast?utm_source”.

[58] “https://www.alibaba.com/product-detail/Incoloy-20-Alloy-20-UNS-N08020_1600506442380.html?spm=a2700.galleryofferlist.topad_classic.d_title.a71c13a0qWWVWl”.

[59] “https://www.ingotmetals.co.nz/”.

[60] “https://www.sigmaaldrich.com/IT/it/product/aldrich/gf27935994?srsltid=AfmBOor2Mzc9jA_z_pr9wNKsIn39-UjluJcI_ZIn8XO_hqWyHxS-GfiJ&utm_source=”.

[61] “https://pmarketresearch.com/worldwide-perfluorinated-elastomers-ffkm-market-research-2024-by-type-application-participants-and-countries-forecast-to-2030/”.

[62] “https://www.stainlesssteelpriceperkg.com/stainless-steel-duplex-2205-price-list/”.

[63] “https://enapter.com/en/aem-by-enapter-electrolysis/”.

[64] D. Henkensmeier, M. Najibah, C. Harms, J. Žitka, J. Hnát, and K. Bouzek, “Overview: State-of-the Art Commercial Membranes for Anion Exchange Membrane Water

Electrolysis," *Journal of Electrochemical Energy Conversion and Storage*, vol. 18, no. 2, May 2021, doi: 10.1115/1.4047963.

[65] "https://www.hydrogen.energy.gov/docs/hydrogenprogramlibraries/pdfs/review23/p204_james_2023_o-pdf.pdf".

[66] "https://enapter.com/en/blog/aem-water-electrolysis-how-it-works/".

[67] "https://www.scribner.com/knowledgebase/high-pressure-electrolyzer-cell-fixture/".

[68] P. Lin, P. Zhou, and C. W. Wu, "A high efficient assembly technique for large PEMFC stacks. Part I. Theory," *J. Power Sources*, vol. 194, no. 1, pp. 381–390, Oct. 2009, doi: 10.1016/j.jpowsour.2009.04.068.

[69] Ö. F. Selamet, M. C. Acar, M. D. Mat, and Y. Kaplan, "Effects of operating parameters on the performance of a high-pressure proton exchange membrane electrolyzer," *Int. J. Energy Res.*, vol. 37, no. 5, pp. 457–467, Apr. 2013, doi: 10.1002/er.2942.

[70] A. Laube *et al.*, "Tubular membrane electrode assembly for PEM electrolysis," *Int. J. Hydrogen Energy*, vol. 47, no. 36, pp. 15943–15951, Apr. 2022, doi: 10.1016/j.ijhydene.2022.03.135.

[71] "https://tfaws.nasa.gov/wp-content/uploads/TFAWS23-ID-7-Presentation.pdf".

[72] "https://patentimages.storage.googleapis.com/80/f3/01/330be4ea3ee85f/WO2023237535A1.pdf".

[73] "https://enapter.com/en/enapter-products-aem/".

[74] "https://www.fst.com/hydrogen/".

[75] "https://hyfindr.com/en/hydrogen-knowledge/aem-electrolysers-how-they-work-key-components".

[76] T. Berning, "Design of a Proton Exchange Membrane Electrolyzer," *Hydrogen (Switzerland)*, vol. 6, no. 2, Jun. 2025, doi: 10.3390/hydrogen6020030.

[77] "https://www.omniseal-solutions.com/blogs/energy-insights-advanced-gaskets-electrolyzer-efficiency".

[78] M. A. S. Zaghloul *et al.*, “High spatial resolution temperature profile measurements of solid-oxide fuel cells,” *Appl. Energy*, vol. 288, Apr. 2021, doi: 10.1016/j.apenergy.2021.116633.

[79] “https://www.ensingerplastics.com/en-us/hydrogen/electrolyzer-components”.

[80] Y. Wei, Y. Xing, X. Zhang, Y. Wang, J. Cao, and F. Yang, “A Review of Sealing Systems for Proton Exchange Membrane Fuel Cells,” Aug. 01, 2024, *Multidisciplinary Digital Publishing Institute (MDPI)*. doi: 10.3390/wevj15080358.

[81] E. Zhang, W. Wang, Y. Zhao, M. Zhu, and J. Zhang, “The structure optimization and performance analysis of bipolar plate flow field for proton exchange membrane water electrolysis,” *J. Power Sources*, vol. 661, Jan. 2026, doi: 10.1016/j.jpowsour.2025.238681.

[82] W. H. Chen *et al.*, “Optimization of Flow Channel Design with Porous Medium Layers in a Proton Exchange Membrane Electrolyzer Cell,” *Energies (Basel).*, vol. 16, no. 15, Aug. 2023, doi: 10.3390/en16155642.

[83] W. Zhao *et al.*, “Impact of Multiple Inlet and Outlet Structures of Bipolar Plate Channel on the Mass Transport in ALK Electrolyzers,” *Energies (Basel).*, vol. 18, no. 11, Jun. 2025, doi: 10.3390/en18112771.

[84] A. Loh, X. Li, S. Sluijter, P. Shirvanian, Q. Lai, and Y. Liang, “Design and Scale-Up of Zero-Gap AEM Water Electrolysers for Hydrogen Production,” *Hydrogen (Switzerland)*, vol. 4, no. 2, pp. 257–271, Jun. 2023, doi: 10.3390/hydrogen4020018.

[85] X. Y. Wong, Y. Zhuo, and Y. Shen, “CFD modelling and optimisation of electrolyser flow channel designs for highly efficient hydrogen production.” [Online]. Available: https://ssrn.com/abstract=4063741

[86] “https://redox.me/products/nrel-high-pressure-lte-cell-nrel-high-pressure-low-temperature-electrolysis-cell”.

[87] G. H. A. Wijaya, K. S. Im, and S. Y. Nam, “Advancements in commercial anion exchange membranes: A review of membrane properties in water electrolysis applications,” Oct. 01, 2024, *Elsevier B.V.* doi: 10.1016/j.dwt.2024.100605.

[88] “https://www.fuelcellstore.com/spec-sheets/purionx_131_technical_data_sheet_2024.pdf”.

[89] H. Zhou, K. Meng, W. Chen, and B. Chen, “3D two-phase and non-isothermal modeling for PEM water electrolyzer: Heat and mass transfer characteristic investigation,” *Int. J. Energy Res.*, 2022, doi: 10.1002/er.8375.

[90] M. K. Datta and P. N. Kumta, “Silicon, graphite and resin based hard carbon nanocomposite anodes for lithium ion batteries,” *J. Power Sources*, vol. 165, no. 1, pp. 368–378, Feb. 2007, doi: 10.1016/j.jpowsour.2006.12.013.

[91] X. Zhu, W. Li, H. Zhao, and X. Jin, “Effects of cryogenic and tempered treatment on the hydrogen embrittlement susceptibility of TRIP-780 steels,” *Int. J. Hydrogen Energy*, vol. 38, no. 25, pp. 10694–10703, Aug. 2013, doi: 10.1016/j.ijhydene.2013.05.113.

[92] B. Xu *et al.*, “A comprehensive study of parameters distribution in a short PEM water electrolyzer stack utilizing a full-scale multi-physics model,” *Energy*, vol. 300, Aug. 2024, doi: 10.1016/j.energy.2024.131565.

[93] A. Al-Masri, M. Peksen, and K. Khanafer, “3D multiphysics modeling aided APU development for vehicle applications: A thermo-structural investigation,” *Int. J. Hydrogen Energy*, vol. 44, no. 23, pp. 12094–12107, May 2019, doi: 10.1016/j.ijhydene.2019.03.079.

[94] L. An, T. S. Zhao, Z. H. Chai, P. Tan, and L. Zeng, “Mathematical modeling of an anion-exchange membrane water electrolyzer for hydrogen production,” *Int. J. Hydrogen Energy*, vol. 39, no. 35, pp. 19869–19876, Dec. 2014, doi: 10.1016/j.ijhydene.2014.10.025.

[95] E. Tardy, Y. Bultel, F. Druart, A. Bonnefont, M. Guillou, and B. Latour, “Three-Dimensional Modeling of Anion Exchange Membrane Electrolysis: A Two-Phase Flow Approach,” *Energies* , vol. 17, no. 13, Jul. 2024, doi: 10.3390/en17133238.

[96] “https://doc.comsol.com/5.6/doc/com.comsol.help.echem/echem_ug_electrochem.06.080.html”.

[97] E. Tardy, Y. Bultel, F. Druart, A. Bonnefont, M. Guillou, and B. Latour, “Three-Dimensional Modeling of Anion Exchange Membrane Electrolysis: A Two-Phase Flow Approach,” *Energies* , vol. 17, no. 13, Jul. 2024, doi: 10.3390/en17133238.

[98] A. Loh, X. Li, S. Sluijter, P. Shirvanian, Q. Lai, and Y. Liang, “Design and Scale-Up of Zero-Gap AEM Water Electrolysers for Hydrogen Production,” *Hydrogen (Switzerland)*, vol. 4, no. 2, pp. 257–271, Jun. 2023, doi: 10.3390/hydrogen4020018.

[99] K. Lawand, S. Nuggehalli Sampathkumar, Z. Mury, and J. Van Herle, “Membrane electrode assembly simulation of anion exchange membrane water electrolysis,” *J. Power Sources*, vol. 595, Mar. 2024, doi: 10.1016/j.jpowsour.2023.234047.

[100] E. Delp, R. Mishra, and E. Wagner, “Evaluation of complex multi-physics phenomena at gas diffusion electrodes during high-pressure water electrolysis with AEMs,” *Sci. Rep.*, vol. 15, no. 1, Dec. 2025, doi: 10.1038/s41598-025-05216-5.

[101] R. Bock *et al.*, “Measuring the thermal conductivity of membrane and porous transport layer in proton and anion exchange membrane water electrolyzers for temperature distribution modeling,” *Int. J. Hydrogen Energy*, vol. 45, no. 2, pp. 1236–1254, Jan. 2020, doi: 10.1016/j.ijhydene.2019.01.013.

[102] S. N. Ozdemir, I. Taymaz, F. G. B. San, and E. Okumuş, “Performance assessment and optimization of the PEM water electrolyzer by coupled response surface methodology and finite element modeling,” *Fuel*, vol. 365, Jun. 2024, doi: 10.1016/j.fuel.2024.131138.

[103] “https://doc.comsol.com/5.6/doc/com.comsol.help.sme/sme_ug_theory.06.68.html”.